

2017

FIELD OBSERVATIONS OF INFRAGRAVITY WAVE RESPONSE TO VARIABLE SEA-SWELL WAVE FORCING

Inch, Kris William

<http://hdl.handle.net/10026.1/10164>

<http://dx.doi.org/10.24382/525>

University of Plymouth

All content in PEARL is protected by copyright law. Author manuscripts are made available in accordance with publisher policies. Please cite only the published version using the details provided on the item record or document. In the absence of an open licence (e.g. Creative Commons), permissions for further reuse of content should be sought from the publisher or author.

**FIELD OBSERVATIONS OF INFRAGRAVITY WAVE RESPONSE
TO VARIABLE SEA-SWELL WAVE FORCING**

by

KRIS WILLIAM INCH

A thesis submitted to Plymouth University in partial fulfilment for the degree of

DOCTOR OF PHILOSOPHY

School of Biological and Marine Sciences

Faculty of Science and Engineering

June 2017

This copy of the thesis has been supplied on condition that anyone who consults it is understood to recognise that its copyright rests with its author and that no quotation from the thesis and no information derived from it may be published without the author's prior consent.

Abstract

Name: Kris William Inch

Title: Field observations of infragravity wave response to variable sea-swell wave forcing

Infragravity waves are low frequency (0.005-0.04 Hz) waves that can dominate the spectrum of water motions and sediment transport processes within the inner surf zone. Despite the established importance of infragravity waves in shaping our coasts and numerous studies dating back to the 1950s, several aspects of infragravity wave analysis, generation and dissipation remain poorly understood. As much of the recent infragravity research has focussed on fetch-limited coasts, less is known about the climatology of these waves on energetic coastlines subject to both swell and fetch-limited waves. It has been postulated that bed friction only plays a significant role in the dissipation of infragravity waves where the bed is exceptionally rough, but the precise impact of bed roughness is not fully understood, particularly on extremely rough rock platforms. Finally, although there have been many methodologies proposed for the decomposition of reflective wave fields (an essential tool for studying infragravity wave dynamics), very little attention has been given to evaluating their accuracy, particularly the impact of uncorrelated noise.

This study aims, primarily through the collection of an extensive field dataset and the establishment of accurate analysis tools, to provide new insight into the propagation, dissipation and reflection of infragravity waves on energetic coastlines of varied roughness, subject to both swell and fetch-limited waves.

To ensure the accurate decomposition of infragravity wave signals into their incident and reflected components, a sensitivity analysis into the effect of uncorrelated noise on an array separation method is performed. Results show that signal noise, often prevalent in field data, introduces a significant bias to estimates of incident and reflected wave spectra, and corresponding reflection coefficients. This bias can exceed 100% for signal-to-noise ratios of <1 . Utilising the systematic change in coherence with noise, a correction function is developed which is effective at reducing bias by up to 90%. When applied to field data, results imply that infragravity reflection coefficients can be overestimated by $>50\%$ if signal noise is unaccounted for. Consequently, noise reduction should form an integral part of future infragravity wave studies.

New research from a dissipative, fetch-unlimited sandy beach (Perranporth, Cornwall, UK) and a macrotidal, rocky shore platform (Freshwater West, Pembrokeshire, UK) uniquely demonstrates that the level of infragravity wave energy close to shore is linearly dependent on the offshore short wave energy flux $H_o^2 T_p$ ($r^2 = 0.93$ and 0.79 , respectively). Infragravity waves approach the coast as bound waves lagging slightly (~ 4 s) behind the wave group envelope and are released in the surf zone where their heights can exceed 1

m. Considerable infragravity dissipation is observed in the surf zone and is a function of both frequency and $H_o^2 T_p$. Complex Empirical Orthogonal Function (EOF) analysis reveals (quasi-)standing waves at low infragravity frequencies <0.017 Hz. Conversely, at higher frequencies (>0.017 Hz), infragravity waves demonstrated progressively more dissipation (up to 90%) and progressive wave characteristics, with increasing frequency. Much of the observed dissipation occurs very close to shore ($h < 0.8$ m) and the dependence of the reflection coefficient on a normalised bed slope parameter implies a mild sloping bed regime at these high infragravity frequencies, suggesting that the observed dissipation is dominated by wave breaking processes. This is supported by the results of bispectral analysis which show predominantly infragravity-infragravity interactions in shallow water and the development of infragravity harmonics indicative of steepening and eventual breaking of the infragravity waves.

This study presents the first simultaneous field observations of infragravity waves on a macrotidal, rocky shore platform and adjacent sandy beach. Infragravity wave dissipation is observed on both the platform and beach and occurs at statistically similar rates, demonstrating that frictional dissipation due to bed roughness is not the dominant dissipation mechanism, even in this extreme case. Sea-swell waves are also unaffected by the extreme roughness of the platform, with relative wave heights on the beach and platform ($\gamma = 0.38$ and 0.43 , respectively) scaling well with their respective gradients and are in very close agreement with formulations derived from sandy beaches. Overall, bed roughness is shown to have no significant impact on infragravity or sea-swell wave transformation, with offshore forcing and bed slope being the main controlling factors, particularly under moderate to high energy offshore forcing.

Author's Declaration

At no time during the registration for the degree of Doctor of Philosophy has the author been registered for any other University award without prior agreement of the Graduate Committee.

Work submitted for this research degree at Plymouth University has not formed part of any other degree either at Plymouth University or at another establishment.

This PhD was financed with the aid of a studentship from the School of Marine Science and Engineering (Plymouth University). Additional funding for conference attendance came from the Plymouth Marine Science and Education Foundation (PlyMSEF), Plymouth University's Marine Institute, and the Plymouth University Graduate School.

Data presented in Chapter 6 were collected during an experiment undertaken as part of the Waves Across Shore Platforms (WASP) project, funded by an Engineering and Physical Sciences Research Council grant (EP/L025191/1) awarded to Professor Gerd Masselink.

Relevant scientific workshops and conferences were attended at which work was presented through oral and poster presentations. Several papers have been written for publication in journals or as conference proceedings.

Word count of main body of thesis: 37,104

Signed.....

Date.....

PhD Outputs

Publications:

Bertin, X., De Bakker, A., Van Dongeren, A., Coco, G., Andre, G., Ardhuin, F., Bonneton, P., Bouchette, F., Castelle, B., Crawford, W., Davidson, M., Deen, M., Dodet, G., Guerin, T., Inch, K., Leckler, F., McCall, R., Muller, H., Olabarrieta, M., Roelvink, D., Ruessink, G., Sous, D., Stutzmann, E., Tissier, M. submitted. Infragravity waves: from driving mechanisms to impacts. *Earth Science Reviews*.

Inch, K., Davidson, M., Masselink, G., Russell, P. 2017. Observations of nearshore infragravity wave dynamics under high energy swell and wind-wave conditions. *Continental Shelf Research*, 138, 19-31.

Inch, K., Davidson, M., Masselink, G., Russell, P. 2017. Correcting wave reflection estimates in the coastal zone. *Coastal Engineering*, 119, 65-71.

Inch, K., Davidson, M., Masselink, G., Russell, P. 2016. Accurate estimation of wave reflection on a high energy, dissipative beach. *Journal of Coastal Research*, SI 75, 877-881.

Inch, K., Davidson, M., Masselink, G., Russell, P. 2015. Propagation and dissipation of infragravity waves on a dissipative beach with energetic wave forcing. *Proceedings of Coastal Sediments 2015*, World Scientific, San Diego, USA.

Inch, K., Masselink, G., Puleo, J.A., Russell, P., Conley, D.C. 2015. Vertical structure of near-bed cross-shore flow velocities in the swash zone of a dissipative beach. *Continental Shelf Research*, 101, 98-108.
Submitted during the first 12 months that the author was enrolled for Doctoral study but which is based upon research completed for an MSc in Applied Marine Science at Plymouth University (2012-2013).

Book chapters:

Inch, K.W. 2014. Section 3.2.3: Surf zone hydrodynamics: measuring waves and currents. In: Cook, S.J., Clarke, L.E. and Nield, J.M. (Eds.) *Geomorphological Techniques (Online Edition)*. British Society of Geomorphology, London. ISSN: 2047-0371.

Other presented work:

Inch, K., Davidson, M., Masselink, G., Russell, P. 2016. Correcting infragravity wave reflection estimates on a dissipative beach. *Infragravity waves: from driving mechanisms to impacts, La Rochelle, France, 17-18 March 2016*. Oral presentation and abstract.

Inch, K., Davidson, M., Masselink, G., Russell, P. 2016. Accurate estimation of wave reflection on a high energy dissipative beach. *14th International Coastal Symposium, Sydney, Australia, 7-11 March 2016*. Oral presentation and peer-reviewed journal paper.

Inch, K., Davidson, M., Masselink, G., Russell, P. 2016. Wave transformation on rocky shore platforms. *Making Waves 2016, Plymouth, UK, 11 February 2016*. Oral presentation and abstract.

Inch, K., Davidson, M., Masselink, G., Russell, P. 2015. Propagation and dissipation of infragravity waves on a dissipative beach with energetic wave forcing. *Coastal Sediments 2015, San Diego, USA, 11-15 May 2015*. Poster presentation and conference proceedings.

Inch, K., Davidson, M., Masselink, G., Russell, P. 2015. Field observations of infragravity waves on a dissipative, macrotidal beach. *Surf Beats and Earth's Hum workshop, Brest, France, 12-13 March 2015*. Oral presentation and abstract.

Inch, K., Davidson, M., Masselink, G., Russell, P. 2014. Infragravity wave dynamics under storm conditions: a pilot study. *Young Coastal Scientists and Engineers Conference (YCSEC), Cardiff, UK, 14-15 April 2014*. Poster presentation and abstract.

Grants awarded:

Plymouth Marine Science and Education Foundation (PlyMSEF), Grant-in-aid 2016. £400 awarded to attend the Infragravity waves: from driving mechanisms to impacts workshop in La Rochelle, France.

Plymouth University Marine Institute Education Fund, Grant-in-aid 2016. £300 awarded to attend the 14th International Coastal Symposium in Sydney, Australia.

Plymouth University Graduate School, Doctoral Training Centre (DTC) funding. £190 awarded to attend the Coastal Sediments 2015 conference in San Diego, USA.

Plymouth Marine Science and Education Foundation (PlyMSEF), Grant-in-aid 2015. £400 awarded to attend the Coastal Sediments 2015 conference in San Diego, USA.

Contents

List of figures.....	x
List of tables	xviii
List of symbols and abbreviations	xix
Acknowledgements.....	xxiv
1. Introduction.....	1
1.1 Preamble	1
1.2 Aim and objectives.....	5
1.3 Thesis structure	6
2. Literature Review.....	8
2.1 Infragravity wave generation	8
2.1.1 <i>Bound wave theory</i>	9
2.1.1.1 <i>Bound wave shoaling</i>	11
2.1.1.2 <i>Bound wave release</i>	14
2.1.2 <i>Time-varying breakpoint theory</i>	16
2.1.3 <i>Relative importance of bound and breakpoint forced infragravity waves</i>	16
2.1.4 <i>Infragravity frequency range</i>	20
2.1.5 <i>Other low frequency waves</i>	20
2.2 Parameterizing nearshore infragravity wave height.....	21
2.3 Dissipation and reflection	23
2.3.1 <i>Bed friction</i>	25
2.3.2 <i>Non-linear energy transfer</i>	26
2.3.3 <i>Infragravity wave breaking</i>	26
2.3.4 <i>Normalised bed slope parameter</i>	28
2.3.5 <i>Wave reflection analysis</i>	30
2.4 Infragravity waves on rocky shore platforms	31
2.4.1 <i>Previous research on Type B platforms</i>	33
2.4.2 <i>Coral reef studies</i>	34
2.4.3 <i>Waves Across Shore Platforms (WASP) project</i>	35
2.5 Summary.....	36

3. Methodology	38
3.1 Study sites.....	38
3.1.1 Perranporth.....	38
3.1.2 Freshwater West.....	40
3.2 Experimental Set-up.....	42
3.2.1 Perranporth.....	42
3.2.2 Freshwater West.....	43
3.3 Post-processing.....	48
3.4 Data analysis.....	51
3.4.1 Frequency domain analysis.....	51
3.4.1.1 The auto-spectrum.....	51
3.4.1.2 The cross-spectrum.....	54
3.4.1.3 Reflection analysis.....	55
3.4.1.4 The bispectrum.....	57
3.4.1.5 Significant wave height.....	59
3.4.2 Time domain analysis.....	60
3.4.2.1 Wave group envelope and the groupiness factor.....	60
3.4.2.2 Cross-correlation.....	61
3.5 Summary.....	62
4. Correcting for noise in wave reflection measurements	64
4.1 Background.....	65
4.2 Methodology.....	67
4.3 Results.....	71
4.3.1 Noise correction.....	71
4.3.2 Confidence intervals.....	74
4.3.3 Application to simulated data.....	76
4.3.4 Wave angle and directional spreading.....	78
4.4 Discussion.....	82
4.4.1 Application to field data.....	82
4.5 Conclusion.....	85
4.6 List of chapter specific symbols.....	86

5. Infragravity waves during swell and wind-sea (Perranporth experiment).....	88
5.1 Experimental conditions	88
5.1.1 Offshore wave conditions	88
5.1.2 Alongshore hydrodynamics	89
5.1.3 Short waves in the surf zone	91
5.2 Results	91
5.2.1 Basic hydrodynamic statistics	91
5.2.2 Generation and forcing.....	92
5.2.3 Propagation, dissipation, and reflection.....	96
5.3 Discussion.....	106
5.3.1 Relationship with offshore forcing.....	106
5.3.2 Infragravity dissipation.....	109
5.3.3 Non-linear energy transfer.....	110
5.4 Conclusion	112
6. Effect of bed roughness on infragravity waves (Freshwater West experiment)	114
.....	
6.1 Experimental conditions	114
6.1.1 Offshore wave conditions	114
6.1.2 Alongshore hydrodynamics	115
6.2 Results and discussion.....	117
6.2.1 Basic hydrodynamic statistics	117
6.2.2 Generation and parameterization by offshore forcing	118
6.2.3 Sea-swell wave propagation.....	123
6.2.4 Infragravity wave propagation, transformation and reflection	125
6.3 Conclusion	134
7. Discussion and conclusion	136
7.1 Discussion and wider context	136
7.1.1 Noise correction in wave reflection analysis	136
7.1.2 Infragravity waves during swell and wind-sea.....	138
7.1.3 Implications for sediment transport.....	141
7.1.4 Infragravity waves and bed roughness	143
7.2 Thesis conclusions	145

References	148
Appendix A	159
Appendix B.....	165
Appendix C	165
Appendix D	165
Appendix E.....	165

List of figures

- Figure 1.1.** An infragravity swash event (A) and storm erosion (B) at Summerlease Beach, Bude (UK), during storm Hercules in January 2014. 3
- Figure 2.1.** Two sinusoidal wave trains of slightly different frequencies ($\eta_1 = 0.09$ Hz and $\eta_2 = 0.08$ Hz) but the same amplitude (A), and the resulting wave groups and bound infragravity wave at the difference frequency ($\eta_3 = 0.01$ Hz) (B). 9
- Figure 2.2.** Incident (triangles) and reflected (dots) significant wave height H_s for frequency bands 0.04-0.06 Hz (A), 0.10-0.12 Hz (B), and 0.16-0.18 Hz (C), versus cross-shore location. Lower dashed curve in each plot is Green's law ($H \sim h - 1/4$) fitted to reflected wave heights in the zone offshore from $x = 20$ m, and upper dashed curves are the Longuet-Higgins and Stewart (1962) asymptote ($H \sim h - 5/2$) initiated with the wave height at $x = 8$ m. Note that the frequency bands are higher than conventional infragravity frequencies due to the high frequency of the primary waves used in the laboratory experiments. Source: Battjes et al. (2004). 13
- Figure 2.3.** Cross-correlation coefficient at zero time lag r_0 between the wave group envelope and infragravity motion as a function of the local relative wave height H_{ss}/h (A). Cross-shore change in r_0 between the wave group envelope and infragravity motion for low (open squares), moderate (solid triangles), and high (open circles) energy conditions (B). Cross-shore profile of the study site showing measurement locations (C). Horizontal dashed lines in (A) and (B) are the 95% confidence levels on $r_0 = 0$. Vertical dashed line in (A) indicates the onset of short wave breaking at $H_{ss}/h = 0.33$. Source: Ruessink (1998a). 15
- Figure 2.4.** Cross-correlation between the wave group envelope and infragravity motion at the same locations (A) and between the wave group envelope at $x = 0$ m and infragravity motion at all locations (B). Lines with circular markers indicate the time lag for incident waves propagating at the wave group celerity C_g , and lines with square markers indicate the time lag for reflected waves reflected at $x = 30$ m propagating at the shallow water wave speed gh . Source: Janssen et al., 2003. 19
- Figure 2.5.** Infragravity energy S_{inf} as a function of total offshore sea-swell energy S_{ss} 0.04-0.33 Hz (A), offshore swell energy S_{swell} 0.04-0.14 Hz (B), and offshore sea energy S_{sea} 0.14-0.33 Hz (C). Straight lines are least squares fits. Infragravity runup elevation S_{ig} parameterized by the offshore forcing parameter $(H_o L_o)_{0.5}$ (D). Lines are best linear fits. Dashed line in (D) is the best linear fit from Stockdon et al. (2006). Source: Ruessink (1998a) (A-C) and Senechal et al. (2011) (D). 22
- Figure 2.6.** Shoreline amplitude reflection coefficient R for various infragravity frequencies as a function of the normalised bed slope parameter βH on a laboratory beach (A), and gentle (B) and steep (C) sloping natural beaches. The solid line in all plots is

$\min(1, R = 2\pi\beta H^2)$. Source: Van Dongeren et al. (2007) (A) and De Bakker et al. (2014) (B-C). 30

Figure 2.7. Cross-sectional schematics of Type A (A) and Type B (B) shore platforms (from Ogawa et al., 2012). Example of a Type A shore platform at Hartland Quay, UK (C), and an example of a Type B shore platform at Leigh, New Zealand (D). 32

Figure 3.1. Location map of Perranporth Beach, UK (A), aerial image of Perranporth Beach taken around low tide (B), and photograph taken from the top of the instrument array line (C). Solid red line in (B) indicates the instrument array location and is ~500 m long. The high tide line in (B) is also clear as the change in sand colour. 40

Figure 3.2. Location map of Freshwater West, UK (A), aerial image of Freshwater West (B), and photographs illustrating the beach (C) and platform (D) study areas. The solid and dotted red lines in (B) are the beach and platform instrument arrays, respectively, and represent a distance of ~150 m. 41

Figure 3.3. Mean beach profile during the Perranporth field experiment showing the positions of the buried pressure sensors (PT) and the co-located pressure and velocity rig (PUV). Elevation is relative to Ordnance Datum Newlyn (ODN), which is ~0.2 m above mean sea level in the southwest of England. Horizontal lines indicate mean sea level (MSL), mean high water springs (MHWS), and mean low water springs (MLWS). 43

Figure 3.4. Beach (A) and platform (B) profiles during the Freshwater West field experiment showing the positions of the pressure sensors (PT) and the co-located pressure and velocity rigs (PUV). Elevation is relative to Ordnance Datum Newlyn (ODN). Horizontal lines indicate mean high water springs (MHWS) and mean low water springs (MLWS). 46

Figure 3.5. Detrended digital elevation models (DEMs) with pressure sensor locations (black dots) for the platform (A) and beach (B) at Freshwater West. Cross-shore variation in alongshore averaged roughness based on standard deviation $K\sigma$ and rugosity KR for the platform (C, E, respectively) and beach (D, F, respectively). Offshore (west) is at the top of the figures. The colour scale of the DEMs goes from -1 m (dark blue) to +1 m (yellow). 48

Figure 3.6. Example of a detrended sea-swell time series η_{SS} and associated wave group envelope $A(t)$, obtained through the method of List (1991), from tide 27 ($H_o = 0.67$ m, $T_p = 11.4$ s, $h = 4.07$ m) of the Perranporth field experiment. 60

Figure 4.1. Estimated incident $S +$ and reflected $S -$ auto-spectra estimated using the array set-ups given in Table 4.1 optimized for frequency ranges 0.01-0.05 Hz (A), 0.05-0.20 Hz (B), and 0.20-0.33 Hz (C). Shaded areas indicate the frequency ranges used to form the concatenated auto-spectra (D). Dotted lines indicate the target incident $S +$ and reflected $S -$ auto-spectra. In this example, wave amplitude is 1 m and $R = 0.5$ 70

Figure 4.2. Estimated incident $S +$ and reflected $S -$ spectra (A-D), coherence (E-H), and estimated reflection coefficients R (I-L) for SNR = Inf, 2.5, 1.7, and 0.7 as stated on the figure. Dashed lines in (A-D) are the target incident $S +$ and reflected $S -$ spectra. Red dashed line in (E-H) is the 95% confidence threshold on coherence of 0.45 for 12 degrees of freedom (Shumway and Stoffer, 2000). Red dashed line in (I-L) is the target reflection coefficient R of 0.3. Wave amplitude is 2 m. 72

Figure 4.3. Normalised bias ϵ ($\epsilon S +$, where ϵ is bias) versus coherence for all wave amplitudes, true reflection coefficients, and SNRs. Data have been smoothed providing one estimate per simulation and 984 degrees of freedom. Solid red line is an exponential regression function with coefficients and accuracy given on the figure. 73

Figure 4.4. 95% confidence intervals on normalised bias $\Delta\epsilon$ for various degrees of freedom versus coherence (A). Solid lines are linear regression lines fit to the data of the corresponding colour. Slopes m (B) and intercepts b (C) from the linear regression lines shown in (A) versus degrees of freedom. Solid red lines in (B) and (C) are exponential regression functions with coefficients and accuracy given on the figure. 75

Figure 4.5. Deviation (%) of uncorrected $S +$ and corrected $Sc +$ incident spectra from the target value $S +$ (A-C). Coherence (D-F), and uncorrected R and corrected Rc reflection coefficients (G-I). Shaded areas in (A-C) are 95% confidence intervals on $Sc +$ and shaded areas in (G-I) are 95% confidence intervals on Rc . SNRs are 5.0, 2.5, and 1.7 as stated on the figure. Red dashed line in (D-F) is the 95% confidence threshold on coherence of 0.45 for 12 degrees of freedom (Shumway and Stoffer, 2000). Red dashed line in (G-I) is the target reflection coefficient R of 0.5. Wave amplitude is 3 m. 77

Figure 4.6. Normalised bias ϵ ($\epsilon S +$, where ϵ is bias) versus coherence for unidirectional waves of various angles, as given by the figure legend. Data have been smoothed providing 984 degrees of freedom. Solid red line is the exponential regression function, with coefficients given on the figure, defined in Figure 4.3 and that forms the basis of the noise correction technique (Equations 4.4-4.7). Circles correspond to the normalised bias on incident spectral estimates and triangles are the normalised bias on reflected spectral estimates. 79

Figure 4.7. Normalised bias ϵ ($\epsilon S +$, where ϵ is bias) versus coherence for directionally spread waves between $\pm 45^\circ$ and $\pm 90^\circ$, as given by the figure legend. Data have been smoothed providing 984 degrees of freedom. Solid red line is the exponential regression function, with coefficients given on the figure, defined in Figure 4.3 and that forms the basis of the noise correction technique (Equations 4.4-4.7). Circles correspond to the normalised bias on incident spectral estimates and triangles are the normalised bias on reflected spectral estimates. 81

Figure 4.8. Data from the inner surf zone of Perranporth Beach, UK ($H_o = 1.85$ m, $T_p = 10.8$ s). Corrected incident $Sc +$ and reflected $Sc -$ spectra, and uncorrected incident $S +$ and reflected $S -$ spectra (A). Coherence (B) and corrected Rc and uncorrected R estimated reflection coefficients (C). Shaded areas in (A) are 95% confidence intervals

on $Sc +$ and $Sc -$ and error bars in (C) are 95% confidence intervals on Rc . Red dashed line in (B) is the 95% confidence threshold on coherence of 0.45 for 12 degrees of freedom (Shumway and Stoffer, 2000)..... 83

Figure 4.9. Data from the inner surf zone of Perranporth Beach, UK ($H_o = 1.85$ m, $T_p = 10.8$ s). Corrected incident $Fc +$ and reflected $Fc -$ infragravity energy flux, and uncorrected incident $F +$ and reflected $F -$ infragravity energy flux (A). Corrected $Rc2$ and uncorrected $R2$ infragravity energy (i.e., squared) reflection coefficients (B)..... 85

Figure 5.1. Offshore wave conditions during the study period, measured by a Datawell Directional Waverider buoy at a depth of approximately -17 m ODN. Significant wave height H_o (A), spectral peak period T_p (B), and tidal elevation relative to mean sea level (C). 89

Figure 5.2. Ratio between the alongshore V_{inf2} and cross-shore U_{inf2} velocity variance in the infragravity band (A), and the percentage of shear wave contributions to the total infragravity velocity variance U_{sh2} (B), for the 10 tides during which the PUV rig was deployed in the Perranporth field experiment. Horizontal lines in (A) and (B) indicate 0.5 and 50%, respectively. Shear wave contributions were calculated following Lippmann et al. (1999)..... 90

Figure 5.3. Infragravity wave height H_{inf} for $0 < h/h_b < 0.33$ versus offshore significant wave height H_o (A), offshore significant wave height in the swell frequency band H_{swell} (B), and $H_o 2 T_p$ (C). Black lines are best-fit linear regression lines with coefficients of determination given on the figure and regression coefficients given in Table 5.2..... 94

Figure 5.4. Cross-correlation between the wave group envelope at the most seaward sensor and the infragravity wave time series at all locations during tide 7 ($H_o = 1.05$ m, $T_p = 10.8$ s). The dashed black line is the predicted time lag for an incident and reflected wave propagating at gh . The solid black line represents a time lag of 0 s and the horizontal dotted line shows the location of the short wave breakpoint at $h/h_b \approx 1$. Red indicates positive correlations and blue indicate negative correlations..... 96

Figure 5.5. Bulk incident infragravity energy flux ($F +$) normalised by the mean value ($F +$) for each tide (A), correlation coefficient at zero time lag r_0 between the wave group envelope and the infragravity time series (B), and groupiness factor GF (C), versus normalised surf zone width h/h_b for all locations during all tides. Dashed vertical lines indicate the seaward limit of the surf zone at $h/h_b = 1$. Only r_0 values significant at the 95% level are shown in (B). 98

Figure 5.6. Example sea-swell time series η_{ss} from tide 27 ($H_o = 0.67$ m, $T_p = 11.4$ s) at three normalised surf zone h/h_b locations; 1.24 (A), 0.68 (B), and 0.18 (C). The dotted black line is the wave group envelope. Colour represents the infragravity water surface elevation η_{inf} with warm colours indicating infragravity wave crests and cool colours indicating infragravity wave troughs. Note the different axis scales..... 99

Figure 5.7. Offshore wave spectra at the wave buoy (A-C) and surf zone wave spectra at $h \approx 2$ m (D-F), for tides 10 (left panels), 1 (middle panels), and 20 (right panels). Shaded areas are 95% confidence intervals. 100

Figure 5.8. Sea-swell H_{ss} (dots) and infragravity H_{inf} (circles) significant wave height (A-C), bulk incident $F +$ (dots) and reflected $F -$ (circles) infragravity energy flux (D-F), bulk incident $D +$ (dots) and reflected $D -$ (circles) infragravity dissipation rate (G-I), and bulk infragravity reflection coefficient R_2 (J-L), versus water depth h for tides 10 (left panels), 1 (middle panels), and 20 (right panels). Mean 95% confidence intervals on $F \pm$, calculated following the method outlined in Section 4.4.1, are $\pm 0.0013 \text{ m}^3 \text{ s}^{-1}$, $\pm 0.0010 \text{ m}^3 \text{ s}^{-1}$, and $\pm 0.0006 \text{ m}^3 \text{ s}^{-1}$ for tides 10, 1, and 20, respectively. Mean 95% confidence intervals on R_2 are ± 0.040 , ± 0.024 , and ± 0.034 for tides 10, 1, and 20, respectively. 102

Figure 5.9. Non-dimensional amplitude M (A-C), phase (D-F), and reflection coefficients R_2 (G-I) versus distance offshore for $f = 0.0078$ Hz (left panels), $f = 0.0195$ Hz (middle panels), and $f = 0.0391$ Hz (right panels). Black dots are tide 10, grey dots are tide 1, and circles are tide 20. M and phase are associated with the dominant Empirical Orthogonal Function (EOF), computed following Henderson et al. (2000). Error bars in G-I are 95% confidence intervals on R_2 following the method outlined in Section 4.4.1. 104

Figure 5.10. Bulk amplitude reflection coefficients R for the total infragravity band (A) and for partitioned infragravity bands (B) versus the normalised bed slope parameter βH . The solid black lines are $\min(1, R = 0.2\pi\beta H^2)$, following Van Dongeren et al. (2007). Error bars in B are 95% confidence intervals on R following the method outlined in Section 4.3.2. The R values in A have 95% confidence intervals that are too small to be included on the figure, with mean and maximum confidence intervals of ± 0.020 and ± 0.034 , respectively. 106

Figure 5.11. Imaginary part of the bispectrum from tide 10 ($H_o = 2.96$ m, $T_p = 15.4$ s) at three normalised surf zone h/h_b locations; 0.44 (A), 0.27 (B), and 0.11 (C). Where the corresponding bicoherence is below the 95% significant threshold of 0.18, bispectral estimates are set to zero. Solid black lines indicate the transition between infragravity and sea-swell frequency bands. Dashed lines indicate the offshore peak period and its higher harmonics. 112

Figure 6.1. Offshore wave conditions during the study period measured by a Datawell Directional Waverider buoy at an approximate depth of -40 m ODN. Significant wave height H_o (A), spectral peak period T_p (B), and wave direction θ (C). The dashed line in (C) represents shore-normal incidence (245°). 115

Figure 6.2. Ratio between the alongshore V_{inf2} and cross-shore U_{inf2} velocity variance in the infragravity band (A, C), and the percentage of shear wave contributions to the total infragravity velocity variance U_{sh2} (B, D), for the beach (left panels) and platform (right panels), during the Freshwater West field experiment. Horizontal lines in

(A, C) and (B, D) indicate 0.5 and 50%, respectively. Values above these thresholds are shown in red and all data from these bursts are rejected from further analysis. Shear wave contributions were calculated following Lippmann et al. (1999)..... 116

Figure 6.3. Infragravity wave height H_{inf} for $0 < h/hb < 0.33$ versus offshore significant wave height H_o (A,B) and H_o2Tp (C,D) on the beach (left panels) and platform (right panels). Black lines are best-fit linear regression lines with coefficients of determination given on the figure and regression coefficients given in Table 6.2. Red lines are the best fit linear regression lines for the Perranporth dataset with coefficients given in Table 6.2. 118

Figure 6.4. H_o2Tp during the study period measured by a Datawell Directional Waverider buoy at an approximate depth of -40 m ODN (A), infragravity wave height H_{inf} (B), and water depth h (C) at similar elevations on the beach and the platform. 121

Figure 6.5. Correlation coefficient at zero time lag r_0 between the wave group envelope and the infragravity time series versus h/hb on the beach (A) and platform (B). Box plots of r_0 versus h/hb (C). Boxes represent a bin width of 0.1. On each box, the central line is the median, box edges are the 25th and 75th percentiles, and whiskers extend to the most extreme values not considered outliers ($< 0.4^{\text{th}}$ percentile or $> 99.6^{\text{th}}$ percentile). Notches in the boxes indicate the 95% confidence intervals on the median (i.e., medians are not significantly different if notches overlap). For ease of comparison, platform boxes are offset on the x-axis by 0.04. Dashed vertical lines indicate the seaward limit of the surf zone at $h/hb = 1$. Only r_0 values significant at the 95% level are shown. 122

Figure 6.6. Sea-swell wave height H_{ss} versus water depth h on the beach (A) and platform (B). Box plots of H_{ss} versus h (C). Boxes represent a bin width of 0.5 m. For a description of the boxes, see Figure 6.5. For ease of comparison, platform boxes are offset on the x-axis by 0.13 m. Colour in (A) and (B) represents H_o . Solid lines in (A) and (B) are linear regression lines fit to the data, omitting values corresponding to $h/hb > 1$, from which the breaker index γ is derived and given on the figure. Dashed lines in (A) and (B) correspond to the 95% confidence intervals on γ 124

Figure 6.7. Infragravity wave height H_{inf} versus h/hb on the beach (A) and platform (B). Box plots of H_{inf} versus h/hb (C). Box plots represent a bin width of 0.1. For a description of the boxes, see Figure 6.5. For ease of comparison, platform boxes are offset on the x-axis by 0.04. Dashed vertical lines indicate the seaward limit of the surf zone at $h/hb = 1$. Colour in (A) and (B) represents H_o2Tp 126

Figure 6.8. Percentage of total variance in the infragravity band $IG\%$ versus water depth h on the beach (A) and platform (B). Box plots of $IG\%$ versus h (C). Boxes represent a bin width of 0.5 m. For a description of the boxes, see Figure 6.5. For ease of comparison, platform boxes are offset on the x-axis by 0.13 m. Colour in (A) and (B) represents H_o2Tp 128

Figure 6.9. Bulk incident infragravity energy flux $F +$ normalised by the mean value $F +$ versus h/hb on the beach (A) and platform (B). Box plots of $F +/F +$ versus h/hb (C).

Box plots represent a bin width of 0.1. For a description of the boxes, see Figure 6.5. For ease of comparison, platform boxes are offset on the x-axis by 0.04. Dashed vertical lines indicate the seaward limit of the surf zone at $h/h_b = 1$ 129

Figure 6.10. Bulk incident infragravity dissipation rate $D +$ versus h/h_b on the beach (A) and platform (B). Box plots of $D +$ versus h/h_b (C). Box plots represent a bin width of 0.1. For a description of the boxes, see Figure 6.5. For ease of comparison, platform boxes are offset on the x-axis by 0.04. Dashed vertical lines indicate the seaward limit of the surf zone at $h/h_b = 1$. Colour in (A) and (B) represents h 130

Figure 6.11. Sea-swell significant wave height H_{ss} (A-C), infragravity significant wave height H_{inf} (D-F), bulk incident infragravity energy flux $F +$ (G-I), and bulk incident infragravity dissipation rate $D +$ (J-L), versus water depth h for tide 30 ($H_o = 3.18$ m, $T_p = 12.6$ s). Left panels are the beach, middle panels are the platform, and right panels are bin-averaged values for the beach and the platform using a bin width of 0.5. Mean 95% confidence intervals on $F +$, calculated following the method outlined in Section 4.4.1, are ± 0.0005 m³ s⁻¹ and ± 0.0007 m³ s⁻¹ for the beach and platform, respectively. 131

Figure 6.12. Bulk amplitude reflection coefficients R for partitioned infragravity bands versus the normalised bed slope parameter βH for the beach (A) and platform (B). The solid black lines are $\min(1, R = 0.2\pi\beta H^2)$, following Van Dongeren et al. (2007). Maximum 95% confidence intervals on beach values of R , calculated following the method outlined in Section 4.3.2, are ± 0.05 , ± 0.01 , and ± 0.004 for the frequency ranges 0.005-0.017 Hz, 0.017-0.028 Hz, and 0.028-0.04 Hz, respectively. The same confidence intervals for the platform values of R are ± 0.02 , ± 0.009 , and ± 0.008 , respectively..... 133

Figure 7.1. Conceptual model illustrating the change in infragravity wave characteristics with changing cross-shore location relative to the surf zone. In the top part of the figure, the black and red (dashed) wave trains represent the sea-swell waves and infragravity motion, respectively. Elsewhere, blue, red, and black colours represent high ($H_o 2T_p > 150$ m²s), medium ($50 < H_o 2T_p < 150$ m²s), and low ($H_o 2T_p < 50$ m²s) levels of offshore forcing, respectively. For a full glossary of the symbols used in the figure, refer to the List of symbols and abbreviations on page xix. The values corresponding to various parameters are approximate and provided as a guide. 141

Figure 7.2. Conceptual figure for sand suspension mechanisms and resulting transport directions for a gently sloping beach, from De Bakker et al. (2016b) (A). Ratio of infragravity wave height to sea-swell wave height H_{inf}/H_{ss} versus water depth h at Perranporth (B), Freshwater West beach (C), and Freshwater West platform (D). Colour in (B-D) represents $H_o 2T_p$ 143

Figure A1. Estimated incident $S +$ and reflected $S -$ spectra (A-D), coherence (E-H), and estimated reflection coefficients R (I-L) for SNR = Inf, 2.5, 1.7, and 0.7 as stated on the figure. Dashed lines in (A-D) are the target incident $S +$ and reflected $S -$ spectra. Red dashed line in (E-H) is the 95% confidence threshold on coherence of 0.45 for 12

degrees of freedom (Shumway and Stoffer, 2000). Red dashed line in (I-L) is the target reflection coefficient R of 0.3. Wave amplitude is 2 m. 160

Figure A2. Normalised bias ϵ ($\epsilon S +$, where ϵ is bias) versus coherence for all wave amplitudes, true reflection coefficients, and SNRs. Data have been smoothed providing one estimate per simulation and 984 degrees of freedom. Solid red line is an exponential regression function with coefficients and accuracy given on the figure. Dashed red line is the exponential regression function used in the correction technique for the Gaillard et al. (1980) method, defined in Figure 4.3. 161

Figure A3. 95% confidence intervals on normalised bias $\Delta\epsilon$ for various degrees of freedom versus coherence (A). Solid lines are linear regression lines fit to the data of the corresponding colour. Slopes m (B) and intercepts b (C) from the linear regression lines shown in (A) versus degrees of freedom. Solid red lines in (B) and (C) are exponential regression functions with coefficients and accuracy given on the figure. 162

Figure A4. Deviation (%) of uncorrected $S +$ and corrected $S_c +$ incident spectra from the target value $S +$ (A-C). Coherence (D-F), and uncorrected R and corrected R_c reflection coefficients (G-I). Shaded areas in (A-C) are 95% confidence intervals on $S_c +$ and shaded areas in (G-I) are 95% confidence intervals on R_c . SNRs are 10.0, 3.3, and 2.0 as stated on the figure. Red dashed line in (D-F) is the 95% confidence threshold on coherence of 0.45 for 12 degrees of freedom (Shumway and Stoffer, 2000). Red dashed line in (G-I) is the target reflection coefficient R of 0.3. Wave amplitude is 4 m. 164

List of tables

Table 3.1. Auto-spectra processing details for Perranporth and Freshwater West.	53
Table 4.1. Cross-shore sensor locations $x_1 - 3$ used in the array set-ups optimized for frequency ranges 0.01-0.05 Hz, 0.05-0.20 Hz, and 0.20-0.33 Hz, respectively. The shoreline is at $x = 0$	70
Table 4.2. Summary of mean errors in estimated and corrected incident spectra and reflection coefficients for a wave amplitude of 3 m, known reflection coefficient of 0.5, and SNRs between infinity and 1. Errors in the estimated and corrected incident spectra, and 95% confidence intervals on corrected incident spectra, are given in terms of percentage of the target value $S +$	77
Table 5.1. Overview of basic hydrodynamic statistics (recorded during all tides and at all locations).	92
Table 5.2. Regression parameters relating to linear fits between H_{inf} and various offshore forcing parameters. All coefficients of determination r^2 are significant at the 95% level.	94
Table 5.3. Summary of environmental parameters during tides 10, 1, and 20.	99
Table 6.1. Overview of basic hydrodynamic statistics on the beach and platform (recorded during all tides and at all locations).	117
Table 6.2. Regression parameters relating to linear fits between H_{inf} and various offshore forcing parameters. All coefficients of determination r^2 are significant at the 95% level.	120

List of symbols and abbreviations

$A(t)$	Wave group envelope (List, 1991)
A_{inf}	Infragravity amplification
A_a	Geometric surface area of DEM square tiles (1 m ²)
A_r	Actual surface area of DEM square tiles
a	Wave amplitude
B_{f_1, f_2}	Discrete bispectrum
b_{f_1, f_2}^2	Bicoherence
$b_{95\%}^2$	95% confidence interval on bicoherence
b	Intercept of linear regression model
C_{xy}	Spectral coherence between time series x and y
$C_{95\%}$	Confidence threshold for significant coherence
Co_{xy}	Co-spectra between time series x and y
c	Shallow water wave velocity (\sqrt{gh})
c_g	Wave group velocity
D_{50}	Median grain size
D^+	Incident infragravity dissipation rate
D^-	Reflected infragravity dissipation rate
df	Frequency bandwidth
dt	Sampling interval
$E[]$	Ensemble average function
F^+	Incident infragravity energy flux
F^-	Reflected infragravity energy flux
f	Frequency
f_s	Sampling frequency (1/ dt)
GF	Groupiness factor (List, 1991)

g	Gravitational acceleration (9.81 m s ⁻²)
H	Theoretical wave height
H_o	Offshore significant wave height
H_{swell}	Offshore significant wave height in the frequency band 0.04-0.14 Hz
H_{sea}	Offshore significant wave height in the frequency band 0.14-0.33 Hz
H_{inf}	Infragravity significant wave height
H_{SS}	Sea-swell (0.04-0.33 Hz) significant wave height
H_b	Breaking significant wave height
H^+	Incident infragravity significant wave height
H^-	Reflected infragravity significant wave height
h	Water depth
h_b	Water depth at the sea-swell wave breakpoint
hf	High frequency cut-off
K	Depth attenuation factor
K_σ	Roughness parameter based on standard deviation
K_R	Roughness parameter based on rugosity
k	Frequency-dependent wave number ($2\pi/L$)
L	Wavelength
L_o	Deep water wavelength
l	Segment length
lf	Low frequency cut-off
M	Non-dimensional amplitude in EOF analysis (Henderson et al., 2000)
m	Slope of linear regression model
N	Time series length
P	Periodogram estimate
P_0	Hydrostatic pressure
P_{wave}	Wave-induced pressure
P_{zb}	Pressure below the bed

Q_{xy}	Quadrature spectra between time series x and y
R	Amplitude reflection coefficient
R^2	Energy reflection coefficient
r	Cross-correlation coefficient
r_{xy}	Auto-correlation coefficient
r^0	Correlation coefficient at zero time lag
r^2	Coefficient of determination (linear regression model)
S	Auto-spectra
S^+	Incident auto-spectra
S^-	Reflected auto-spectra
S_{inf}	Spectral variance in the infragravity frequency band
S_{ss}	Spectral variance in the sea-swell (0.04-0.33 Hz) frequency band
S_{sea}	Spectral variance in the frequency band 0.14-0.33 Hz
S_{swell}	Spectral variance in the frequency band 0.04-0.14 Hz
S_{xy}	Cross-spectra between time series x and y
S_{ig}	Infragravity runup elevation
S_{xx}	Cross-shore component of radiation stress
T	Wave period of incident infragravity wave
T_p	Peak wave period
t	Time
U_{inf}^2	Cross-shore velocity variance in the infragravity band
U_{sh}^2	Shear wave contributions to the total infragravity velocity variance
u_x	Particle velocity
V_{inf}^2	Alongshore velocity variance in the infragravity band
$X(f)$	Theoretical time series (frequency domain)
x	Cross-shore distance coordinate
$x(t)$	Theoretical time series (time domain)

z	Vertical distance coordinate
z_b	Depth of pressure sensor below the bed
α	Significance level (herein 0.05)
β	Bed slope
β_b	Normalised bed slope parameter (Battjes et al., 2004)
β_H	Normalised bed slope parameter (Van Dongeren et al., 2007)
γ	Breaker index
γ_b	Breaker coefficient (at the breakpoint)
ϵ	Spectral bias
F	Inverse of the cumulative distribution function of the F-distribution
\mathcal{F}	Complex Fourier coefficient
η	Water surface elevation time series
η_{inf}	Infragravity water surface elevation time series
η_{ss}	Sea-swell water surface elevation time series
θ	Wave direction
θ_{xy}	Phase spectra between time series x and y
ν	Degrees of freedom
ξ	Iribarren number (Battjes, 1974)
$\xi_{surfbeat}$	Surf beat similarity parameter (Baldock, 2012)
ρ	Fluid density
σ	Standard deviation
σ_z	Standard deviation of DEM square tiles
τ	Time shift
\mathcal{T}	Predicted travel time of infragravity wave
χ^2	Chi-squared distribution
ϕ	Wave phase
ω	Wave angular frequency ($2\pi f$)

Δx	Sensor spacing
DEM	Digital elevation model
DGPS	Differential global positional system
EOF	Empirical Orthogonal Function
MHWS	Mean high water springs
MLWS	Mean low water springs
ODN	Ordnance Datum Newlyn
PT	Pressure sensor
PUV	Co-located pressure and velocity instrument rig
RMSE	Root-mean-squared error
SNR	Signal-to-noise ratio
TR	Tidal range

Acknowledgements

First and foremost, I would like to thank my supervisory dream team of Mark Davidson, Gerd Masselink, and Paul Russell for their continued encouragement and support. Mark has been a constant source of enthusiasm and excellent advice since day one and it was through his wealth of knowledge and guidance that I was able to complete this PhD. Any questions or queries I had about my work (or about triathlon) were quickly answered by Mark and he always knew which direction I should take my research. Mark has also shown great patience after having to explain spectral analysis to me about 50 times throughout the past 3 years. I first met Gerd over 10 years ago during my first week of university as an undergraduate and have been fortunate enough to have him as a project supervisor at undergraduate, masters, and PhD level. Gerd's enthusiasm for coastal research is unparalleled, especially in the field, and I'm sure that I wouldn't have pursued marine science had I not been allocated Gerd as a personal tutor back in 2005 freshers week. Paul is always very positive and would consistently turn up to meetings with a smile. He has a great ability to point out what is interesting and significant about certain results, as well as being able to make complicated theories sound simple.

The highlight of my PhD has been the field campaigns that I have been involved with, from stormy Westward Ho! to tropical New Zealand. I shared these experiences with a number of great people, but I owe a special thanks to Tim Poate and Pedro Almeida for teaching me so much about fieldwork techniques and helping with subsequent data processing. Tim especially has helped me a lot and was always great company during the longer field campaigns. I am also grateful to Peter Ganderton for providing the best technical support and always being on the end of the phone whenever there were problems with the kit.

Throughout the past 3.5 years I have shared the office with lots of entertaining and like-minded people that were always up for a laugh and made the endless hours of Matlab far more bearable. Special thanks to Pedro Almeida, Claire Earlie, Kit Stokes, Erwin Bergsma, Guiomar Lopez, Ellie Woodward, Ed Steele, Sam Prodger, Marcus Znacchi, Olivier Burvingt, Nieves Garcia Valiente, Mark Wiggins, and Diego Bruciaferri. Outside of university, my friends in Bude provided the perfect distraction when I needed it and were able to remind me that there is more to life than PhD.

My passion for the ocean came from growing up in the paradise that is Bude and mum and dad taking me and my brother to the beach so much. Despite not fully understanding what a PhD is or what my research is about, mum and dad have always given their full support in everything I've done and haven't asked too many questions about when I will get a proper job. When they first dropped me off at university as a fresh undergraduate and the first member of the Inch clan to go to university, I don't think they expected me to still be a student so many years later (and neither did I). But I know that they are proud and at least they can now tell their friends that there is a Dr in the family.

Finally, the greatest acknowledgement of all goes to Francesca for being by my side all the way and for being so patient and selfless, not only during the past 3 years but since we met 8 years ago. People often complain about PhDs being stressful and mentally tough, but I have been able to avoid much of this since it is impossible not to be happy when with Francesca. One day I will repay you for keeping me fed and watered and in clean clothes for so many years.

Chapter 1

Introduction

This chapter introduces the framework of the thesis and outlines the work that is presented in the succeeding chapters. Firstly, the subject and its wider context are introduced, highlighting the knowledge gaps that will be addressed. Following this, the overriding aim and objectives of the research are outlined, and finally a summary of the thesis structure is given.

1.1 Preamble

Over recent decades, the development and exploitation of the coastal zone has increased considerably and it has become one of the most densely populated areas on earth (e.g., Small and Nicholls, 2003); a trend that is expected to continue into the future as coastal population growth exceeds that of the hinterland. The area of coast lying less than 10 m above sea level is home to 10% of the world's population, some 600 million people, despite accounting for only 2% of the world's land mass (McGranahan et al., 2007).

The Intergovernmental Panel on Climate Change (IPCC) project a rise in the global mean sea level of up to 1 m by 2100 (Wong et al., 2014). In addition to sea level rise, climate change is expected to modify the wave climate causing an increase in both storm frequency and intensity (e.g., Knutson et al., 2010). This change in the storm wave climate has arguably a greater impact in terms of coastal erosion and flooding, at least in the short-term and on exposed coasts, whilst in the long-term the impacts are closely linked with sea level rise which will allow storm waves to reach higher elevations.

Several studies provide evidence that the European wave climate is already being influenced by climate change. For example, the analysis of long-term field data sets (e.g.,

Young et al., 2011) and modelled wave data (e.g., Dodet et al., 2010; Bertin et al., 2013) indicates a trend of increasing significant wave height for the Atlantic coast of Europe since the latter half of the 20th century, while Donat et al. (2011) reports an increasing trend in European storminess since 1871. More recently, wave conditions along the Atlantic coast of Europe during the winter of 2013/2014 were the most energetic since at least 1948 (Masselink et al., 2016a). In the southwest of England, significant wave height exceeded the 1% exceedance level of 5.9 m for 22 separate storm events resulting in extensive beach and dune erosion on west-facing beaches (Masselink et al., 2016b).

A common characteristic of natural wave fields is that they are highly irregular and consist of waves with a wide range of frequencies, from tides to wind-driven sea and swell waves. Among these waves, in the frequency range 0.005-0.04 Hz (25-200 s), are infragravity waves, also known as long waves and surf beat. Infragravity waves are forced by wave groups either through weak non-linear interactions offshore (Longuet-Higgins and Stewart, 1962) or at the sea-swell breakpoint from strong non-linearities in sea-swell wave breaking (Symonds et al., 1982). Since the initial observations of Munk (1949) and Tucker (1950), infragravity waves have received considerable attention in the literature and have been the focus of many field, laboratory, and numerical modelling studies.

Unlike sea-swell waves which break and become saturated in the surf zone (Thornton and Guza, 1982), the long wavelengths of infragravity waves impede breaking allowing them to grow towards the shore where they can dominate the water motion on dissipative beaches and reach heights of over 1 m (e.g., Guza and Thornton, 1982; Ruessink et al., 1998; Fiedler et al., 2015; Inch et al., 2017). Therefore, infragravity waves are responsible for conveying storm information from offshore to the inner surf zone and shoreline, thus playing an important role in the erosion of beaches and dunes (e.g., Osborne and Greenwood, 1992a,b; Russell, 1993; Van Thiel de Vries et al., 2008; Roelvink et al., 2009)

(Figure 1.1). As further evidence of this, infragravity wave height close to shore is consistently observed to be positively correlated with the offshore significant wave height in the sea-swell band (e.g., Guza and Thornton, 1982; Elgar et al., 1992; Ruessink, 1998a; Contardo and Symonds, 2013; De Bakker et al., 2014).



Figure 1.1. An infragravity swash event (A) and storm erosion (B) at Summerleaze Beach, Bude (UK), during storm Hercules in January 2014.

There has been a resurgence of interest in infragravity waves throughout the last decade, in part owing to the increased need for understanding in the face of climate change, prompting the first European infragravity wave workshops to be held in France in 2015 and 2016, respectively. Despite numerous field, laboratory, and numerical modelling studies that have emanated from this growing interest, certain infragravity wave processes remain poorly understood. For example, several recent studies have observed considerable infragravity wave dissipation close to shore (e.g., Ruessink, 1998a; Sheremet et al., 2002; Henderson et al., 2006; Guedes et al., 2013; De Bakker et al., 2014), thus contradicting the long-standing viewpoint that infragravity waves reflect almost entirely from the shoreline with shoreward (hereafter *incident*) and seaward (hereafter *reflected*) propagating components combining and giving rise to a quasi-standing wave structure (Guza and Thornton, 1985). However, the primary mechanism responsible for this dissipation is a topic of ongoing debate, whilst the variability in dissipation characteristics with offshore wave forcing and surf zone location has received less

attention. Specifically, the role of offshore wave period in nearshore infragravity wave dynamics has been acknowledged by very few studies (c.f., Senechal et al., 2011; Contardo and Symonds, 2013), with many field studies being undertaken on fetch-limited coasts and/or during low-moderate energy conditions. Furthermore, the vast majority of field studies have focused on sandy beaches and, to a lesser extent, coral reefs. There is an almost complete lack of infragravity field observations from macrotidal, rocky shore platforms. Thus, the impact of bed roughness on infragravity wave transformation processes, particularly dissipation, represents a significant gap in the infragravity wave literature. Shore platforms, which occur around 28% of the coastline of England and Wales, are of particular importance since they directly control the transformation of shoreward propagating waves, and thus the energy arriving at the shoreline. Also, shore platforms are almost always out of equilibrium with the hydrodynamic conditions due to their resistance to short-term morphological changes. These rocky platforms are unlike (sub)tropical coral reef environments which tend to have very sudden change in water depth at the reef crest where short wave breaking is focused preventing large amounts of energy propagating onto the reef flat beyond (e.g., Pomeroy et al., 2012).

To prepare for the increased coastal hazards posed by climate change and ensure the safety of our coastlines, numerical models are used to predict the erosion and recovery of beaches and to highlight areas particularly at risk of coastal flooding. At present, very few models include a realistic representation of the contribution made by infragravity waves to the nearshore hydrodynamics. To address this issue, accurate field observations measured under varying offshore forcing conditions and environmental settings are required.

Despite the need for more field data on infragravity waves, a number of shortcomings remain in the analysis techniques available. This particularly applies to the algorithms for

decomposing an infragravity wave signal into its shoreward and seaward propagating components; a critical procedure when investigating dissipation. One such shortcoming yet to be addressed is the impact of signal noise. This noise, prevalent in field data, can introduce significant error to the results of the reflection analysis (e.g., Huntley et al., 1999) and subsequently to the results of shoreline models if not dealt with appropriately.

1.2 Aim and objectives

The fundamental aim of this project is to improve the quantitative understanding of cross-shore infragravity wave dynamics on sandy beaches and rocky shore platforms. To achieve this, the following more specific objectives are defined:

- Develop and validate a method to accurately estimate incident and reflected infragravity wave components and corresponding reflection coefficients.
 - Perform numerical simulations to test the sensitivity of wave decomposition methods to uncorrelated noise and develop a function to correct for the observed bias that can be applied to field data.
- Identify infragravity wave propagation and dissipation patterns on a sandy beach under contrasting sea and swell wave conditions.
 - Design and execute a field experiment to measure cross-shore infragravity wave dynamics during a variety of environmental conditions.
 - Investigate the temporal variability in infragravity energy in relation to offshore wave conditions, with emphasis on the importance of wave period.

- Explore the spatial distribution of infragravity energy relative to short wave breaking and investigate the possible infragravity dissipation mechanism(s).
- Investigate infragravity wave propagation and transformation across a macrotidal, rocky shore platform.
 - Conduct a field experiment to measure infragravity wave dynamics on a rocky shore platform and adjacent sandy beach simultaneously.
 - Quantify the level of infragravity wave dissipation across the platform and highlight key differences observed between the platform and the beach.

1.3 Thesis structure

Chapter 2 provides a review of the current literature relevant to infragravity waves and the aim and objectives of this thesis, whilst highlighting the processes that are not yet well understood and will form the central focus of Chapters 4-6. The data processing and analysis techniques used to analyse the two major field datasets are very similar and are outlined in Chapter 3, along with the experimental set-up of the two field deployments.

Chapter 4 presents the results of numerical simulations used in the development of a correction function for noise induced error on wave reflection estimates to be applied to the field results.

Results from a high energy, dissipative beach (Perranporth, Cornwall, UK) are presented in Chapter 5, with an emphasis on the spatial (cross-shore) variability in infragravity energy flux with respect to the surf zone location and the temporal variability of infragravity responses to changing offshore wave forcing, investigating potential differences between prevailing sea and swell waves.

Chapter 6 presents the results of a field experiment on a macrotidal, rocky shore platform (Freshwater West, Pembrokeshire, UK). Infragravity wave propagation over the platform is investigated and compared with data from the adjacent sandy beach.

Chapter 7 provides a synthesis of the main findings of the project in the context of the aim and objectives, tying together the main themes that emerge throughout. Original contributions to the field of infragravity waves are identified and recommendations for future research are discussed.

Chapter 2

Literature Review

The aim of this chapter is to provide a summary of key research and relevant infragravity wave literature, highlighting the principal areas and knowledge gaps relevant to the present study. The two main mechanisms for infragravity wave generation are described first, including their transformation from deep into shallow water. Next, recent observations of infragravity wave dissipation in the surf zone are discussed and possible dissipation mechanisms are acknowledged. Finally, the limited literature regarding infragravity wave dynamics on rocky shore platforms is summarised and the paucity of research into infragravity wave propagation on macrotidal shore platforms is recognised.

2.1 Infragravity wave generation

The first field observations of infragravity waves, or ‘surf beat’ as it was then known, were made by Munk (1949) who, upon finding a linear relationship between the amplitude of these low frequency waves and the amplitude of the sea-swell waves, suggested that they were caused by variations in mass transport associated with the short waves. These findings were quickly backed-up by Tucker (1950) who, as well as confirming the linear relationship between the long and short waves amplitudes, performed a cross-correlation between the wave group envelope and the low frequency motion. The most significant result of this correlation analysis was a negative peak at a time lag equal to the travel time of a wave travelling to the shoreline and reflecting back to the measurement location as predicted by linear wave theory. Although Tucker (1950) was unable to explain the significance of this time lag, it was concluded that low frequency waves are forced by the mass transport of short wave groups and are released when the short waves break, thus allowing them to reflect from the shoreline.

There are generally two accepted theories for the generation of infragravity waves, both related to the variation in sea-swell energy induced by wave groups. Wave dispersion, which implies that wave celerity in deep water increases with decreasing frequency (i.e., with increasing wave period), causes wave trains to become more regular and narrow-banded as they propagate away from a storm system. When two sets of sea-swell waves with slightly different frequencies and wavelengths interact, a group structure is created through the addition of in phase wave amplitudes and the cancellation of out of phase wave amplitudes. This is demonstrated in Figure 2.1 using two sets of sea-swell waves with neighbouring frequencies (a so-called bichromatic wave field).

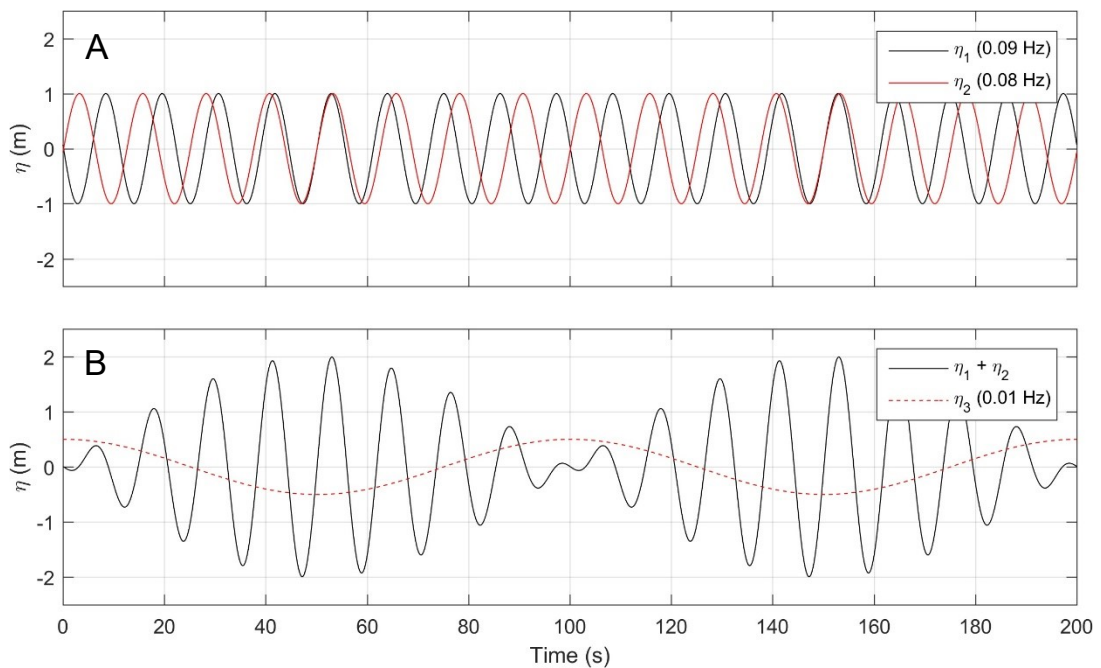


Figure 2.1. Two sinusoidal wave trains of slightly different frequencies ($\eta_1 = 0.09$ Hz and $\eta_2 = 0.08$ Hz) but the same amplitude (A), and the resulting wave groups and bound infragravity wave at the difference frequency ($\eta_3 = 0.01$ Hz) (B).

2.1.1 Bound wave theory

The first theory for infragravity wave generation was proposed by Biesel (1952), and later by Longuet-Higgins and Stewart (1962, 1964) and Hasselmann (1962), who demonstrated theoretically that the modulation of short wave height by wave groups

induces a variation in water level causing it to become depressed under groups of large waves where the mass transport is negative, and enhanced where the sea-swell waves are smaller. This variation in water level creates a second-order wave that is ‘bound’ to the wave groups (Figure 2.1). Longuet-Higgins and Stewart (1962, 1964) demonstrated this concept theoretically using the concept of radiation stress which is defined as the excess flux of momentum due to the presence of waves. For a frame of reference in which wave fronts are normal to the x -axis, the flux of x directed momentum in the x direction S_{xx} is defined as

$$S_{xx} = \overline{\int_{-h_0}^{\eta} (\rho u_x) u_x dz} + \overline{\int_{-h_0}^{\eta} P_{wave} dz} \quad (2.1)$$

where η is the time-varying water surface elevation due to waves, h is water depth, ρ is fluid density, u_x is particle velocity, and P_{wave} is the wave-induced pressure. With linear wave theory, Equation 2.1 reduces to

$$S_{xx} = \left(2n - \frac{1}{2}\right) E \quad (2.2)$$

where

$$n = \frac{1}{2} \left(1 + \frac{2kh}{\sin 2kh}\right) \quad (2.3)$$

where k is the frequency-dependent wave number ($2\pi/L$, where L is wavelength) and

$$E = \frac{1}{8} \rho g H^2 \quad (2.4)$$

where g is gravitational acceleration (9.81 m s^{-2}) and H is wave height.

Gradients in radiation stress direct force from areas of greater stress (high waves) to areas of less stress (low waves) which in turn creates a wave like disturbance in the mean sea

level beneath the wave groups. This fluctuation in mean sea level, hereafter referred to as a bound infragravity wave, propagates at the group velocity C_g and has the same wavelength and period as the wave groups, but is 180° out of phase (i.e., the trough of the bound infragravity wave is coincident with the largest waves in the wave group). The surface elevation of a bound infragravity wave accompanying a wave group can be expressed in terms of the radiation stress as

$$\eta(t) = -\frac{S_{xx}(t)}{\rho(gh - c_g^2)} + \text{constant} \quad (2.5)$$

where t is time and c_g is the wave group velocity. The work of Longuet-Higgins and Stewart (1962, 1964) is consistent with the negative correlation observed by Tucker (1950) and is now a widely accepted theory following its validation by a number of field (e.g., Huntley and Kim, 1984; Herbers et al., 1994) and laboratory (e.g., Baldock et al., 2000) studies.

2.1.1.1 Bound wave shoaling

The shoaling of sea-swell waves propagating into shallower water can be described using Green's law, based on linear wave theory and assuming the conservation of energy flux, which predicts a wave amplitude proportional to $h^{-1/4}$. Longuet-Higgins and Stewart (1962) present a shallow water equilibrium solution for the shoaling of bound infragravity waves which can be derived from Equation 2.5, which becomes near-resonant in shallow water where $C_g \approx \sqrt{gh}$. Still assuming the conservation of short wave energy flux, this yields $S_{xx} \sim h^{-1/2}$ such that the amplitude of the bound infragravity wave is proportional to $h^{-5/2}$. Although this is often interpreted as a shoaling law for bound infragravity waves propagating over a sloping bed and has been used to assess the presence of such waves (e.g., Elgar et al., 1992; Ruessink, 1998b), Longuet-Higgins and Stewart (1962) did

express concerns over the validity of this equilibrium solution since Equation 2.5 is based on bound waves of constant form propagating over a horizontal bed and because resonance needs time to build up. Several field (e.g., Elgar et al., 1992; Ruessink, 1998b), laboratory (e.g., Baldock et al., 2000; Battjes et al., 2004; Van Dongeren et al., 2007; Dong et al., 2009) and numerical (e.g., Madsen et al., 1997) studies have reported shoaling rates of bound infragravity waves varying between $h^{-1/4}$ and $h^{-5/2}$.

To achieve an amplitude growth rate stronger than that of conservative shoaling (Green's law), energy must be transferred from sea-swell waves within the group to the bound infragravity wave. For this to occur, the bound infragravity waves must lag behind the wave groups allowing for a phase shift away from the equilibrium value of 180° . This lag has been reported by field (e.g., Masselink, 1995) and laboratory (e.g., Battjes et al., 2004) studies, and analytically by Janssen et al. (2003) who showed that shoaling bound waves propagate slightly slower than wave groups thus causing a phase lag that increases into shallower water. A detailed study of high-resolution laboratory data by Battjes et al. (2004) observed an increase in phase lag with increasing infragravity frequency, which in turn creates a frequency-dependent shoaling rate with lower frequency bound waves shoaling close to Green's law and higher frequency waves shoaling close to the shallow water equilibrium solution of Longuet-Higgins and Stewart (1962). These results are demonstrated in Figure 2.2 showing that bound waves in the frequency range 0.04-0.06 Hz shoal close to $h^{-5/2}$, whilst shoaling in the frequency range 0.16-0.18 Hz is of the order of Green's law, and waves with frequencies 0.10-0.12 Hz shoal at a rate between these values. These frequency ranges are much higher than infragravity frequencies in the field due to the frequency of the primary waves in the laboratory experiments of Battjes et al. (2004), in which they are referred to as subharmonic gravity waves, though the generation mechanism is the same.

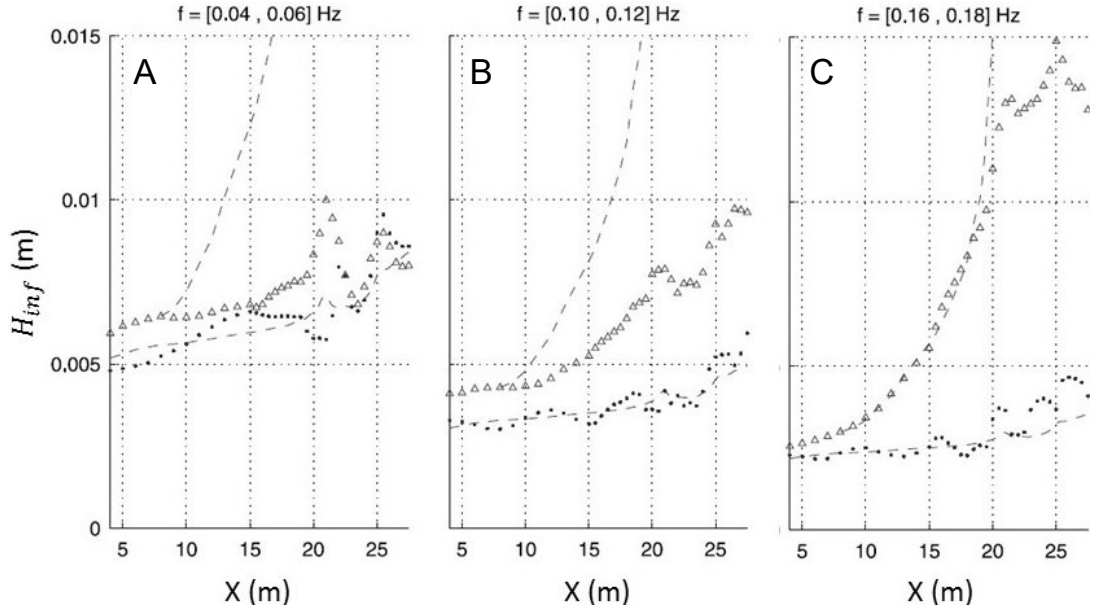


Figure 2.2. Incident (triangles) and reflected (dots) significant wave height H_s for frequency bands 0.04-0.06 Hz (A), 0.10-0.12 Hz (B), and 0.16-0.18 Hz (C), versus cross-shore location. Lower dashed curve in each plot is Green's law ($H \sim h^{-1/4}$) fitted to reflected wave heights in the zone offshore from $x = 20$ m, and upper dashed curves are the Longuet-Higgins and Stewart (1962) asymptote ($H \sim h^{-5/2}$) initiated with the wave height at $x = 8$ m. Note that the frequency bands are higher than conventional infragravity frequencies due to the high frequency of the primary waves used in the laboratory experiments. Source: Battjes et al. (2004).

Battjes et al. (2004) found that the frequency-dependent shoaling of bound infragravity waves could be generalized by relating it to a normalised bed slope parameter β_b defined as

$$\beta_b = \frac{\beta T}{2\pi} \sqrt{\frac{g}{h}} \quad (2.6)$$

where β is bed slope and T is the wave period of the incident infragravity wave. They found that for values of $\beta_b < 0.06$, bound waves experience a mild sloping regime and undergo a large amplitude growth in the shoaling zone, whereas the amplitude growth is weak for values of $\beta_b > 0.3$ due to waves experiencing a steep sloping regime. Infragravity wave dissipation was also found to be controlled by β_b ; this was verified and extended by Van Dongeren et al. (2007) and will be discussed further in Section 2.3.4.

2.1.1.2 Bound wave release

The grouped structure of sea-swell waves is destroyed in the surf zone where these waves are broken and their amplitudes become depth-limited. It has been widely accepted in the literature that bound infragravity waves are released in the surf zone and propagate shoreward as free waves since the mechanism forcing these waves is lost with the destruction of the wave groups. Numerous studies have demonstrated the release of bound waves through cross-correlation between the wave group envelope and infragravity motion (e.g., Masselink, 1995; Ruessink, 1998a; Janssen et al., 2003), bispectral analysis (e.g., Herbers et al., 1995; Ruessink, 1998b), and the reduction in infragravity wave shoaling at the short wave breakpoint (e.g., Battjes et al., 2004).

The results of Ruessink (1998a) shown in Figure 2.3 demonstrate the use of cross-correlation to investigate the release of bound infragravity waves. Here, the cross-correlation coefficient between the infragravity motion and the wave group envelope is lowest (typically -0.5 to -0.7) at the onset of short wave breaking (Figure 2.3A), indicating that the infragravity waves are predominantly bound (i.e., out of phase). Whereas the increasing intensity of short wave breaking causes the cross-correlation coefficient to move towards mostly non-significant values. Figure 2.3B shows that during high energy conditions the cross-correlation coefficient between the infragravity motion and the wave group envelope is significantly negative at the most seaward measurement location but non-significant, suggesting free infragravity waves, at all other locations. However, under moderate energy conditions with a smaller surf zone width, the cross-correlation coefficient remains at a value significantly less than 0 at all locations, although tending towards 0 close to shore where presumably the bound waves had begun to be released. Infragravity energy levels were extremely small during low energy conditions

and dominated by free wave motion, hence the cross-correlation coefficient was never significantly different from 0.

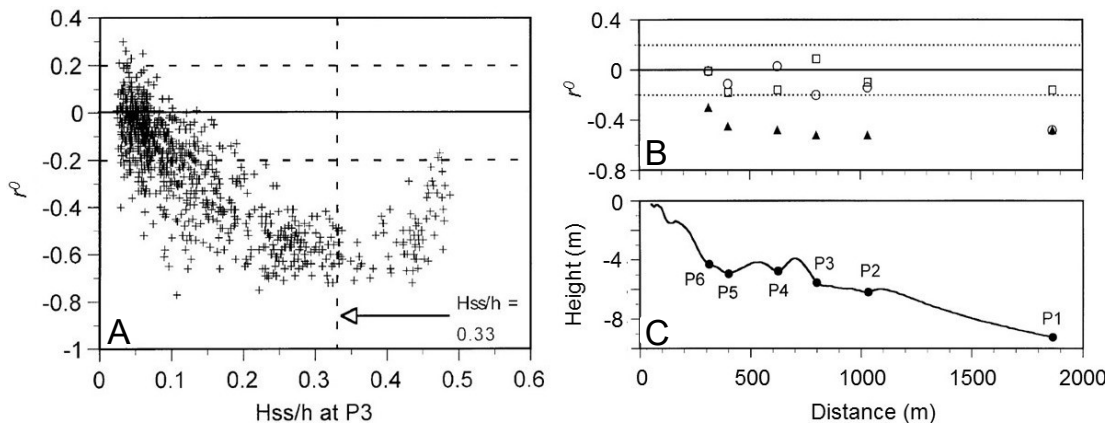


Figure 2.3. Cross-correlation coefficient at zero time lag r^0 between the wave group envelope and infragravity motion as a function of the local relative wave height H_{ss}/h (A). Cross-shore change in r^0 between the wave group envelope and infragravity motion for low (open squares), moderate (solid triangles), and high (open circles) energy conditions (B). Cross-shore profile of the study site showing measurement locations (C). Horizontal dashed lines in (A) and (B) are the 95% confidence levels on $r^0 = 0$. Vertical dashed line in (A) indicates the onset of short wave breaking at $H_{ss}/h = 0.33$. Source: Ruessink (1998a).

However, Baldock (2012) argues, based on an interpretation of Longuet-Higgins and Stewart (1962), that the release of bound infragravity waves is not necessarily controlled by short wave breaking but rather that bound waves will be progressively released when the short waves are in shallow water and the bound wave satisfies the free wave dispersion relationship, which can occur shoreward or seaward of the short wave breakpoint. Baldock (2012) points out that short waves are likely to be in shallow water at the breakpoint under mild wave and laboratory conditions, whereas the largest waves during storms are more likely to break before true shallow water conditions are met. These claims are supported by the field measurements of Contardo and Symonds (2013) who observed continued forcing of bound infragravity waves shoreward of the short wave breakpoint during more energetic conditions on a barred beach in Western Australia.

2.1.2 Time-varying breakpoint theory

Assuming that sea-swell wave height in the surf zone is solely a function of the local water depth, a shoreward propagating wave train consisting of clearly spaced wave groups gives rise to a time-varying short wave breakpoint that moves seaward (shoreward) during the breaking of high (low) waves. This time-varying breakpoint concept is the basis of a second infragravity wave generation mechanism, proposed by Symonds et al. (1982), in which freely propagating infragravity waves are generated as dynamic set-up/down oscillations with the same frequency as the wave groups. These breakpoint generated infragravity waves are forced by time-varying gradients in radiation stress and radiate away from the breakpoint in both the shoreward and seaward direction. Shoreward propagating infragravity waves can reflect from the shoreline meaning that seaward propagating waves offshore of the breakpoint can consist of both initially incident waves that have been reflected at the shoreline and seaward radiating waves generated at the breakpoint. Therefore, the amplitude of the seaward propagating waves offshore of the surf zone depends on the relative phase of the two wave trains as constructive or destructive superposition can occur (Symonds et al., 1982; Schaffer, 1993; Baldock et al., 2000).

2.1.3 Relative importance of bound and breakpoint forced infragravity waves

Infragravity waves may be generated by bound wave theory and the time-varying breakpoint simultaneously; however, determining the relative importance of the two mechanisms under varying environmental conditions can be problematic and is a topic that remains largely unanswered in the literature. This particularly applies to field studies since an extensive array of instruments, both inside and outside the surf zone, is ideally required. List (1992) and Van Dongeren et al. (2002) suggested that, as bed slope decreases, bound infragravity waves become increasingly important relative to those

forced at the breakpoint. This was explored further by Battjes et al. (2004) who explain that the normalised bed slope parameter, as defined in Equation 2.6, can be used to identify the dominant generation mechanism. They show that breakpoint generated infragravity waves are expected to dominate when there is a steep sloping regime and the shoaling of bound waves is very weak. Bound infragravity waves are expected to dominate almost entirely in mild sloping regimes where the increased surf zone width causes breakpoint generated waves to be ineffective because of phase cancellation (see also Baldock and Huntley, 2002). In addition to the normalised bed slope, Baldock and Huntley (2002) and Baldock (2012) showed that short wave steepness also plays an important role in infragravity wave generation and Baldock (2012) combined these parameters to develop a surf beat similarity parameter $\xi_{surfbeat}$ to indicate the type of infragravity wave likely to dominate in different conditions, defined as

$$\xi_{surfbeat} = \beta_b \sqrt{\frac{H_o}{L_o}} \quad (2.7)$$

where H_o is the offshore significant wave height and L_o is the deep water wavelength corresponding to the offshore peak frequency. Infragravity energy in the surf zone is expected to be primarily breakpoint generated when $\xi_{surfbeat}$ is high, and from the release of bound waves when $\xi_{surfbeat}$ is low. This parameter was found to agree well with the findings of Contardo and Symonds (2013).

In general, past field studies have shown profound evidence of infragravity waves being generated by bound wave theory with very few showing convincing evidence of infragravity waves being generated at the breakpoint (c.f., Pomeroy et al., 2012; Contardo and Symonds, 2013; Becker et al., 2016). This is likely due to the mild beach slopes in most published field studies, as demonstrated by Van Dongeren et al. (2007) in showing that several of the field sites that have hosted important infragravity wave research,

including Monterey and Duck in the USA, and Terschelling in the Netherlands, have typical values of β_b that place them well within the mild sloping regime.

Some laboratory studies have shown the dominance of breakpoint generated infragravity waves, however, these have normally been performed on steep laboratory slopes conducive to the time-varying breakpoint mechanism. For example, laboratory studies by Baldock et al. (2000) and Baldock and Huntley (2002) with bichromatic and random wave conditions, respectively, showed a clear dominance of breakpoint forced infragravity waves on a steep beach with a slope of 1:10. In contrast, the study by Janssen et al. (2003) on a slope of 1:70 gave no indication of breakpoint generated infragravity waves.

The most common technique used to identify the dominant source of free infragravity waves in the surf zone is cross-correlation between the wave group envelope outside the surf zone and the infragravity motion through the surf zone (e.g., List, 1992; Masselink, 1995; Janssen et al., 2003; Pomeroy et al., 2012; Ruju et al., 2012). If free infragravity waves in the surf zone are released bound waves, cross-correlation with the wave group envelope at a location outside the surf zone, where the infragravity wave remains bound, should reveal a negative peak at a time lag equal to the travel time for the infragravity wave to propagate between the two measurement locations. However, since breakpoint forced infragravity waves are generated in phase with the wave groups, the correlation described above would be positive if this was the dominant generation mechanism. In instances where both bound and breakpoint forced infragravity waves exist, opposing phases may cancel out thus providing no significant correlation at the expected time lag (e.g., Schaffer, 1993). Figure 2.4 uses the results of Janssen et al. (2003) to demonstrate the use of cross-correlation analysis to detect the source of infragravity motion. Figure 2.4A shows cross-correlation results between the wave group envelope and the infragravity motion at each location; it can be seen that the correlation at zero time lag is

strongly negative until the short wave breakpoint at $x \approx 23$ m where it becomes incoherent before tending to zero as the wave groups break up. Figure 2.4B presents the cross-correlation results between the wave group envelope at $x = 0$ m and the infragravity motion at all other locations. A band of negative correlation at a time lag equal to that of a wave propagating shoreward from $x = 0$ m can be seen and this remains strongly negative shoreward of the breakpoint at $x \approx 23$ m, thus implying that infragravity waves in the surf zone are predominantly released bound waves rather than breakpoint forced. A band of negative correlation representing the reflected infragravity wave can also be observed at a time lag that is in good agreement with the shallow water wave speed.

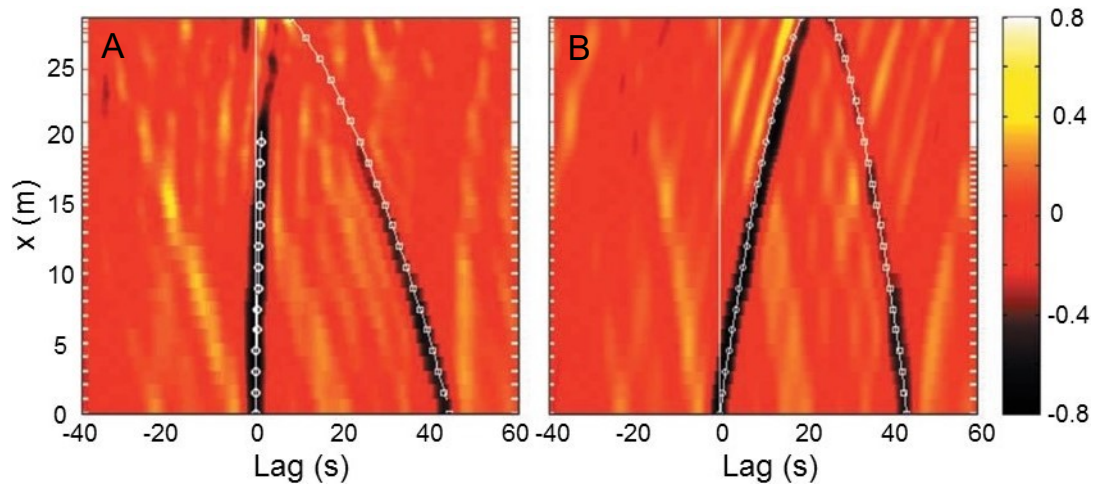


Figure 2.4. Cross-correlation between the wave group envelope and infragravity motion at the same locations (A) and between the wave group envelope at $x = 0$ m and infragravity motion at all locations (B). Lines with circular markers indicate the time lag for incident waves propagating at the wave group celerity C_g , and lines with square markers indicate the time lag for reflected waves reflected at $x = 30$ m propagating at the shallow water wave speed \sqrt{gh} . Source: Janssen et al., 2003.

Moura and Baldock (2017) employed a novel, remote sensing method to identify the dominant infragravity generation mechanism whereby the cross-correlation is performed between the breakpoint oscillations and the shoreline motion, both measured remotely via video. Thirteen datasets from three different beaches were analysed and the results, contradictory to some earlier studies (e.g., Battjes et al., 2004), showed that bound wave

theory dominated on beaches with a narrow surf zone and plunging breakers, whereas the time-varying breakpoint theory was dominant where steep, spilling waves break in deeper water creating a wider surf zone.

2.1.4 Infragravity frequency range

The specific frequency range chosen to define the infragravity band varies in the literature, with a common lower limit of 0.005 Hz and an upper limit typically between 0.04 and 0.05 Hz. The value used for the upper limit depends primarily on location, with a limit of 0.04 Hz deemed most suitable on exposed coasts (e.g., Elgar et al., 1992; Fiedler et al., 2015) where peak sea-swell frequencies can equal or exceed 0.05 Hz. On low fetch coastlines where wind waves are more prevalent, an upper infragravity limit of 0.05 Hz is more suitable (e.g., Ruessink et al., 1998; De Bakker et al., 2014). Infragravity frequencies in laboratory experiments depend on the frequency of the generated short waves and therefore often differ from conventional infragravity frequencies in field studies (e.g., Van Dongeren et al., 2007).

2.1.5 Other low frequency waves

As well as bound, free, and reflected (leaky) infragravity waves, two other types of low frequency wave exist. Firstly, edge waves (e.g., Huntley et al., 1981) are alongshore propagating infragravity waves that are reflectively trapped at the shoreline due to refraction. Secondly, shear waves (e.g., Oltman-Shay et al., 1989), sometimes referred to as far infragravity waves, occur as fluctuations in the alongshore current rather than as a surface elevation displacement and exist at the low frequency end of the infragravity band (<0.01 Hz). Since the focus of this thesis is on cross-shore infragravity waves and the data presented herein is from cross-shore dominated field sites, edge and shear waves will not be discussed further in this literature review.

2.2 Parameterizing nearshore infragravity wave height

Regardless of their generation mechanism, shoreward propagating free infragravity waves in the surf zone typically continue to shoal according to Green's law and can dominate the water motion close to shore where heights of >1 m have been recorded (e.g., Guza and Thornton, 1982; Ruessink et al., 1998; Fiedler et al., 2015). Infragravity wave height in the nearshore, or at the shoreline as runup, has frequently been shown to be positively correlated with offshore wave height (Holman, 1981; Guza and Thornton, 1982; Guza and Thornton, 1985; Holman and Sallenger, 1985; Oltman-shay et al., 1989; Elgar et al., 1992; Okihiro et al., 1992; Ruessink, 1998a; Ruggiero et al., 2004; Senechal et al., 2011; De Bakker et al., 2014). However, the relationship between infragravity waves and offshore wave period has received far less attention. Elgar et al. (1992) and Ruessink (1998a), among others, reported a stronger correlation between nearshore infragravity energy and offshore energy in the swell frequency band (0.04-0.14 Hz) than the sea frequency band (0.14-0.33 Hz). For example, using field data from Terschelling in the Netherlands with significant wave heights up to 4.5 m (mean = 1.2m), correlation coefficients calculated by Ruessink (1998a) were 0.90-0.96 for infragravity energy correlated with swell energy, but only 0.66-0.72 when correlated with energy in the sea frequency band (Figure 2.5A-C). These findings are consistent with bound wave theory since swell dominated conditions tend to produce narrower spectrums and it was demonstrated theoretically by Longuet-Higgins and Stewart (1962, 1964) and Hasselmann (1962) that the non-linear interaction between a pair of sea-swell waves is stronger when the frequencies of the two interacting waves are close together. This has since been corroborated by a number of field, laboratory, and numerical modelling studies (e.g., Elgar and Guza, 1985; Norheim et al., 1998; De Bakker et al., 2015).

Stockdon et al. (2006) used a vast dataset from a range of beaches and environmental conditions to show that the variability in infragravity runup is best explained using a parameter that accounts for both offshore wave height and wave period and observe a strong relationship with $(H_o L_o)^{1/2}$. This was supported by Senechal et al. (2011) who found that infragravity wave runup during extreme storm conditions has considerably less scatter when correlated with $(H_o L_o)^{1/2}$ ($r^2 = 0.83$; Figure 2.5D) than with H_o only ($r^2 = 0.71$). More recently, Fiedler et al. (2015) found a strong relationship between infragravity runup and $(H_o L_o)^{1/2}$ in very energetic conditions with significant wave heights exceeding 7 m. Contardo and Symonds (2013) reported a 30% stronger infragravity wave height response to long period incident swell ($T_p > 10$ s) than to short period wind-sea ($T_p < 5$ s), though conditions were fairly low energy and did not exceed 1.2 m. Despite these studies, a detailed investigation into the importance of wave period for infragravity wave dynamics, particularly their cross-shore behaviour in the surf zone, is currently lacking.

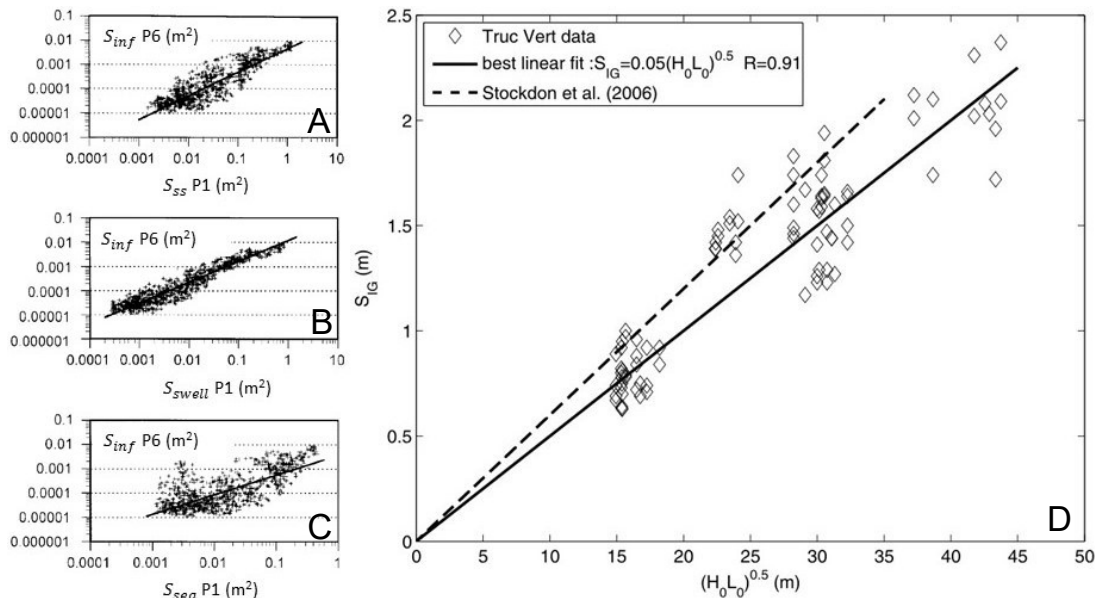


Figure 2.5. Infragravity energy S_{inf} as a function of total offshore sea-swell energy S_{SS} 0.04-0.33 Hz (A), offshore swell energy S_{swell} 0.04-0.14 Hz (B), and offshore sea energy S_{sea} 0.14-0.33 Hz (C). Straight lines are least squares fits. Infragravity runup elevation S_{IG} parameterized by the offshore forcing parameter $(H_o L_o)^{0.5}$ (D). Lines are

best linear fits. Dashed line in (D) is the best linear fit from Stockdon et al. (2006). Source: Ruessink (1998a) (A-C) and Senechal et al. (2011) (D).

2.3 Dissipation and reflection

It was long believed that infragravity waves, due to their long wavelengths that impede breaking, reflect almost entirely from shore giving rise to a cross-shore (quasi-)standing wave structure (Guza and Thornton, 1985). However, more recently, particularly over the past 10-15 years, considerable infragravity wave dissipation in the nearshore has been observed by a number of field (e.g., Ruessink, 1998a; Sheremet et al., 2002; Henderson et al., 2006; Guedes et al., 2013; De Bakker et al., 2014; Fiedler et al., 2015), laboratory (e.g., Battjes et al., 2004; Van Dongeren et al., 2007; De Bakker et al., 2015), and numerical modelling (e.g., Ruju et al., 2012; De Bakker et al., 2016a) studies. Furthermore, infragravity dissipation is not constant throughout the infragravity band but highly frequency-dependent, with high frequency waves dissipating more than those of a lower frequency. Some of the earliest evidence of infragravity wave dissipation was observed by Guza and Thornton (1985) who analysed pressure and velocity data from a beach in Southern California and found infragravity waves with frequencies <0.03 Hz to be standing, but waves with higher frequencies showed a more progressive wave pattern. Ruessink (1998a) found that the cross-shore amplification of bulk infragravity energy on a very dissipative (1:200) beach in the Netherlands decreased significantly to values less than 1 in the surf zone, indicating an onshore decline in infragravity energy. In the laboratory study by Battjes et al. (2004), data from random wave experiments were separated into incident and reflected components and it was found that a significant amount of infragravity dissipation takes place in a narrow zone very close to shore, totalling around 90% of the energy at high infragravity frequencies and 60% of the total infragravity energy. A field investigation of infragravity wave dissipation at the shoreline was carried out by De Bakker et al. (2014) who calculated an average bulk infragravity

reflection coefficient of 0.23 in a water depth of around 0.65 m on a dissipative beach (1:80) in the Netherlands. Also, a transition was observed at a frequency of 0.0167 Hz, below which infragravity waves were cross-shore standing but above which the waves were predominantly onshore progressive. A similar trend was observed on a steeper beach (1:30) but with a transition between standing and progressive infragravity waves at a higher frequency of 0.0245 Hz, thus indicating less infragravity dissipation (higher reflection) as a result of the steeper bed slope.

As additional evidence of infragravity wave dissipation, some field investigations on dissipative beaches have reported infragravity runup to become saturated (i.e., ceases to increase despite further increases in offshore forcing) in a similar way to sea-swell runup, mainly during high energy conditions (Ruessink et al., 1998; Ruggiero et al., 2004; Senechal et al., 2011; Guedes et al., 2013). For example, Senechal et al. (2011) observed runup saturation extending to almost the entire infragravity band during extreme storm conditions ($H_o = 6.4$ m, $T_p = 16.4$ s) at Truc Vert beach in France. This motivated a hyperbolic tangent fit which predicted 80% of runup variability using H_o as the independent variable; a linear fit predicted 71% of the variability. Interestingly, Fiedler et al. (2015) did not observe saturation of infragravity runup at the 1:80 Agate beach in Oregon, USA, despite the offshore significant wave height exceeding 7 m. However, infragravity amplification, defined as the ratio of infragravity wave height at the shoreline and at a location approximately 1 km offshore, decreased dramatically during the most energetic conditions, indicating potential proto-saturation of infragravity runup (i.e., saturation could occur with further increases in offshore forcing).

Whilst video-based runup measurements provide useful information about the magnitude and potential saturation of infragravity energy reaching the shoreline, wave measurements taken in the nearshore are required to gain an insight into the infragravity

dissipation mechanism. Infragravity dissipation, and particularly frequency dependent dissipation, means that the infragravity wave characteristics in the nearshore may not be coherent with those observed at the shoreline. For example, Guedes et al. (2013) calculated the coherence between runup time series and nearshore wave time series measured in up to 2.6 m water depth on a dissipative beach and observed the highest coherence values at low infragravity frequencies (<0.02 Hz), consistent with the peak runup frequency, but lower levels of coherence at higher infragravity frequencies that underwent significant dissipation between the two measurement locations. As such, infragravity runup is influenced by, among other factors, the frequency distribution of shoreward propagating infragravity energy and this, among other factors such as swash zone slope and sediment characteristics, should be considered when relating runup and nearshore wave data.

2.3.1 Bed friction

Several studies have attempted to identify the mechanism(s) responsible for the observed decay of infragravity wave energy in the nearshore, and this continues to be a topic of ongoing debate in the literature. Henderson and Bowen (2002) suggested bed friction was the dominant infragravity wave dissipation mechanism in the surf zone during an experiment at Duck, North Carolina, USA. However, a follow-up study by Henderson et al. (2006) concluded that the drag coefficient used in Henderson and Bowen's (2002) bed friction formulation was unrealistically high for sandy beaches and that bed friction was not the dominant dissipation mechanism. Several studies since have supported this assertion and added to the growing consensus that bed friction is, at best, a secondary infragravity wave dissipation mechanism on sandy beaches (Thomson et al., 2006; Van Dongeren et al., 2007; Lin and Hwung, 2012; De Bakker et al., 2014, 2016). In contrast, bed friction has been shown to play an important role in the dissipation of infragravity

waves in coral reef environments with extensive shallow regions where drag coefficients are typically an order of magnitude larger than sandy beaches (Pomeroy et al., 2012; Van Dongeren et al., 2013).

2.3.2 Non-linear energy transfer

As an alternative to bed friction, Henderson et al. (2006) and Thomson et al. (2006) used bispectral analysis to show that infragravity energy loss can be explained by the non-linear transfer of energy back to sea-swell frequencies through triad interactions. Though not strictly a dissipation mechanism since energy is transferred rather than removed from the wave spectrum, these studies on relatively mild-steep sloping (1:50-1:15) natural beaches in low-moderate energy conditions demonstrated that these non-linear interactions can be strong in the surf zone where sea-swell energy remains dominant over infragravity energy ($h > 1$ m). Guedes et al. (2013) also observed a reduction in infragravity energy through non-linear transfers to sea-swell frequencies but on a more dissipative (1:70) beach where infragravity energy was relatively stronger. They concluded, however, that non-linear energy transfers alone were not enough to explain the large infragravity energy loss that was observed. Baldock (2012) explains that the interaction between free infragravity waves and sea-swell waves is very weak, suggesting that infragravity waves are likely to still be bound if losing significant energy through non-linear transfers.

2.3.3 Infragravity wave breaking

The final dissipation mechanism that is gathering increasing support in the literature as the dominant mechanism close to shore on dissipative beaches is infragravity wave breaking (Battjes et al., 2004; Van Dongeren et al., 2007; Lin and Hwung, 2012; De Bakker et al., 2014,2015; Rijnsdorp et al., 2015). Using bichromatic wave experiments in

a laboratory, Van Dongeren et al. (2007) showed that as depth decreases and infragravity energy becomes increasingly important relative to sea-swell energy, non-linear energy transfers are predominantly between infragravity frequencies and their higher harmonics. These self-self interactions and enhancement of infragravity harmonics cause the infragravity wave to steepen and become more asymmetrical, analogous to the shoaling of sea-swell waves, before eventually breaking and turning into a turbulent bore. To validate these findings, Van Dongeren et al. (2007) ran an additional experiment with monochromatic, free infragravity waves. The initially sinusoidal waves developed higher harmonics, steepened up and transitioned into turbulent bores, dissipating most of their energy and reflecting very little, thus corroborating the results from the bichromatic wave experiments. Such an analysis cannot be replicated in the field given the constant presence of sea-swell waves and hydrodynamic noise, particularly in broad-banded wind-sea. However, similar evidence in support of infragravity wave breaking was observed in a laboratory experiment with irregular wave conditions based on a JONSWAP spectrum (De Bakker et al., 2015), and in idealised numerical modelling studies using the non-hydrostatic SWASH model (De Bakker et al., 2014,2015; Rijnsdorp et al., 2015). Moreover, infragravity waves possessing an asymmetric, bore-like shape have been observed in coral reef modelling studies by Nakaza (1991) and Shimozono et al. (2015).

Numerical modelling by Ruju et al. (2012) on 1:20-1:30 sloping beaches showed that both non-linear energy transfers to sea-swell frequencies and infragravity wave breaking could play a role in infragravity energy loss in different parts of the surf zone. In the outer surf zone, where sea-swell energy remains strong relative to infragravity energy, triad interactions transferred energy from infragravity frequencies back to sea-swell frequencies. Whereas closer to shore, with the decrease in sea-swell energy, these interactions turned into self-self infragravity interactions culminating in their breaking.

2.3.4 Normalised bed slope parameter

In an attempt to generalise infragravity wave reflection and potential breaking at the shoreline, Van Dongeren et al. (2007) proposed a normalised bed slope parameter β_H , identical in form to Battjes et al.'s (2004) β_b parameter defined in Equation 2.6 but with h replaced by the incident infragravity wave height H^+ with period T giving

$$\beta_H = \frac{\beta T}{2\pi} \sqrt{\frac{g}{H^+}} \quad (2.8)$$

As with the earlier defined β_b parameter, β_H is based on the premise that a given bed slope will have a higher effective steepness for low frequency (long) waves than it will for high frequency (short) waves. It should be noted that β_H is directly related to the Iribarren number ξ as $\xi = \sqrt{2\pi}\beta_H$ where

$$\xi = \frac{\beta}{\sqrt{H_o/L_o}} \quad (2.9)$$

providing that H_o is replaced by H^+ and L_o is estimated for the infragravity frequency corresponding to T in Equation 2.8 (rather than the peak offshore wave period). Thereby, β_H can be viewed as an infragravity equivalent of the conventional Iribarren number. For sea-swell waves, Battjes (1974) observed a relationship between the amplitude reflection coefficient R at the shoreline and the Iribarren number, which can also be written in terms of β_H as

$$R = 0.1\xi^2 = 0.2\pi\beta_H^2 \quad (2.10)$$

Van Dongeren et al. (2007) found that this relationship also applies quite well to the infragravity amplitude (not squared) reflection coefficient (Figure 2.6A). A transition occurs at $\beta_H \approx 1.25$, similar to the value found for the onset of breaking sea-swell waves (Battjes, 1974), below which infragravity waves experience a mild sloping regime and

dissipate due to breaking, and above which waves experience a steep sloping regime where $R \approx 1$ and minimal dissipation occurs. Using field data from two beaches with contrasting beach slopes, De Bakker et al. (2014) observed a more gradual transition from mild to steep sloping regimes occurring at $\beta_H \approx 3$ (Figure 2.6B-C), whereas numerical modelling by De Bakker et al. (2016a) showed this transition occurring at $\beta_H \approx 4$. Positive relationships between β_H and the bulk infragravity energy (squared) reflection coefficient were observed in the field by Guedes et al. (2013) and in a numerical modelling study by Rijnsdorp et al. (2015).

The effect of bed slope on infragravity wave dissipation and reflection can be tidally modulated on natural beaches as their profiles are often complex rather than linear. Indeed, significant changes in beach gradient, and thus β_H , can occur within one surf zone width during storm conditions (e.g., Senechal et al., 2011). Thomson et al. (2006) investigated the effect of beach shape on infragravity wave dissipation on a beach where the profile is convex at low tide and concave at high tide. Although the total surf zone width was not tidally modulated, infragravity dissipation was enhanced over the convex, low tide profile. This was thought to be due to the larger spatial extent of the shallow water (<1 m) region where non-linear energy transfers are closer to resonance.

Despite the numerous studies referenced to above, the dominant mechanism responsible for the dissipation of infragravity waves remains poorly understood. Over recent years, some consensus has been reached suggesting that infragravity wave breaking occurs close to shore on dissipative beaches; however, much of this evidence has been based on laboratory and/or numerical modelling. Evidence from the detailed analysis of field data, especially during energetic swell conditions which have been shown to generate higher levels of infragravity energy, remain sparse.

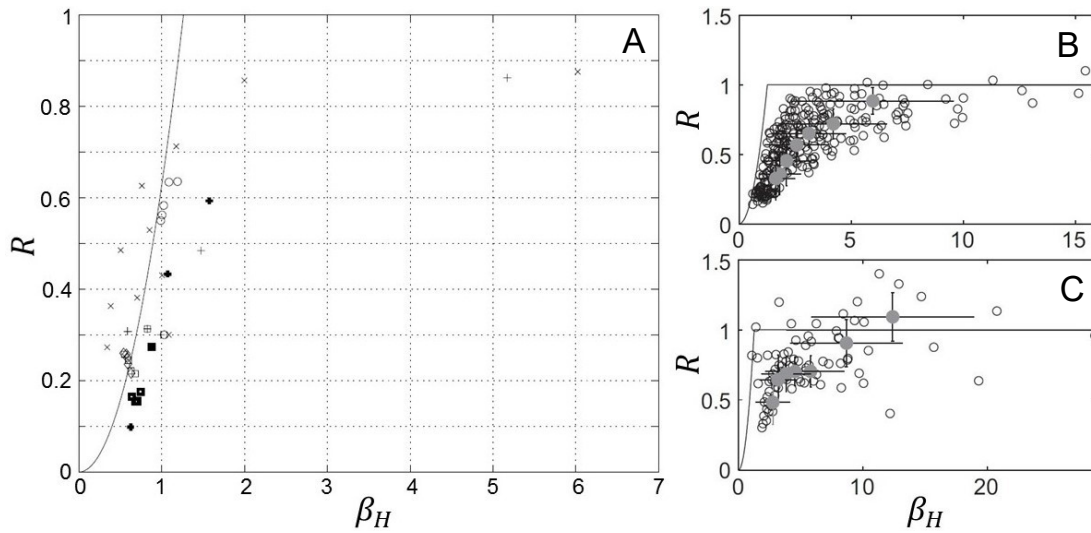


Figure 2.6. Shoreline amplitude reflection coefficient R for various infragravity frequencies as a function of the normalised bed slope parameter β_H on a laboratory beach (A), and gentle (B) and steep (C) sloping natural beaches. The solid line in all plots is $\min(1, R = 2\pi\beta_H^2)$. Source: Van Dongeren et al. (2007) (A) and De Bakker et al. (2014) (B-C).

2.3.5 Wave reflection analysis

Understanding and accurately estimating infragravity wave dissipation and reflection, and thus correctly predicting potential storm damage and modelling shoreline change, relies upon the infragravity wave signal being accurately separated into its shoreward and seaward propagating components. Two types of method exist to separate incident and reflected waves; (1) array methods which use the wave signal from two or more spatially separated wave sensors in a cross-shore array (e.g., Gaillard et al., 1980; Frigaard and Brorsen, 1995; Van Dongeren et al., 2007), and (2) methods that use data from co-located wave and velocity sensors at a single location (e.g., Guza and Bowen, 1976; Sheremet et al., 2002). Each method has associated advantages and disadvantages and both are susceptible to error from, for example, asynchronous timing between instruments, not accounting for bed slope correctly, and inadequate sensor positioning. An additional source of error that is less related to experimental design and particularly prevalent in field data is uncorrelated signal noise. The presence of noise has been shown to introduce a positive bias to wave reflection estimates from co-located wave and velocity sensor

methods and attempts have been made to alleviate this (e.g., Tatavarti et al., 1988; Huntley et al., 1999). However, an investigation into the impact of uncorrelated noise on incident and reflected wave components estimated from array based techniques, and the potential to remove ensuing biases, is currently lacking. This is discussed further in Section 4.1.

2.4 Infragravity waves on rocky shore platforms

As much as 80% of the world's coastlines are characterised by rocky or cliffed coasts (Emery and Kuhn, 1982; Bird, 2000). A typical morphological feature of these coasts are intertidal shore platforms; (quasi-)horizontal or low gradient rocky surfaces that occur within or close to the intertidal zone and are commonly backed by cliffs (Trenhaile, 1987; Sunamura, 1992). Shore platform surfaces range from very smooth (like a sandy beach) to very rough and depend on geological factors such as the lithology and stratigraphic characteristics of the bed.

Two types of shore platform are generally recognised (Sunamura, 1992); Type A are gently sloping ($\beta \approx 0.01-0.05$) platforms that usually extend into the sub-tidal zone (Figure 2.7A,C), and Type B are near-horizontal with a steep low tide cliff, the upper part of which can sometimes be seen at low tide (Figure 2.7B,D). Shore platform type is predominantly controlled by tidal range (e.g., Dickson et al., 2013), with Type A platforms typical of large tidal environments (mean spring tidal range >2 m), whereas Type B platforms tend to occur where the tidal range is small (mean spring tidal range <2 m).

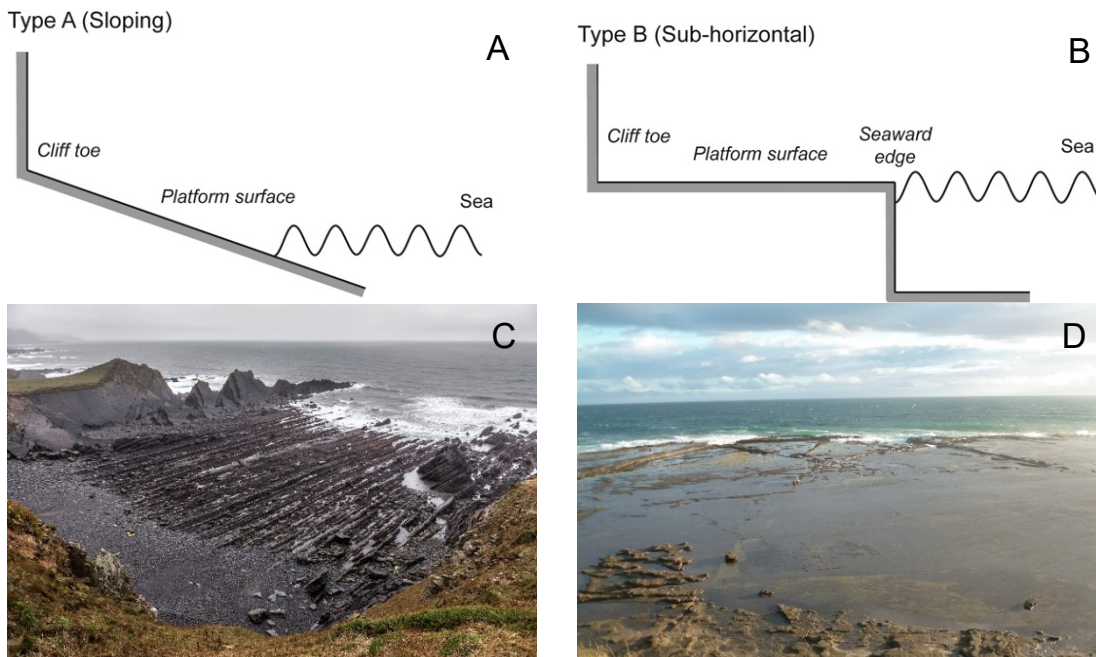


Figure 2.7. Cross-sectional schematics of Type A (A) and Type B (B) shore platforms (from Ogawa et al., 2012). Example of a Type A shore platform at Hartland Quay, UK (C), and an example of a Type B shore platform at Leigh, New Zealand (D).

Shore platforms directly control the transformation of waves propagating across its surface, and thus the amount of wave energy reaching the shoreline. Unlike sandy beaches, shore platforms do not have the capacity to adjust their morphology in response to hydrodynamic phenomenon, nor do they recover from the impact of storm events in the way that beaches do during calm conditions. Although a number of studies have acknowledged the presence of infragravity energy on shore platforms, detailed field investigations of infragravity wave dynamics have focused almost entirely on sandy beaches. Given what is known from the existing infragravity wave literature, infragravity waves likely play an important role in delivering wave energy to the base of cliffs backing shore platforms, including sea-swell energy by increasing the local water depth allowing sea-swell waves to propagate further onshore. As well as direct impact on the cliff itself, infragravity waves could be an important mechanism in removing cliff-toe debris, as well as extending the influence of wetting and drying cycles across the platform at all tidal stages, thus enhancing the erosion of weak rocks.

2.4.1 Previous research on Type B platforms

Over the last decade, general interest in rocky coasts has grown resulting in several recent field investigations of wave characteristics on Type B shore platforms, particularly in the meso and microtidal environments of New Zealand and Australia (e.g., Ogawa et al., 2011,2015; Marshall and Stephenson, 2011; Dickson and Pentney, 2012). These studies have tended to focus on the spatial and temporal variation of short wave energy and, in some cases, potential cliff impact caused by waves. Much fewer studies have been undertaken on Type A platforms (e.g., Poate et al., 2016).

To date, the only published study to focus on infragravity wave transformation over rocky shore platforms is that of Beetham and Kench (2011) who undertook two field experiments on Type B shore platforms in New Zealand (Oraka and Rothesay Bay). Although, the study was relatively modest in its analysis and experimental set-up, which consisted of 5 pressure sensors deployed for 22 hours and 36 hours on the Oraka and Rothesay Bay platforms, respectively. Additionally, wave conditions were low-moderate with maximum offshore wave heights not exceeding 1.5 m. The results of this study were mostly consistent with those from sandy beaches, with infragravity wave height linearly dependent on the offshore sea-swell wave height and increasing shoreward with maximum infragravity wave heights of 0.20 m and 0.17 m measured at the cliff toe of the Oraka and Rothesay Bay platforms, respectively. Infragravity wave shoaling, quantified as the change in wave height from the platform edge to the cliff toe, was strongest on the wider Oraka platform and at high tide when the water level over the platform was at its highest. Dissipation of sea-swell waves across the platform was lowest at high tide and it is suggested that the super-elevation of water level at this time caused by the largest infragravity waves has the potential to aid sea-swell waves in reaching and acting upon the cliff face. A shoreward increase in infragravity wave height and the increasing

significance of infragravity energy relative to sea-swell energy on the inner platform, analogous to dissipative sandy beaches, has also been observed on other shore platforms in New Zealand and in Australia by Marshall and Stephenson (2011) and Ogawa et al. (2011).

Ogawa et al. (2015) showed that whether infragravity or sea-swell waves dominate on a shore platform can be parameterized using the relative water depth (h/H) at the platform edge. A threshold value of 1.1 was observed, above which sea-swell frequencies dominate the wave spectra, and below which infragravity frequencies dominate the wave spectra as sea-swell waves typically break on the platform edge. Such a parametrization would not be applicable on Type A platforms given the absence of an outer platform edge.

2.4.2 Coral reef studies

Despite the limited number of infragravity wave investigations on shore platforms, several field studies have acknowledged infragravity wave behaviour on coral reefs (e.g., Lugo-Fernandez et al., 1998; Brander et al., 2004; Pomeroy et al., 2012; Pequignet et al., 2014; Cheriton et al., 2016). These environments, predominantly existing in microtidal regions, are analogous in shape to Type B shore platforms with a relatively horizontal reef flat and a low tide reef step equivalent to the edge of a shore platform. Arguably the most important similarity is the bed roughness, and thus high friction coefficient compared to sandy beaches, which has the potential to influence wave transformation processes.

A three week field study by Pomeroy et al. (2012) at Ningaloo Reef, Western Australia, in low-moderate forcing conditions ($H_o < 1.6$ m) found that infragravity energy on the reef flat is generated predominantly by breakpoint forcing on the steep (1:20) fore-reef slope. Infragravity dissipation was observed on the reef and bed friction was determined

to be the dominant mechanism; non-linear energy transfers were only responsible for infragravity energy growth, whilst the effects of bed friction caused the infragravity waves to become less steep, thus reducing the likelihood of breaking. The rate of infragravity wave damping by bottom friction was much smaller than that of the sea-swell waves and was tidally modulated, with the highest dissipation rates occurring in shallower water. These findings regarding infragravity wave generation at the breakpoint and frictional dissipation were supported by numerical simulations and by Van Dongeren et al. (2013) using XBeach.

Contrary to these studies, Pequignet et al. (2014) observed 87% of the infragravity energy on a reef on the island of Guam to be generated by bound wave theory in more energetic offshore wave conditions ($H_o \approx 3$ m). Frictional dissipation was considered to be the primary dissipation mechanism on the shallow reef flat, but it is also suggested that a slight decrease in infragravity energy could be caused by weak breakpoint forced waves that are out of phase with the bound waves, thus some energy cancellation occurs.

Little frictional dissipation of infragravity waves was observed by Cheriton et al. (2016) on a smooth reef in the Marshall Islands during storm conditions ($H_o = 6$ m, $T_p = 16$ s). However, infragravity waves of up to 1 m at the shoreline were found to be highly skewed and asymmetrical which could indicate the emergence of infragravity wave breaking. Shimozono et al. (2015) provide further support for the breaking of infragravity waves using numerical simulations on an 800 m wide fringing reef, in which infragravity waves evolved into bores due to non-linear steepening.

2.4.3 Waves Across Shore Platforms (WASP) project

Whilst the number of wave transformation studies on Type B shore platforms and similar coral reef environments has increased in recent years, there is a distinct knowledge gap

concerning transformation processes of both sea-swell and infragravity waves on Type A shore platforms in macrotidal regions. To address this knowledge gap, the Waves Across Shore Platforms (WASP) project was launched in 2014 as a collaboration between the universities of Plymouth (UK), Bangor (UK), Auckland (New Zealand), and Deltares (Netherlands). The aim of the WASP project is to understand how waves propagate across shore platforms and develop a capability to reliably model this process. Field data were collected at 5 macrotidal, Type A shore platforms of differing width, slope, bed roughness, and wave climate around the UK. Early results presented by Poate et al. (under review) show that sea-swell waves are dissipated through depth limited breaking in the surf zone and that, despite significant differences in bed roughness between the platforms, friction can largely be neglected in sea-swell wave transformation. The proportion of total energy in the infragravity frequency band increased shoreward at all sites, consistent with previous observations, however the total infragravity energy was predominantly shown to be either constant or decreasing in the shoreward direction. Further analysis of this vast dataset will investigate the extent to which recent infragravity wave forcing and dissipation trends that have been observed on sandy beaches apply to Type A shore platforms, particularly under energetic forcing conditions, which is currently missing from the literature.

2.5 Summary

Infragravity waves are an important hydrodynamic phenomenon that play an important role in a number of nearshore processes. In particular, their frequent dominance in the inner surf and swash zones means they are often the primary morphodynamic driver in shallow water, thus a detailed understanding of infragravity waves is imperative for accurately predicting beach erosion and modelling shoreline change. Despite considerable research efforts dating back to the 1950s, several aspects of infragravity

waves are not fully understood and new questions have arisen from recent studies. The influence of offshore wave period on infragravity energy levels at the shoreline, as well as transformation and dissipation through the surf zone, is a particularly important area in need of further insight since higher wave periods (i.e., swell) tend to induce increased levels of groupiness and is thus directly related to the infragravity wave generation mechanisms. Indeed, a large proportion of recent infragravity wave studies into dissipation and reflection took place on low fetch, sea dominated coastlines or in a laboratory; the extent to which their findings apply to more exposed coasts warrants further study. To accurately investigate the propagation, transformation, and reflection of infragravity waves, relevant methodological shortcomings must be overcome. Perhaps the most important of these, assuming a logical experimental set-up, is failing to address the potential impact of signal noise. Without this, the results of wave reflection analysis may be subject to significant error.

The vast majority of field studies on infragravity waves have taken place on sandy beaches. Rocky shore platforms, especially Type A (i.e., macrotidal) platforms, present a virtually unstudied environment in terms of infragravity wave research. However, given the prevalence of rocky coastlines around the world, this is a critical knowledge gap in face of climate change and rising sea levels.

Chapter 3

Methodology

The following chapter begins by describing the study sites and experimental set-up of the two major field experiments that form the basis of the subsequent results chapters (5 and 6). Next, the techniques used to post-process the data are outlined, followed by the data analysis methods that can be broadly categorised into frequency and time domain techniques. Since the fundamental difference between infragravity and sea-swell waves is their frequency, and correspondingly their wavelength, analysis in the frequency domain allows the infragravity and sea-swell components to be isolated and temporal (i.e., with offshore forcing) and spatial (i.e., with surf zone position) variations within the two frequency bands can be explored. Furthermore, differences in energy and wave transformation at individual infragravity frequencies can be examined. It is also within the frequency domain that the infragravity data are separated into incident and reflected components; an essential step when investigating the transformation and possible dissipation of infragravity waves. Analysis in the time domain is primarily based around the cross-correlation of time series, particularly the infragravity time series and the wave group envelope. This is performed to provide insight into the generation mechanism of the infragravity waves and, if bound, their release relative to the breakpoint of sea-swell waves. Additional methods that are more specific to individual aspects of the research are included in the relevant chapter.

3.1 Study sites

3.1.1 Perranporth

Perranporth, located at the southern end of Perran Sands, is a macrotidal, dissipative beach on the north coast of Cornwall, UK (Figure 3.1). Perranporth is a relatively straight

beach facing west-northwest so is fully exposed to the dominant westerly wave approach, receiving both Atlantic swell and locally generated wind waves. An offshore wave buoy recorded an annual mean significant wave height of 1.57 m and a mean peak wave period of 10.5 s since its insertion on 18th December 2006 (CCO, 2017). Wave approach is typically shore-normal. Perranporth's relatively featureless profile, along with its cross-shore dominance and exposure to a wide range of swell and wind waves, make it an excellent site for studying infragravity wave behaviour under different levels of offshore forcing. Interestingly, some of the first ever field observations of infragravity waves were made at Perranporth by Tucker (1950).

Perranporth has a semi-diurnal tidal regime with mean spring and neap tidal ranges of 6.1 m and 3.1 m, respectively. On spring low tides, the intertidal region has an average cross-shore length (dune foot to water's edge) of 500 m and a longshore extent of approximately 4 km (Droskyn Point to Ligger Point). The beach is characterised by a low-gradient ($\beta \approx 0.012$ over the intertidal region), concave profile composed of medium quartz sand with a median grain size D_{50} of 0.33 mm (Inch et al., 2015; Prodger et al., 2016). Most of the intertidal region is relatively featureless and alongshore homogeneous; however, well pronounced bar-rip morphology is exposed during spring low tides (Austin et al., 2013; Masselink et al., 2014; Poate et al., 2014).

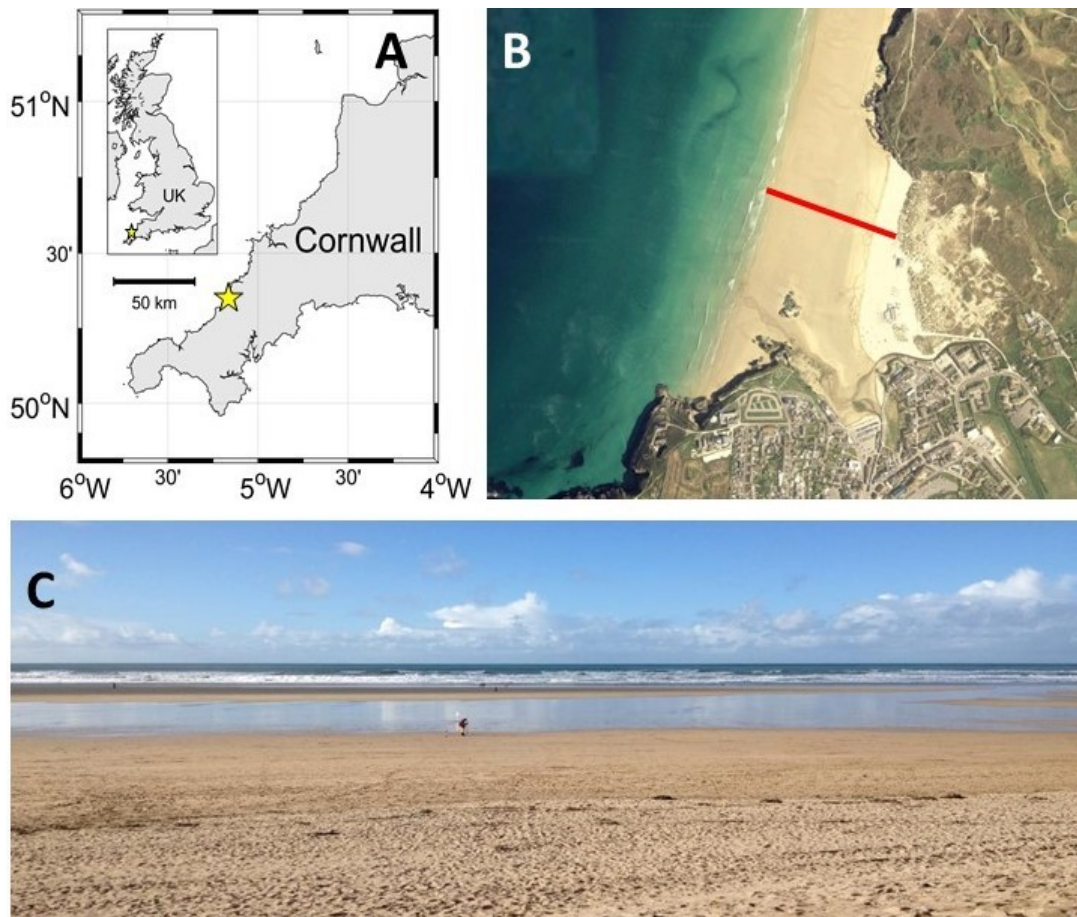


Figure 3.1. Location map of Perranporth Beach, UK (A), aerial image of Perranporth Beach taken around low tide (B), and photograph taken from the top of the instrument array line (C). Solid red line in (B) indicates the instrument array location and is ~500 m long. The high tide line in (B) is also clear as the change in sand colour.

3.1.2 Freshwater West

Freshwater West is a wide, dissipative beach situated in the county of Pembrokeshire, southwest Wales (Figure 3.2). Freshwater West was chosen as a study site as it provided an ideal opportunity to deploy two parallel instrument arrays; one on the rocky shore platform ($\beta \approx 0.018$), and another on the sandy beach ($\beta \approx 0.011$), to compare bed roughness effects on wave transformation processes under identical forcing conditions.

Tides are semi-diurnal and macrotidal with a mean spring tidal range of 6.5 m. The beach is composed of medium sand and backed by an extensive dune system. Bar and rip features are pronounced in the region below mean low tide, whilst the upper beach

remains comparatively flat. The southern end of the beach has a Type A rocky shore platform, known as Little Furznip, which is backed by low cliffs reaching an elevation of 55 m. The shore platform has an intertidal width of approximately 210 m and is composed primarily of sandstone. Facing west-southwest, Freshwater West is fully exposed to the prevailing south-westerly waves, receiving a combination of short wind waves and long period swell. An offshore wave buoy deployed off the Pembrokeshire coast recorded an annual mean significant wave height of 1.80 m and a mean peak wave period of 9.2 s since its deployment during September 2014 (CEFAS, 2017).

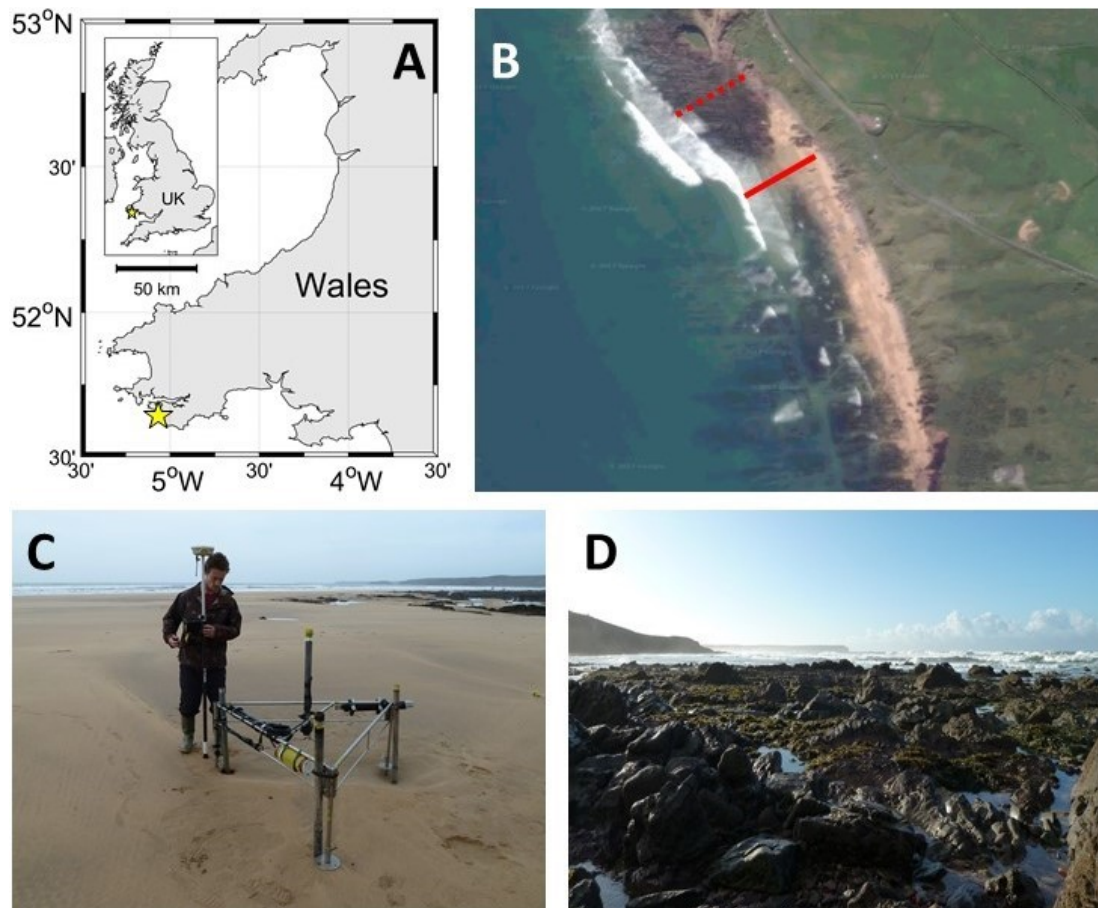


Figure 3.2. Location map of Freshwater West, UK (A), aerial image of Freshwater West (B), and photographs illustrating the beach (C) and platform (D) study areas. The solid and dotted red lines in (B) are the beach and platform instrument arrays, respectively, and represent a distance of ~150 m.

3.2 Experimental Set-up

3.2.1 Perranporth

Data were collected at Perranporth Beach for 33 consecutive tidal cycles from 7 to 24 November 2014 (18 days). Pressure observations were logged continuously at 4 Hz by 15 *in situ* pressure sensors (RBR Solo D-Wave). The sensors were situated in a cross-shore array spanning 372 m (Figure 3.3); 13 were located between the mean spring high and mean spring low tide lines and 2 were located slightly above the mean spring high tide line to capture inner surf zone data during periods of particularly energetic wave forcing that are typical for the time of year.

The spacing of the pressure sensors ranged from 15 m to 35 m and was chosen strategically to ensure the accurate estimation of incident and reflected infragravity auto-spectra. This involved the use of irregular spacing (i.e., three different sensor spacing's existed for every trio of pressure sensors) and a general reduction in separation distance closer to shore to account for the shortening of the infragravity waves. Numerical simulations, as outlined in Chapter 4, were used to ensure the suitability of the spacing before a definitive layout was decided upon.

The pressure sensors were securely attached to screw in ground anchors or small (~0.6 m) lengths of scaffolding and buried so that the pressure sensor was ~0.1 m below the bed. The pressure sensors were buried in order to be less intrusive and to avoid corruption of the pressure signal caused by dynamic pressure variations from accelerating and decelerating flows. In addition to the buried pressure sensors, a rig equipped with a co-located pressure sensor and an acoustic Doppler velocimeter (Nortek Vector) sampling 0.2 m above the bed, both logging at 4 Hz, was deployed for 10 selected tides during the latter half of the study period. The instrument transect was measured on alternate low tides using real time kinematic DGPS (± 0.03 m accuracy) and experienced little

variability throughout the field experiment. The elevation of the instruments was measured at every low tide and adjustments were made, as necessary, to keep the instruments at their intended elevations with respect to the bed level.

Offshore wave conditions were measured by a Datawell Directional Waverider buoy, maintained by the Channel Coastal Observatory (www.channelcoast.org), located just offshore of Perranporth Beach at a depth of approximately -17 m ODN (Ordnance Datum Newlyn). The buoy measures vertical heave and horizontal displacement at 1.28 Hz to generate directional spectra and statistics including significant and maximum wave height, peak wave period, and directional spread.

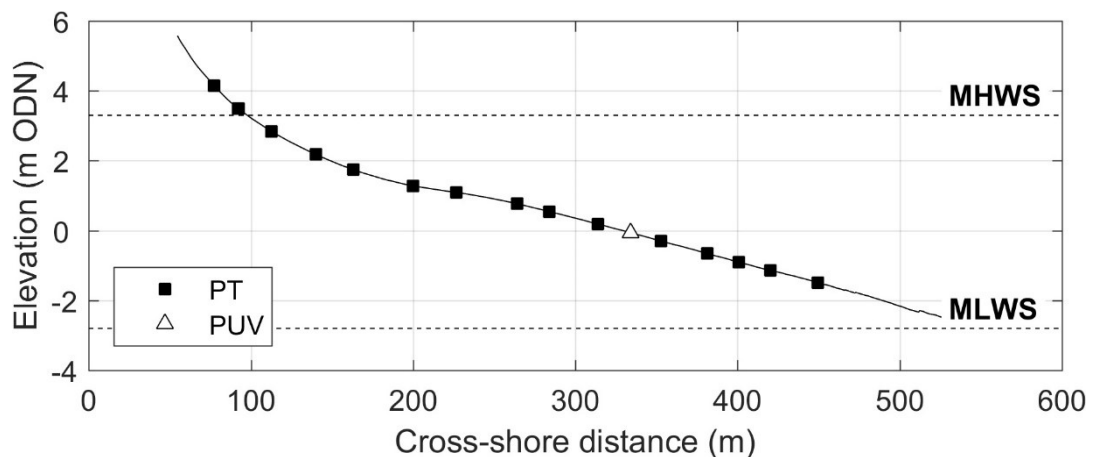


Figure 3.3. Mean beach profile during the Perranporth field experiment showing the positions of the buried pressure sensors (PT) and the co-located pressure and velocity rig (PUV). Elevation is relative to Ordnance Datum Newlyn (ODN), which is ~ 0.2 m above mean sea level in the southwest of England. Horizontal lines indicate mean sea level (MSL), mean high water springs (MHWS), and mean low water springs (MLWS).

3.2.2 Freshwater West

The Freshwater West field experiment took place from 27 October to 13 November 2015 (17 days) during which data were collected for 31 consecutive tidal cycles. This experiment formed part of the Waves Across Shore Platforms (WASP) project with the aim to improve the understanding of how waves propagate across shore platforms of varying morphology and develop a capability to reliably model this process (Poate et al.,

2016; Poate et al., under review). Since this project is concerned primarily with the transformation of sea-swell waves, the instrumental set-up (e.g., sensor spacing) differs slightly from the Perranporth field experiment.

Time-synchronised pressure sensors were deployed simultaneously in two cross-shore arrays; one on the rocky platform at the south end of Freshwater West known as Little Furznip, and one on the section of sandy beach immediately south of the platform. This part of the beach was chosen over the main beach because of its closer proximity and more similar bed slope to that of the platform array.

The platform array consisted of 14 pressure sensors (RBR Solo D-Wave) logging continuously at 8 Hz. The pressure sensors were individually secured inside steel housings to protect them from loose rocks and bolted onto the platform with a spacing of approximately 10 m, increasing to 15 m between the most seaward five sensors, thus spanning a cross-shore distance of 150 m from the mean high tide line close to the cliff toe to around 40 m from the seaward edge of the platform (Figure 3.4B). A rig equipped with a co-located pressure sensor and an acoustic Doppler velocimeter (Nortek vector) was also deployed close to the centre of the platform with both instruments logging at 8 Hz and at a height of 0.2 m above the bed.

The beach array comprised of 7 intertidal pressure sensors spaced at 15 m, thus spanning a distance of 90 m (Figure 3.4A). The 5 most seaward sensors were logging at 8 Hz (RBR Solo D-Wave) whilst the 2 most landward sensors logged at 6 Hz (RBR Duo). The sensors were deployed attached to screw in ground anchors as they were during the Perranporth experiment so that the pressure sensor was ~ 0.1 m below the bed. The smaller number of pressure sensors in the beach array was due to the WASP project being primarily focused on shore platforms. A rig equipped a co-located pressure sensor and an acoustic Doppler

velocimeter, set up identical to that on the platform, was deployed in the centre of the array.

All instruments and the profiles transecting the instrument arrays on both the beach and the platform were measured using an electronic total station (± 0.002 m accuracy). Given the significantly irregular morphology of the platform, the survey areas were also mapped at a very high-resolution (3.1 mm at 10 m distance) using a Leica P20 terrestrial laser scanner. Using a number of scan positions on the beach and the platform, the instrument arrays were scanned to 20 m either side and the data were used to create a digital elevation model with a 0.1 x 0.1 m resolution grid. For ease of analysis, positions measured by the total station and the laser scanner were rotated and translated onto a local coordinate system.

Offshore forcing conditions at an approximate depth of -40 m ODN are measured by a Datawell Directional Waverider buoy, managed by Swansea University, situated 4 miles off St Govans Head, Pembrokeshire, and approximately 10 miles southeast of Freshwater West. Statistics such as significant wave height and peak period, as well as spectral information, are recorded every 30 minutes.

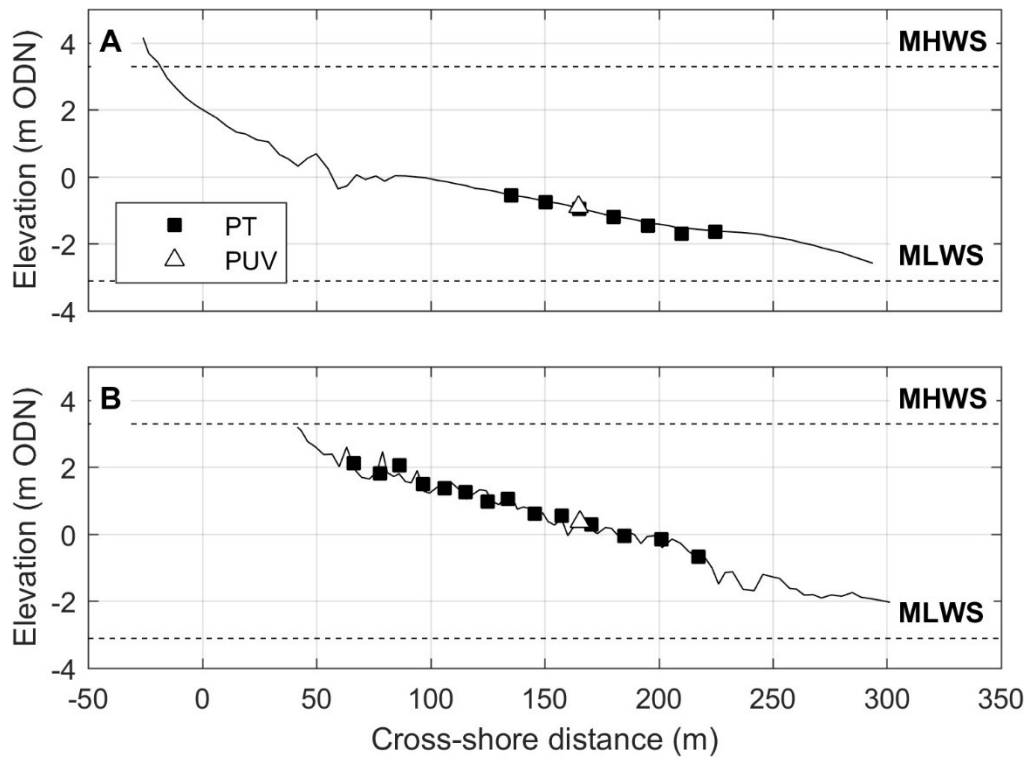


Figure 3.4. Beach (A) and platform (B) profiles during the Freshwater West field experiment showing the positions of the pressure sensors (PT) and the co-located pressure and velocity rigs (PUV). Elevation is relative to Ordnance Datum Newlyn (ODN). Horizontal lines indicate mean high water springs (MHWS) and mean low water springs (MLWS).

Before determining the influence of the platform roughness on infragravity wave dynamics, it is first necessary to quantify the level of surface roughness on the beach and the platform. Here, two methods are used to parameterize the surface roughness, both calculated from 1x1 m square tiles of the digital elevation models (DEMs) produced from the laser scanner data. The first method is analogous to estimating significant wave height in the time domain and is calculated as $K_{\sigma} = 4\sigma_z$, where σ_z is the standard deviation associated with the square tiles. This parameter has been used successfully by, for example, Lowe et al. (2005) who found wave dissipation across a coral reef to compare well with K_{σ} . The second parameter is based on rugosity and is calculated as $K_R = A_r/A_a - 1$, where A_r is the actual surface area of the square tiles and A_a is the geometric surface area (1 m^2). A perfectly smooth surface yields $K_R = 0$. The roughness parameters

K_σ and K_R are alongshore-averaged across the 40 m wide sections on the beach and platform to obtain an estimate of the cross-shore variability in bed roughness.

The higher roughness on the platform compared to the beach is immediately clear from the amount of blue and yellow in Figure 3.5A-B which shows the detrended DEMs for the platform and beach. Bedding planes on the platform are orientated southeast-northwest and thus are oblique to the direction of wave approach. The visual difference in bed roughness between the beach and platform portrayed by the DEMs is supported by the two roughness parameters in Figure 3.5C-F. Mean (\pm one standard deviation) values of K_σ are 0.01 ± 0.01 and 0.14 ± 0.02 on the beach and platform, respectively. The same values of K_R are 0.003 ± 0.001 and 0.06 ± 0.02 , respectively. Variability across the profiles is fairly minimal and therefore the roughness is well characterised by these mean values. The slight increase in roughness at the seaward end of the beach profile is caused by the presence of mega-ripples on the day of the laser scan.

A sensitivity analysis of difference grid sizes was undertaken by Poate et al. (under review) and it was concluded that, whilst values of K_σ and K_R are sensitive to grid size up to 3 m, a 1 m grid explains almost 80% of the roughness. This size grid also reflects the scale at which the near-bed orbital excursion would be affected by bed roughness.

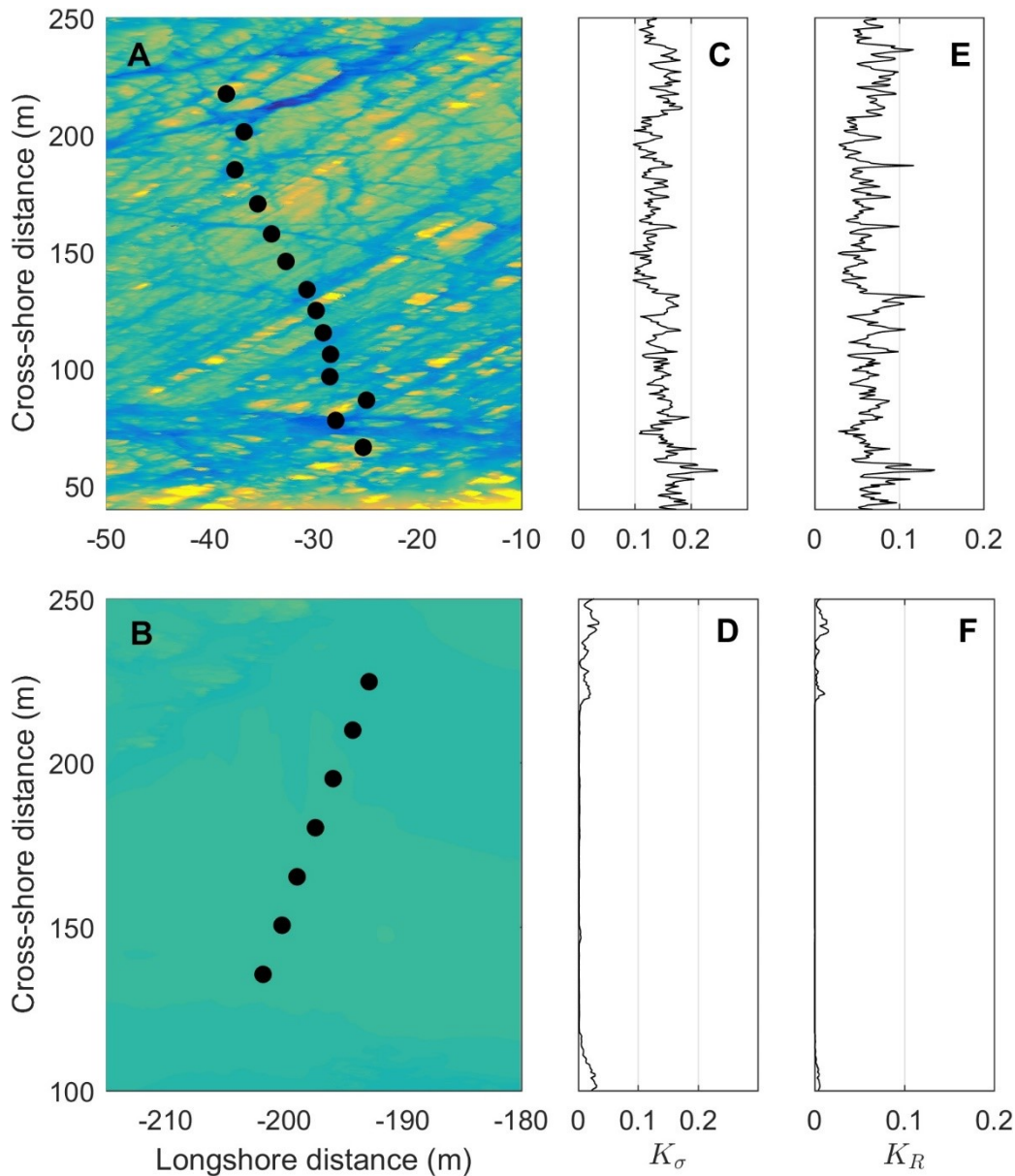


Figure 3.5. Detrended digital elevation models (DEMs) with pressure sensor locations (black dots) for the platform (A) and beach (B) at Freshwater West. Cross-shore variation in alongshore averaged roughness based on standard deviation K_σ and rugosity K_R for the platform (C, E, respectively) and beach (D, F, respectively). Offshore (west) is at the top of the figures. The colour scale of the DEMs goes from -1 m (dark blue) to +1 m (yellow).

3.3 Post-processing

The results presented in subsequent chapters come almost entirely from the analysis of time series data of pressure and velocity logged by the in situ pressure sensors and acoustic Doppler velocimeters. These time series are considered to be both stationary and stochastic.

Time series from the Perranporth experiment were made up of 8192 data points centred around high tides which, given the sampling rate of 4 Hz, allows for a time series length of ~34 minutes. Longer time series were used in estimating the bispectrum, which is discussed in Section 3.4.1.4. The Freshwater West time series also consisted of 8192 data points but, considering the higher sampling rate of 8 Hz, gives a shorter time series length of ~17 minutes.

Whilst the analysis of longer time series tends to yield more reliable and higher resolution results, in macrotidal environments time series length is a trade off against tide induced changes in water depth at the sensors which subsequently impacts the stationarity of the observed hydrodynamics. The longer length of the Perranporth time series is justified since the data are centred around high tide when the change in tide level is at a minimum. Time series from Freshwater West are extracted from throughout the tide in order to analyse data from a range of water depths. Shorter time series are used in this case since the tidal excursion increases away from the extremes of high and low tide.

The absolute pressure recorded by the sensors was converted to hydrostatic pressure by subtracting the low tide barometric pressure logged by when the sensors were exposed. The barometric pressure was assumed to vary linearly between consecutive low tides. In converting pressure to water surface elevation, depth attenuation of the pressure signal is corrected for by applying a frequency-dependent depth attenuation factor $K(f)$ derived from linear wave theory as

$$K(f) = \frac{\cosh(kz)}{\cosh(kh)} \quad (3.1)$$

where z is the height of the pressure sensor above the bed. The small amount of attenuation caused by the pressure sensors at Perranporth and those in the beach array at Freshwater West being buried was corrected for using poroelastic theory (Raubenheimer

et al., 1998) where the ratio between pressure below the bed P_{z_b} and hydrostatic pressure P_0 is

$$\frac{P_{z_b}}{P_0} = \exp^{-kz_b} \quad (3.2)$$

where z_b is the depth of the pressure sensor below the surface. Time series that were found to be intermittently wet and dry (i.e., measuring in the swash zone) were rejected from further analysis.

In the calculation of bulk parameters and time series filtering, a frequency based classification is used to distinguish between infragravity and sea-swell waves. In the literature, the split frequency between infragravity and sea-swell waves is commonly 0.05 Hz (e.g., Guza and Thornton, 1985; Henderson et al., 2006; Guedes et al., 2013) or 0.04 Hz (e.g., Masselink, 1995; Ruessink, 1998a; Fiedler et al., 2015). A split frequency of 0.04 Hz is preferred on coastlines exposed to long period swell, and is applied herein, to avoid the inclusion of sea-swell energy in the infragravity band. During the Perranporth field experiment, for example, a maximum peak wave period of 20 s (0.05 Hz) was measured by the offshore wave buoy. Auto-spectra from the most seaward pressure sensors at both Perranporth and Freshwater West show that 0.04 Hz is situated in the spectral valley separating the dominant infragravity and sea-swell spectral peaks for much of the data, thus providing further support for the use of this split frequency. The lower limit of the infragravity band is set at 0.005 Hz to ensure that any tidal signal is not included. Additionally, the spectral density at frequencies below this cut-off was not well correlated with the offshore sea-swell energy, indicating that there may be another mechanism forcing these very low frequency waves. The high frequency cut-off for the sea-swell band of 0.33 Hz corresponds to a depth attenuation of ~80% at the most seaward pressure sensors during spring high tides, thus higher frequencies could not be corrected

confidently. Furthermore, a high frequency cut-off of 0.3-0.4 Hz for the sea-swell band has been frequently used in previous studies (e.g., Elgar et al., 1992; Ruessink, 1998a,b; Henderson et al., 2006; Guedes et al., 2013).

3.4 Data analysis

A time series, in which a quantity x is expressed as a function of time t , can also be expressed in the frequency domain by its amplitude X as a function of frequency f . Therefore, $x(t)$ and $X(f)$ can be seen as two representations of the same physical process and are directly related via the Fourier transform as

$$X(f) = \int_{-\infty}^{\infty} x(t)e^{-2\pi ift} dt \quad (3.3)$$

and

$$x(t) = \int_{-\infty}^{\infty} X(f)e^{2\pi ift} df \quad (3.4)$$

where dt and df are the sampling interval and frequency bandwidth, respectively. The following sections outline the analysis techniques that were performed in the time and frequency domains.

3.4.1 Frequency domain analysis

3.4.1.1 The auto-spectrum

For Equations 3.3 and 3.4 to be applicable, a time series must be continuously sampled and infinitely long. However, actual time series are of finite length consisting of N data points with a sampling interval equal to $1/f_s$, where f_s is the sampling frequency. In terms of the time series analysed herein, N is 8192 and the sampling interval is 0.250 s and

0.125 s for time series sampled at 4 Hz and 8 Hz, respectively. The Fourier transform of a finite time series, termed the discrete Fourier transform, is expressed as

$$X(k) = \sum_{n=0}^{N-1} x(n)e^{-2\pi i kn/N} \quad k = 0, 1, \dots, N-1 \quad (3.5)$$

or in its complex polar notation as

$$X(k) = \sum_{n=0}^{N-1} x(n) \left(\cos \frac{2\pi kn}{N} - i \sin \frac{2\pi kn}{N} \right) \quad (3.6)$$

$$k = 0, 1, \dots, N-1$$

Determination of the auto-spectrum; that is, the contribution of component frequencies to the time series, is derived from the one-sided periodogram function $P(k)$ defined as

$$P(k) = \frac{|X(k)|^2}{f_s N} \quad \text{for } k = 0, \frac{N}{2} \quad (3.7)$$

$$P(k) = \frac{2|X(k)|^2}{f_s N} \quad \text{for } k = 1, \dots, \frac{N}{2} - 1 \quad (3.8)$$

Since the discrete Fourier transformation produces N Fourier coefficients that are symmetrical about $N/2$ (i.e., the second half are the complex conjugates of the first half), the periodogram function uses only the first half of the Fourier coefficients and doubles them, excepting $P(0)$ and $P(N/2)$. Spectral density estimates $S(f)$, with units of $\text{m}^2 \text{Hz}^{-1}$, are obtained by normalising the one-sided periodogram such that the sum of $P(k)$ is proportional to the variance of the time series (Parseval's theorem):

$$\text{Variance} = \frac{f_s}{N} \sum_{k=0}^{N/2} P(k) \quad (3.9)$$

To improve the reliability of the spectral estimates, the Welch method is adopted in which the time series is partitioned into 50% overlapping segments of equal length and a Hanning taper is applied to reduce spectral leakage. Spectral density estimates are calculated for each segment and these are subsequently averaged at each frequency. The use of smaller segments increases the degrees of freedom ν of the spectral estimates but decreases the frequency bandwidth since $df = f_s/l$, where l is the segment length. That is to say, ν and df are inversely proportional as an improvement in one will be detrimental to the other. For 50% overlapping segments tapered with a Hanning window, Nuttall (1971) shows that ν is given by

$$\nu = 3.82 \left(\frac{N}{l} \right) - 3.24 \quad (3.10)$$

Here, an l value of 1024 is used with all the time series, giving $\nu = 27$ and $df = 0.0039$ Hz for the Perranporth data and $df = 0.0078$ Hz for the Freshwater West data. Confidence limits on $S(f)$ are derived from the chi-squared χ^2 distribution and ν (Jenkins and Watts, 1968) by

$$S(f) \frac{\nu}{\chi_{\nu, 1-\alpha/2}^2} \geq S(f) \geq S(f) \frac{\nu}{\chi_{\nu, \alpha/2}^2} \quad (3.11)$$

where α is the significance level, herein 0.05 (i.e., 95% confidence level). Processing details of the auto-spectrum are given in Table 3.1.

Table 3.1. Auto-spectra processing details for Perranporth and Freshwater West.

Dataset	Time series length N	Sampling frequency f_s	Segment length l	Frequency bandwidth df	Degrees of freedom ν	Confidence multipliers 95%
Perranporth	8192	4 Hz	1024	0.0039 Hz	27	1.85 0.63
Freshwater West	8192	8 Hz	1024	0.0078 Hz	27	1.85 0.63

3.4.1.2 The cross-spectrum

The relationship between two time series is determined by the cross-spectrum which evaluates the level of covariance between the time series in the frequency domain. Information gleaned from the cross-spectrum is utilized to investigate the cross-shore structure of wave energy at different frequencies and in the estimation of incident and reflected auto-spectra. To obtain an estimate of the cross-spectrum, spectral estimates are calculated for two time series and are cross-correlated using the correlation theorem by

$$S_{xy}(f) = S_x(f) \cdot S_y^*(f) \quad (3.12)$$

where S_x and S_y are the spectral estimates of two time series and $*$ denotes the complex conjugate. The resulting cross-spectral estimates are complex with the real part (co-spectrum) Co_{xy} giving a measure of the in-phase co-variance, and the imaginary part (quadrature spectrum) Q_{xy} giving a measure of the out of phase co-variance. Cross-spectral estimates have the same degrees of freedom as the spectral estimates since they are calculated and averaged in the same way.

The spectral coherence C_{xy} , calculated as

$$C_{xy}(f) = \frac{|S_{xy}(f)|^2}{S_x(f) \cdot S_y(f)} \quad (3.13)$$

provides a measure between 0 and 1 representing the level of linearity between two time series. In calculating C_{xy} , smoothed estimates (through the use of segments or frequency averaging) of S and S_{xy} must be used, otherwise $C_{xy} = 1$. The confidence threshold for significant coherence is calculated following Shumway and Stoffer (2000) as

$$C_{95\%} = \frac{F_{2,\nu-2}(\alpha)}{\frac{\nu}{2} - 1 + F_{2,\nu-2}(\alpha)} \quad (3.14)$$

where F is the inverse of the cumulative distribution function of the F-distribution. For $\nu = 27$ and $\alpha = 0.05$, $C_{95\%} = 0.21$.

Even if the level of coherence is very high, it is possible for corresponding frequency components to have different phase. The phase spectrum θ_{xy} is derived from the cross-spectrum by

$$\theta_{xy}(f) = \tan^{-1} \left\{ \frac{\text{Im}(S_{xy}(f))}{\text{Re}(S_{xy}(f))} \right\} \quad (3.15)$$

3.4.1.3 Reflection analysis

Since infragravity waves can, at least partly, reflect from the shoreline and propagate seaward, a time series of nearshore water surface elevation is a superposition of incident and reflected infragravity waves. These two signals must be separated to accurately investigate the transformation and dissipation of infragravity waves. Here, an array method (see Section 4.1 for a description of reflection analysis techniques) is used to derive incident and reflected auto-spectra, corresponding energy fluxes and wave heights, and reflection coefficients.

The estimation of incident $S^+(f)$ and reflected $S^-(f)$ auto-spectra requires the auto-spectra from three pressure sensors in a cross shore array, as well as the cross-spectra between the three different sensor pairs, and is achieved using the first order formulae of Gaillard et al. (1980) as

$$S^+(f) = \frac{\bar{S} - \bar{Co} + \bar{Q}}{2S_a} \quad (3.16)$$

$$S^-(f) = \frac{\bar{S} - \bar{Co} - \bar{Q}}{2S_a} \quad (3.17)$$

where

$$\bar{S} = S_1 + S_2 + S_3 \quad (3.18)$$

$$\bar{Co} = Co_{21} \cos(k\Delta x_{21}) + Co_{31} \cos(k\Delta x_{31}) + Co_{32} \cos(k\Delta x_{32}) \quad (3.19)$$

$$\bar{Q} = Q_{21} \sin(k\Delta x_{21}) + Q_{31} \sin(k\Delta x_{31}) + Q_{32} \sin(k\Delta x_{32}) \quad (3.20)$$

and

$$S_a = \sin(k\Delta x_{21}) + \sin(k\Delta x_{31}) + \sin(k\Delta x_{32}) \quad (3.21)$$

where S , Co , and Q represent the auto-, co-, and quadrature spectra respectively, Δx is sensor spacing, and subscript numbers denote sensor location (S) or sensor pair (C , Q , Δx).

The incident and reflected spectra were used to calculate corresponding frequency-dependent energy fluxes ($F^+(f)$ and $F^-(f)$, respectively) as

$$F^\pm(f) = S^\pm(f)\sqrt{gh} \quad (3.22)$$

Here, \sqrt{gh} is used since the water depth does not exceed 6 m in the Perranporth and Freshwater West datasets, therefore $c_g \sim \sqrt{gh}$. Frequency-dependent reflection coefficients $R^2(f)$ were calculated as the ratio of $F^-(f)$ to $F^+(f)$. Bulk infragravity energy fluxes F^\pm and reflection coefficients R^2 were estimated by integrating over the infragravity frequency range where

$$F^{\pm} = \int_{0.005 \text{ Hz}}^{0.04 \text{ Hz}} F^{\pm}(f) df \quad (3.23)$$

and

$$R^2 = F^- / F^+ \quad (3.24)$$

Energy fluxes are used to investigate the dissipation of infragravity waves because energy flux is conservative with changing water depth, therefore any growth (decay) in infragravity energy flux represents a true gain (loss) in energy. Changes in infragravity wave height or spectral density, however, can occur as a result of wave shoaling when the rate of energy delivery at the shoreline is unchanged.

Incident and reflected infragravity dissipation rates (D^+ and D^- , respectively), normalised by water depth, are calculated as

$$D^{\pm} = \frac{1}{h} \frac{\Delta F^{\pm}}{\Delta x} \quad (3.25)$$

where ΔF^{\pm} represents the change in F^{\pm} corresponding to Δx , where Δx in this instance is the spacing between wave reflection estimates (i.e., the centre of the wave triplet arrays).

3.4.1.4 The bispectrum

Bispectral analysis, first introduced by Hasselmann et al. (1963), detects phase coupling between frequency triads and it is these triad interactions that allow non-linear energy transfers within a wave field. Non-linear energy transfers can play an important role in infragravity energy loss through either energy being transferred back to sea-swell frequencies, or energy transfers within the infragravity band than can lead to a more asymmetric and skewed infragravity wave shape and eventual infragravity wave breaking.

The discrete bispectrum B_{f_1, f_2} describes triad interactions between frequencies f_1 and f_2 , and their sum frequency $f_3 = f_1 + f_2$, and is calculated as

$$B_{f_1, f_2} = E[\mathcal{F}_{f_1} \mathcal{F}_{f_2} \mathcal{F}_{f_3}^*] \quad (3.26)$$

where $E[]$ is the ensemble average of complex Fourier coefficients \mathcal{F} at frequencies f_1 , f_2 , and f_3 , and * represents complex conjugation. Equation 3.26 shows that if the average triple product of the Fourier coefficients is zero (i.e., the Fourier modes are independent of each other), then the bispectral estimate will have a zero value. Whereas, any non-linear interaction occurring between the frequencies in the triad will produce a non-zero bispectral estimate. Bispectral estimates are complex and must be represented in their imaginary or real parts to obtain information about the direction and magnitude of energy transfers within the triad. Here, the imaginary part of the bispectrum is used, following Herbers et al. (2000), with positive interactions indicating a transfer of energy from f_1 and f_2 to their sum f_3 , and negative interactions indicating an energy transfer from f_3 to f_1 and f_2 .

A normalised measure of the strength of the coupling between the interacting wave components is provided by the bicoherence b_{f_1, f_2}^2 , computed as

$$b_{f_1, f_2}^2 = \frac{|B_{f_1, f_2}|^2}{E[|\mathcal{F}_{f_1} \mathcal{F}_{f_2}|^2] E[|\mathcal{F}_{f_3}|^2]} \quad (3.27)$$

following Kim and Powers (1979). Whilst there are several methods of calculating b_{f_1, f_2}^2 , the method accepted here is frequently used in the literature (e.g., Elgar and Guza, 1985; Guedes et al., 2013) and assures that $0 \leq b_{f_1, f_2}^2 \leq 1$. The 95% confidence level on bicoherence $b_{95\%}^2$ is calculated as

$$b_{95\%}^2 \geq \sqrt{(6/\nu)} \quad (3.28)$$

based on the approximation of Haubrich (1965). It is suggested by Elgar and Guza (1985) that this method overestimates the 95% confidence level and that a value of approximately one quarter of this is more realistic; however, Equation 3.28 is used here as a conservative approach and only bispectral estimates with corresponding bicoherence values above the 95% confidence level are shown in this thesis. A more detailed description of bispectral analysis is given by, for example, Hasselmann et al. (1963) and Collis et al. (1998).

Bispectral analysis was performed on the Perranporth dataset and, to increase the degrees of freedom and thus reduce $b_{95\%}^2$, extended time series of 16384 data points (~68 minutes) were used. Bispectral estimates were averaged to give a frequency resolution of 0.0117 Hz and 186 degrees of freedom, giving $b_{95\%}^2 = 0.18$.

3.4.1.5 Significant wave height

The significant wave height is determined for the infragravity H_{inf} and sea-swell H_{ss} frequency bands by integrating over the spectral variance associated with each band such that

$$H_{inf} = 4 \sqrt{\int_{0.005 \text{ Hz}}^{0.04 \text{ Hz}} S(f) df} \quad (3.29)$$

$$H_{ss} = 4 \sqrt{\int_{0.04 \text{ Hz}}^{0.33 \text{ Hz}} S(f) df} \quad (3.30)$$

Significant incident and reflected infragravity wave heights (H^+ and H^- , respectively) were calculated following Equation 3.29 and replacing S with S^+ and S^- , respectively.

3.4.2 Time domain analysis

Analysis in the time domain is performed using filtered infragravity η_{inf} and sea-swell η_{ss} time series. This filtering is performed in the frequency domain whereby the discrete Fourier transformation of the time series is taken and multiplied by a filter function that has a value of unity at the passband frequencies and zero at all other frequencies, before undergoing an inverse Fourier transformation back into the time domain.

3.4.2.1 Wave group envelope and the groupiness factor

To investigate the relationship between infragravity waves and groups of short waves, the wave group envelope $A(t)$ is calculated following the method of List (1991) as

$$A(t) = \frac{\pi}{2} |\eta_{ss}(t)|_{low} \quad (3.31)$$

where subscript *low* indicates a low pass filter of frequency 0.04 Hz, and $||$ represents absolute value. The wave group envelope reflects the modulation of sea-swell amplitudes on the time scale of wave groups and is demonstrated in Figure 3.6.

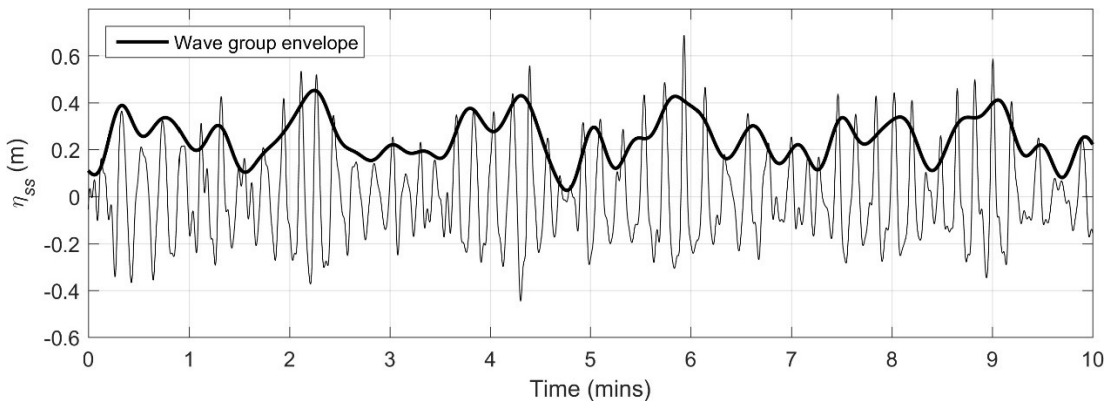


Figure 3.6. Example of a detrended sea-swell time series η_{ss} and associated wave group envelope $A(t)$, obtained through the method of List (1991), from tide 27 ($H_o = 0.67$ m, $T_p = 11.4$ s, $h = 4.07$ m) of the Perranporth field experiment.

The grouped nature of the sea-swell waves is investigated further by calculated the groupiness factor GF , also proposed by List (1991), as

$$GF = \frac{\sqrt{2\overline{var[A(t)]}}}{\overline{A(t)}} \quad (3.32)$$

where var is the variance and the overbar symbolises the mean. The groupiness factor provides a normalised value between 0 and 1 representing the groupiness of the wave group envelope.

3.4.2.2 Cross-correlation

The time domain's alternative to the cross-spectrum is cross-correlation analysis; a function that measures the relationship between two random, stationary time series with zero mean by applying a time shift to one of the series. The cross-correlation between the infragravity time series and the wave group envelope provides information about the generation mechanism of infragravity waves and, conversely, the modulation of sea-swell waves by infragravity waves in the surf zone. This is expressed as

$$r(\tau) = \frac{\langle \eta_{inf}(t)A(t + \tau) \rangle}{\sigma_{\eta_{inf}}\sigma_A} \quad (3.33)$$

where τ is a time shift, $\langle .. \rangle$ denotes a time averaging operator, and $\sigma_{\eta_{inf}}$ and σ_A are the standard deviations of η_{inf} and A , respectively. If the infragravity waves are predominantly bound to the short waves groups, then the cross-correlation coefficient at a time lag of zero r_0 will approach -1 because the two time series will theoretically be 180° out of phase.

Given that adjacent points in the time series are not independent, the 95% confidence interval on the cross-correlation coefficients is calculated following the method of Garrett and Toulany (1981) using a reduced number of points N_* where

$$N_* = \frac{1}{N} + \frac{2}{N^2} \sum_{j=1}^{N_0} (N - \tau) r_{xy}(\tau) \quad (3.34)$$

where N is the original number of points, $r_{xy}(\tau)$ is the lagged auto-correlation coefficient of the product of the two time series to be correlated, and N_0 is the number of lags until a zero-crossing is made by $r_{xy}(\tau)$. The 95% confidence is then calculated as

$$1.96/\sqrt{N_*} \quad (3.35)$$

(Jenkins and Watts, 1968). For the Perranporth data, for which cross-correlation was applied, N_0 averaged 78, resulting in $N_* \approx 1260$ and a mean 95% confidence interval on zero correlation of ± 0.08 .

The propagation of incident and reflected infragravity waves relative to the wave group envelope is further investigated by calculating the predicted travel time, according to linear wave theory, for short wave groups to travel to shore from a specified location and for reflected infragravity waves to return to that location. Ruju et al. (2012) describe this mathematically as

$$\mathcal{T}(\tau, x) = \int_x^0 \left(\frac{1}{c_g} + \frac{1}{c} \right) dx - \tau = 0 \quad (3.36)$$

where c is the shallow water wave velocity calculated as \sqrt{gh} .

3.5 Summary

This chapter has provided a detailed description of the two field experiments undertaken as part of this project and the data analysis techniques that will be applied in the following chapters. Time series analysis in the frequency domain allows for the infragravity and sea-swell components to be separated and analysed independently, as well as an investigation of frequency-dependence within the infragravity band. The infragravity

component is further decomposed into its incident and reflected parts which provide information on the dissipation and reflection of infragravity waves. Following the application of a frequency domain filter, cross-correlation in the time domain is used to investigate the generation and release of infragravity waves, as well as their influence on short wave height in the surf zone.

Chapter 4

Correcting for noise in wave reflection measurements¹

The aim of this chapter is to use simulated time series of water surface elevation to investigate the impact of noise on wave reflection estimates using the array method of Gaillard et al. (1980). A mathematical function is developed to provide a correction for the observed bias in incident and reflected spectra and corresponding reflection coefficients. This function is applied to field data to demonstrate its value. The results presented in this chapter are principally applicable to the array method of Gaillard et al. (1980) and will be utilised in the succeeding results chapters with the Perranporth and Freshwater West field datasets. However, to demonstrate that the approach used here to derive the correction technique can equally be applied to other reflection methods that use an array of pressure observations, a noise correction for the method of Van Dongeren et al. (2007) is presented in Appendix A.

Firstly, a brief introduction to wave reflection analysis and potential sources of error is given. The methodology specific to this chapter is described next, followed by the simulation results that demonstrate the impact of noise and are used to develop the correction technique. An assessment of the importance of wave angle on the reflection method is then given followed by a demonstration of the noise correction method being applied using data from the Perranporth field experiment. Due to the complexity of the equation symbols, parameters used specifically in this chapter have been defined both in

¹ *Published as:*

Inch, K., Davidson, M., Masselink, G., Russell, P. 2016. Accurate estimation of wave reflection on a high energy, dissipative beach. *Journal of Coastal Research*, SI 75, 877-881.

Inch, K., Davidson, M., Masselink, G., Russell, P. 2017. Correcting wave reflection estimates in the coastal zone. *Coastal Engineering*, 119, 65-71.

the text and in a separate glossary found at the end of this chapter, to serve as an ‘aide memoire’ for the reader.

4.1 Background

Several methods exist to decompose a two-dimensional wave signal propagating over a horizontal bed into its incident and reflected components using cross-shore arrays of spatially separated wave sensors. These methods utilise the phase difference between pairs of wave sensors to provide information on the propagation of the incident and reflected waves. Early methods to calculate wave reflection typically use an array of only two wave sensors (e.g., Goda and Suzuki, 1976; Morden et al., 1976); however, these techniques suffer from singularities at a discrete number of critical frequencies where the distance between the two wave sensors is equal to an integer number of half the corresponding wavelength. To overcome this limitation and estimate wave reflection over a wider frequency range, several newer techniques have been developed that use the wave records from three or more wave sensors (e.g., Gaillard et al., 1980; Mansard and Funke, 1980; Battjes et al., 2004), thus providing a range of wave sensor pairs and separation distances for use in the analysis.

The alternative method of calculating wave reflection is to use co-located wave and velocity sensors (e.g., Guza and Bowen, 1976; Sheremet et al., 2002), where the direction of wave propagation is estimated using information on the slope of the sea surface provided by the cross-shore current. These methods have the advantage of estimating wave reflection at a singular cross-shore location, whereas the wave reflection estimate from an array method is the average value for the spatial extent of the array, which may be quite large. Additionally, methods that use co-located wave and velocity sensors are not affected by variations in the bathymetry. However, it is critically important to have the wave and velocity sensors located at the same horizontal location as even a small

spatial separation can have important effects on the resulting wave reflection estimates (Huntley et al., 1999). In many cases, array methods remain the preferred approach as wave sensors are typically less intrusive to deploy in the field than current sensors making them less of a hazard to water users and more robust so can be deployed over longer periods of time; this is essential when investigating the climatology of infragravity waves. Furthermore, wave sensors are far more economical if wave reflection estimates are required at several cross-shore locations (Hughes, 1993), thus allowing for a better appreciation of the spatial variability in infragravity wave dynamics.

Most array methods used to separate incident and reflected waves are designed for two-dimensional waves propagating over a horizontal bed and do not account for the effects of sloping bathymetry such as that of a natural beach. Therefore, depending on the wave conditions and bed slope, errors in the analysis are likely when used in such conditions. Baldock and Simmonds (1999) demonstrated that relatively simple modifications are required to adapt the separation method of Frigaard and Brorsen (1995) to account for shore-normal linear waves propagating over a bed with arbitrary bathymetry. Their analysis showed that neglecting the shoaling effects of waves can lead to large errors in the estimated reflection coefficient in cases of low wave reflection. Furthermore, accounting for bathymetry variations was found to be crucial to avoid significant errors (up to 90%) in estimating the incident and reflected wave amplitudes.

Signal noise is a source of error that may impact wave reflection estimates in both laboratory and field experiments. Signal noise can be defined as unwanted (and often unknown) modifications to a signal picked up during data measurement and/or processing. In nearshore wave data, this is typically caused by water surface variability that is unrelated to wave motion, sometimes referred to as ‘surface chop’. In terms of array methods, the coherence between sensor pairs can be used to determine the level of signal

noise and, as such, noise is wave motion that is present at one sensor but absent or significantly altered at another sensor. Other potential sources of signal noise include electronic noise, sensor set-up relative to standing wave nodes, and human disturbance. Using simulated time series of surface elevation and velocity with known true reflection coefficients and added uncorrelated noise, Huntley et al. (1999) showed that the presence of noise in the data can introduce a significant positive bias to the reflection coefficients estimated from co-located wave gauge and velocity sensor methods. In an attempt to overcome this, Tatavarti et al. (1988) developed a method using principal component analysis to separate the elevation and velocity time series into orthogonal eigenvector combinations, thus allowing the correlated parts of the two time series to be separated from undesired noise. This technique was validated by Huntley et al. (1999) who also demonstrate that the bias in reflection coefficients estimated using other co-located wave and velocity sensor methods can be corrected for by using the estimated reflection coefficient itself and the coherence between the estimated incident and reflected waves. A similar investigation into the effect of noise on wave reflection estimates using array methods is currently lacking.

4.2 Methodology

The water surface elevation η at two cross-shore locations, x_1 and x_2 , separated by Δx , is given by linear wave theory as

$$\eta(x_1, t) = a^+ \cos(\omega t - kx_1 + \phi^+) + a^- \cos(\omega t + kx_1 + \phi^-) \quad (4.1)$$

$$\begin{aligned} \eta(x_2, t) = & a^+ \cos(\omega t - kx_1 - k\Delta x + \phi^+) \\ & + a^- \cos(\omega t + kx_1 + k\Delta x + \phi^-) \end{aligned} \quad (4.2)$$

where a is wave amplitude, ω is wave angular frequency ($2\pi f$), ϕ is wave phase, and superscript + and – denote incident and reflected waves, respectively. The signs of the

terms are for an onshore-directed x -axis. Equations 4.1 and 4.2 show that between cross-shore locations x_1 and x_2 , the incident and reflected waves are phase shifted by $-k\Delta x$ and $k\Delta x$, respectively.

Equations 4.1 and 4.2 are used to generate simultaneous time series of water surface elevation at three cross-shore locations on a horizontal bed. For the purpose of the simulations, wave amplitudes a_i and a_r are independent of frequency and all waves travel at the shallow water wave speed. A range of simulations were performed with incident wave amplitudes between 1 and 10 m, known reflection coefficients between 0 and 1, and with normally distributed, random noise added to the time series at known signal-to-noise ratios (SNR). While the use of constant wave amplitudes and reflection coefficients across all frequencies is not representative of real field data, it means that each frequency provides an independent estimate of the incident and reflected spectra for any particular SNR, wave amplitude and true reflection coefficient. This allows mean values of error, and confidence intervals on these estimates, to be calculated for particular frequency ranges. By running a range of simulations with different wave amplitudes and noise levels, errors and corresponding confidence intervals can be predicted for each frequency bin in a measured spectrum.

Synthetic time series were generated with 4096 data points and a sampling frequency of 4 Hz. Smooth spectral estimates were computed as outlined in Section 3.4.1.1, giving a frequency resolution of 0.0039 Hz and 12 degrees of freedom. The spectra are then separated into incident $S^+(f)$ and reflected $S^-(f)$ components using the first order formulae of Gaillard et al. (1980) described in Section 3.4.1.3. The incident and reflected spectra are then used to estimate the amplitude reflection coefficient $R(f)$ by

$$R(f) = \sqrt{\frac{S^-(f)}{S^+(f)}} \quad (4.3)$$

Note that the amplitude reflection coefficient differs from the squared reflection coefficient R^2 (Equation 3.24) in that it gives a measure of the reflected wave amplitude rather than energy.

The purpose of using an array method with three wave sensors is to avoid singularities occurring at a discrete number of critical frequencies. However, sensor triplets must be chosen intelligently with spatial separations that mitigate the coincidence of critical frequencies, otherwise these frequencies will suffer similar effects to those from using a two sensor array. This chapter will focus on the frequency range 0.01-0.33 Hz. The low frequency cut-off of 0.01 Hz was chosen to avoid any adverse effects radiating from the singularity that always occurs at 0 Hz, regardless of whether two or three wave sensors are used. The high frequency cut-off of 0.33 Hz was chosen as it coincides with the upper limit of the frequency range used to define sea-swell waves throughout this thesis (see Section 3.3). Furthermore, wave reflection from natural coastlines has been found to be negligible at higher frequencies, particularly on dissipative beaches. The use of this frequency range allows for spectral estimates at 82 discrete frequencies. To avoid the influence of singularities across the entire frequency range of interest, three different array set-ups are used in the simulations to satisfy frequency ranges 0.01-0.05 Hz, 0.05-0.20 Hz, and 0.20-0.33 Hz, respectively. The full range of simulations was performed for each array set-up and spectral estimates for the corresponding three frequency ranges were concatenated providing the full spectrum of interest for each combination of simulation parameters. The cross-shore location of the sensors in each array set-up is given in Table 4.1, whilst Figure 4.1 illustrates the effect of singularities before and after the concatenation of the spectral estimates. For example, the array set-up optimized for the

frequency range 0.01-0.05 Hz causes singularities to occur at 0.0976 Hz and 0.3438 Hz (Figure 4.1A). The concatenated auto-spectra is shown in Figure 4.1D and is free of singularities. The reflection line distance (i.e., the distance between the most shoreward sensor and the shoreline) was not found to impact the results significantly and so an arbitrary value of 20 m was chosen.

Table 4.1. Cross-shore sensor locations x_{1-3} used in the array set-ups optimized for frequency ranges 0.01-0.05 Hz, 0.05-0.20 Hz, and 0.20-0.33 Hz, respectively. The shoreline is at $x = 0$.

Frequency Range	x_1 (m)	x_2 (m)	x_3 (m)
0.01 – 0.05 Hz	20	45	65
0.05 – 0.20 Hz	20	30	38
0.20 – 0.33 Hz	20	25	32

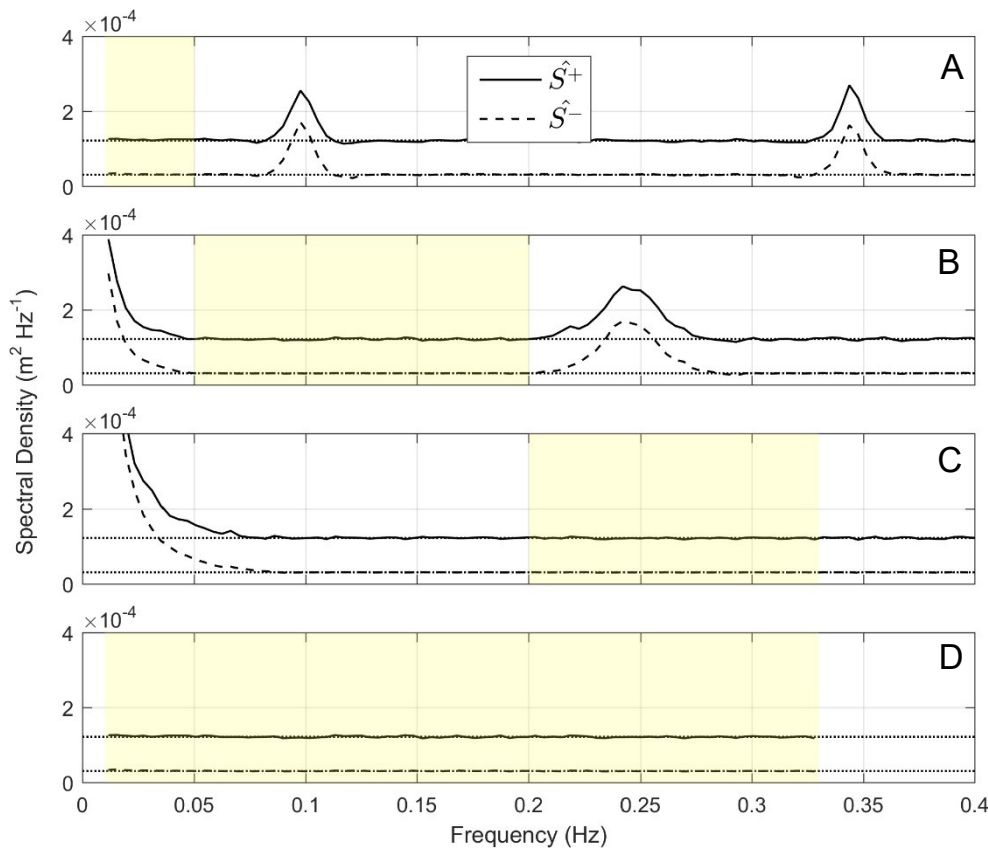


Figure 4.1. Estimated incident \widehat{S}^+ and reflected \widehat{S}^- auto-spectra estimated using the array set-ups given in Table 4.1 optimized for frequency ranges 0.01-0.05 Hz (A), 0.05-0.20 Hz (B), and 0.20-0.33 Hz (C). Shaded areas indicate the frequency ranges used to form the concatenated auto-spectra (D). Dotted lines indicate the target incident S^+ and reflected S^- auto-spectra. In this example, wave amplitude is 1 m and $R = 0.5$.

4.3 Results

For each simulation scenario, an assessment is made of the accuracy to which the incident and reflected spectra, and corresponding reflection coefficients, are reproduced by the decomposition method of Gaillard et al. (1980). Mean coherence between the three synthetic time series is calculated to investigate the extent to which coherence can be used as a proxy for SNR. By averaging the coherence between the three pairs of time series, fluctuations due to standing wave nodes and antinodes are removed. Throughout this section, target values for incident and reflected spectra and reflection coefficients (i.e., those fixed in the simulations) are denoted by S^+ , S^- , and R , respectively. Estimated values are differentiated from target values by the following overbar symbol $\widehat{}$, and corrected estimates are represented by an additional subscript c . Error in the estimated values is always positive and is therefore referred to as a bias.

4.3.1 Noise correction

Figure 4.2 shows \widehat{S}^+ , \widehat{S}^- , coherence, and \widehat{R} for a wave amplitude of 2 m, $R = 0.3$, and four different SNRs. With no noise added to the time series, \widehat{S}^+ and \widehat{S}^- are estimated accurately with mean values within 3% of their respective target values. \widehat{R} is also estimated with reasonable accuracy with a mean value of 0.31. The absence of noise is reflected in a mean coherence value of 0.98. A similar accuracy can be found across all simulations where no noise has been added to the time series, thus providing confidence in the method. For $\text{SNR} = 2.5$, both \widehat{S}^+ and \widehat{S}^- are positively biased by 12.2% and 11.7% of S^+ respectively, and mean coherence is reduced to 0.72. With \widehat{S}^+ and \widehat{S}^- being biased by very similar amounts, the difference in magnitude between \widehat{S}^+ and \widehat{S}^- is largely unchanged but becomes smaller relative to the overall magnitudes, thus introducing a positive bias to \widehat{R} which has a mean value of 0.43. This is further demonstrated by a SNR

of 1.7, which creates a bias in \widehat{S}^+ and \widehat{S}^- of 25.8% and 26.3% of the S^+ magnitude respectively and increases the mean \widehat{R} value to 0.50. A SNR of 0.7 causes \widehat{S}^+ and \widehat{S}^- to be biased by 137.4% and 136.0% of S^+ respectively, which raises the mean \widehat{R} from 0.3 to 0.78. However, this is somewhat of an extreme case and coherence values for this simulation are well below the 95% confidence threshold and therefore would not be considered significant if found in real data.

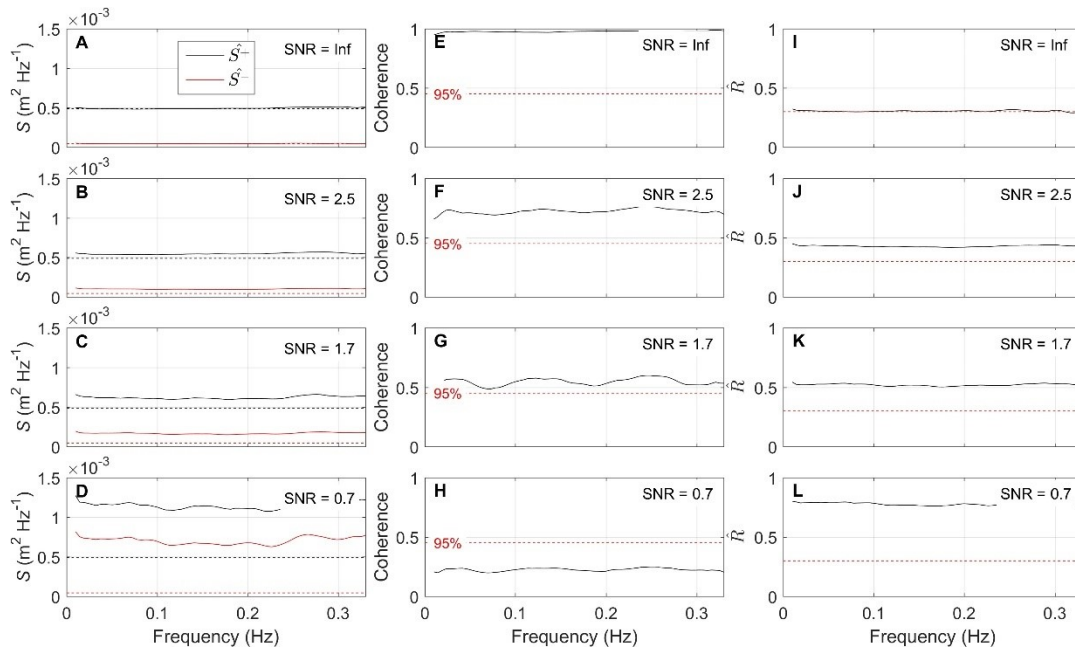


Figure 4.2. Estimated incident \widehat{S}^+ and reflected \widehat{S}^- spectra (A-D), coherence (E-H), and estimated reflection coefficients \widehat{R} (I-L) for SNR = Inf, 2.5, 1.7, and 0.7 as stated on the figure. Dashed lines in (A-D) are the target incident S^+ and reflected S^- spectra. Red dashed line in (E-H) is the 95% confidence threshold on coherence of 0.45 for 12 degrees of freedom (Shumway and Stoffer, 2000). Red dashed line in (I-L) is the target reflection coefficient R of 0.3. Wave amplitude is 2 m.

Whilst the bias in \widehat{S}^+ and \widehat{S}^- is dependent only on the wave amplitude and SNR, the bias in \widehat{R} becomes more significant for lower values of true reflection. This is because, while \widehat{S}^+ and \widehat{S}^- are biased by the same magnitude, as the true reflection coefficient decreases from 1 the bias becomes increasingly larger relative to S^- than S^+ . For a given SNR, the bias in \widehat{S}^+ and \widehat{S}^- increases linearly with increasing wave amplitude. Therefore, normalising by \widehat{S}^+ conveniently removes the dependency of bias on wave amplitude,

allowing the bias from all simulations to be investigated simultaneously as a function of coherence. This is shown in Figure 4.3 where the data have been band-averaged across frequencies thus providing one estimate for each simulation scenario. The frequency smoothing, which increases the degrees of freedom of the estimates from 12 to 984, is performed to provide the best possible estimates from which to predict the expected bias in real data.

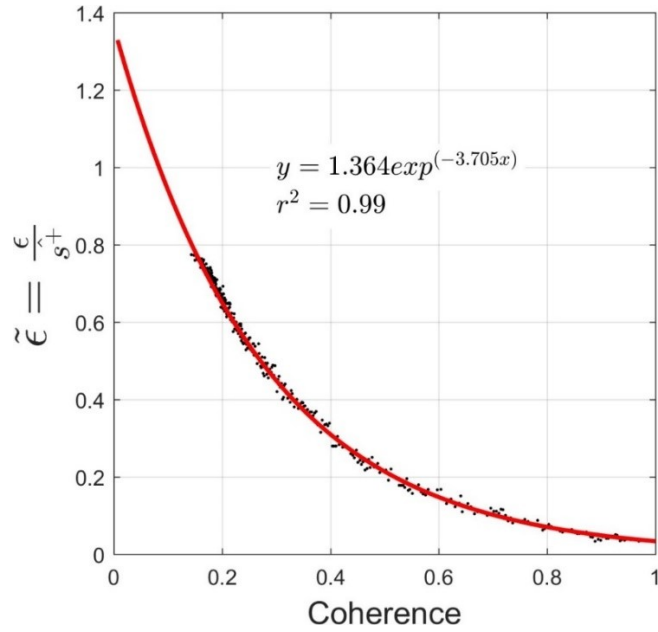


Figure 4.3. Normalised bias $\tilde{\epsilon}$ (ϵ/\widehat{S}^+ , where ϵ is bias) versus coherence for all wave amplitudes, true reflection coefficients, and SNRs. Data have been smoothed providing one estimate per simulation and 984 degrees of freedom. Solid red line is an exponential regression function with coefficients and accuracy given on the figure.

The normalised bias $\tilde{\epsilon}$ is shown to decrease exponentially with increasing coherence and an exponential regression function is fit to the data with excellent agreement and a correlation coefficient r^2 of 0.99 (all r^2 values reported herein are significant at the 95% level). This function allows for a prediction of the bias $\hat{\epsilon}$ by

$$\hat{\epsilon} = \widehat{S}^+ 1.364exp(-3.705C) \quad (4.4)$$

where C is coherence. Corrected incident \widehat{S}_c^+ and reflected \widehat{S}_c^- spectra can then be calculated as

$$\widehat{S}_c^+ = \widehat{S}^+ - \widehat{\epsilon} \quad (4.5)$$

$$\widehat{S}_c^- = \widehat{S}^- - \widehat{\epsilon} \quad (4.6)$$

and corrected reflection coefficients \widehat{R}_c as

$$\widehat{R}_c = \sqrt{\frac{\widehat{S}_c^-}{\widehat{S}_c^+}} \quad (4.7)$$

4.3.2 Confidence intervals

Reducing the amount of frequency smoothing and degrees of freedom shown in Figure 4.3 increases the amount of scatter around the exponential regression function. However, no frequency smoothing and 12 degrees of freedom still yields an r^2 of 0.93. Regardless of the level of frequency smoothing, values of $\tilde{\epsilon}$ remain normally distributed (according to the Shapiro-Wilk normality test) around the exponential regression function. This allows 95% confidence intervals on $\tilde{\epsilon}$ to be calculated for different levels of coherence and degrees of freedom using the t-distribution. These are shown in Figure 4.4A for coherence bins of 0.1 and degrees of freedom between 12 and 984 as a result of averaging over particular frequency ranges in the spectrum. Confidence intervals are shown to increase with decreasing coherence and the rate of this increase is steeper for lower degrees of freedom. For example, for 12 degrees of freedom, 95% confidence intervals are ± 0.085 and ± 0.026 for coherence values between 0.5 and 0.6, and 0.9 and 1.0, respectively. Whereas the same confidence intervals for 120 degrees of freedom (approximately equivalent to averaging over the infragravity band) are ± 0.037 and ± 0.010 , respectively. Note that confidence intervals are not calculated for coherence bins that include values below the 95% confidence threshold for the respective degrees of freedom. The rate of change in the confidence intervals with coherence is relatively constant and linear regression models yield r^2 between 0.81 and 0.99 for the different degrees of

freedom. Figures. 4.4b and 4.4c show that the slope m and intercept b from the linear regressions can be predicted accurately ($r^2 = 0.97$ and 0.98 , respectively) using exponential regression functions and the degrees of freedom.

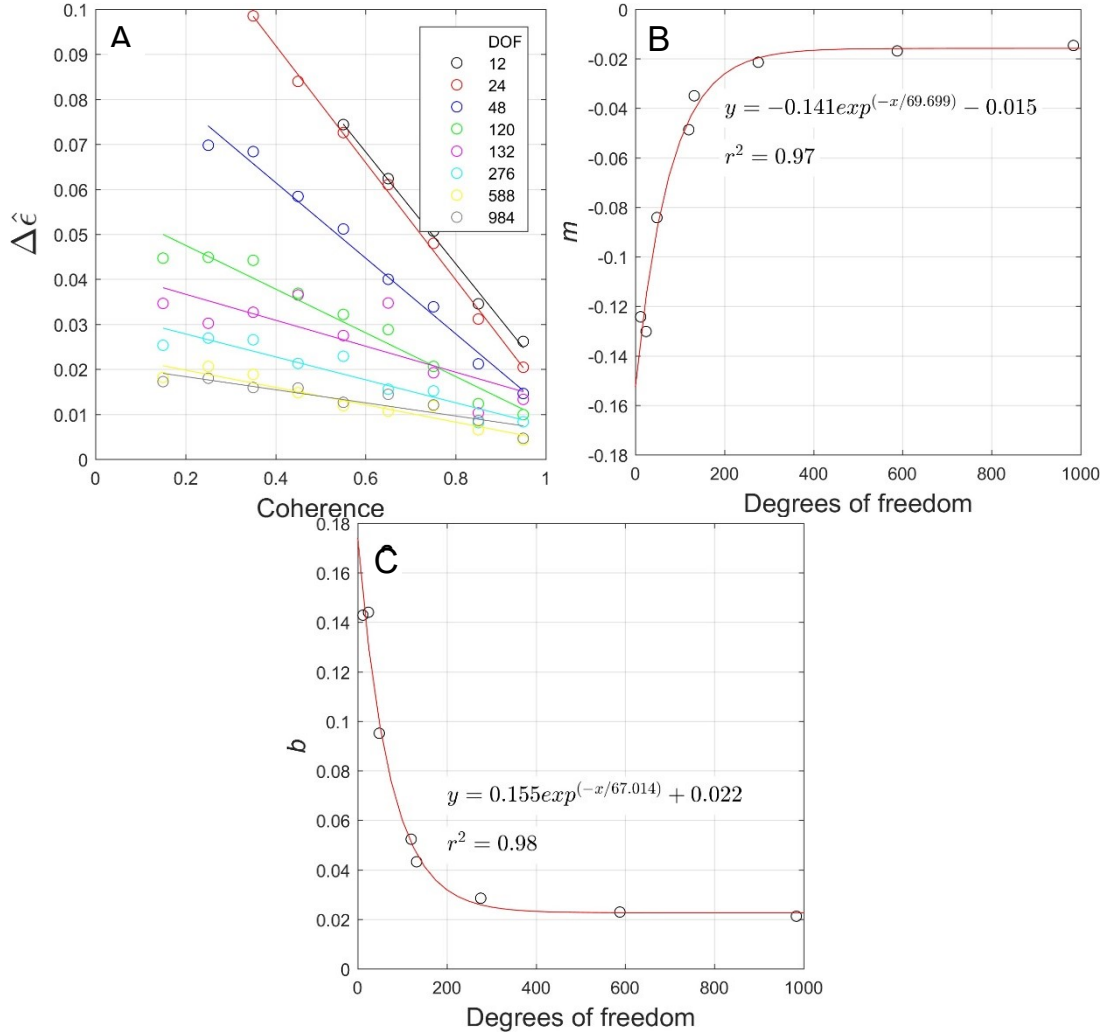


Figure 4.4. 95% confidence intervals on normalised bias $\Delta \hat{\epsilon}$ for various degrees of freedom versus coherence (A). Solid lines are linear regression lines fit to the data of the corresponding colour. Slopes m (B) and intercepts b (C) from the linear regression lines shown in (A) versus degrees of freedom. Solid red lines in (B) and (C) are exponential regression functions with coefficients and accuracy given on the figure.

This allows 95% confidence intervals on corrected spectra $\Delta \hat{S}_c^{\pm}$ to be calculated as

$$\Delta \hat{S}_c^{\pm} = \hat{S}^{\pm} \left((-0.141 \exp(-v/69.699) - 0.015) C + (0.155 \exp(-v/67.014) + 0.022) \right) \quad (4.8)$$

where ν is degrees of freedom. Using the standard propagation of errors, $\Delta\widehat{S}_c^\pm$ is used to calculate 95% confidence intervals on estimated reflection coefficients $\Delta\widehat{R}_c$ as

$$\Delta\widehat{R}_c = \widehat{R}_c 0.5 \left(\sqrt{\left(\frac{\Delta\widehat{S}_c^\pm}{\widehat{S}_c^-}\right)^2 + \left(\frac{\Delta\widehat{S}_c^\pm}{\widehat{S}_c^+}\right)^2} \right) \quad (4.9)$$

4.3.3 Application to simulated data

The correction technique outlined in Equations 4.4-4.9 is demonstrated in Figure 4.5 on simulated data with an incident wave amplitude of 3 m and $R = 0.5$. For clarity, only incident spectra are shown in Figure 4.5A-C. The same bias correction is applied to \widehat{S}^- but percentage deviations of \widehat{S}_c^- from the target value are determined by R , whereas the percentage deviation of \widehat{S}_c^+ is not. With a SNR of 5.0, \widehat{S}^+ is overestimated by an average of 6.56%, whereas the mean absolute error on \widehat{S}_c^+ is 1.78%. \widehat{R}_c is 0.49 which is an improvement on the \widehat{R} estimate of 0.54. Corrected values are similarly accurate for a SNR of 2.5 with a mean error on \widehat{S}_c^+ of 1.83%, compared to 16.11% on \widehat{S}^+ , and a mean \widehat{R}_c of 0.50. A SNR of 1.7 causes \widehat{S}^+ to be overestimated by 31.66%, whilst \widehat{S}_c^+ has a mean error of only 2.44%; a decrease in error magnitude of >90%. Table 4.2 gives a summary of the errors and 95% confidence intervals depicted in Figure 4.5, and for additional SNRs.

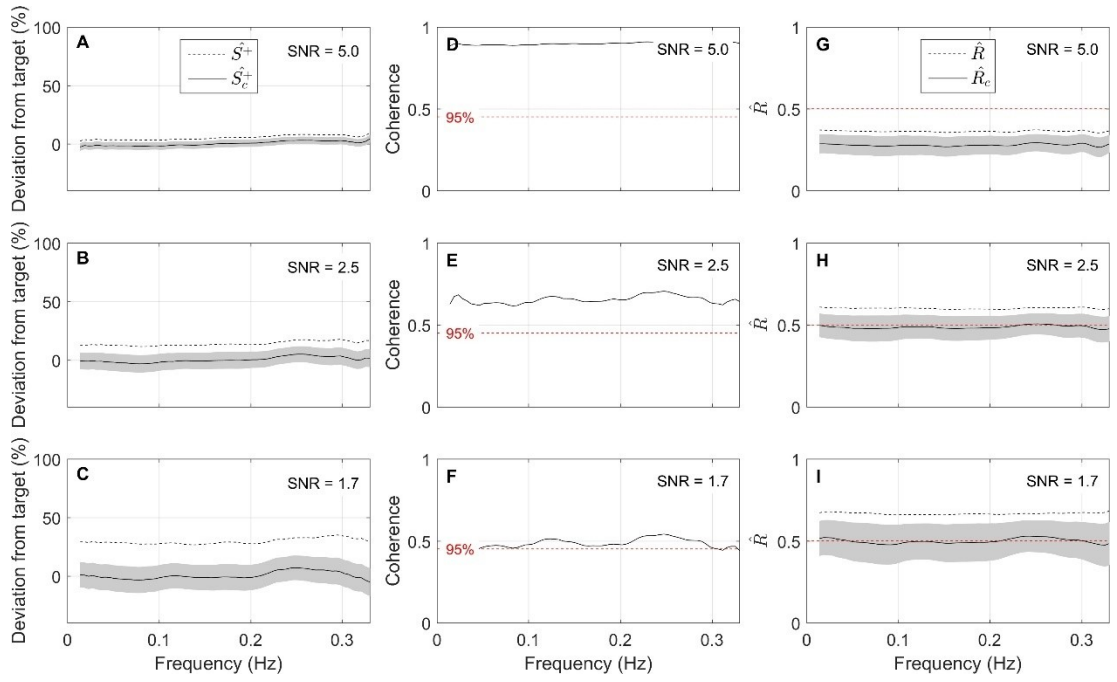


Figure 4.5. Deviation (%) of uncorrected \widehat{S}^+ and corrected \widehat{S}_c^+ incident spectra from the target value S^+ (A-C). Coherence (D-F), and uncorrected \widehat{R} and corrected \widehat{R}_c reflection coefficients (G-I). Shaded areas in (A-C) are 95% confidence intervals on \widehat{S}_c^+ and shaded areas in (G-I) are 95% confidence intervals on \widehat{R}_c . SNRs are 5.0, 2.5, and 1.7 as stated on the figure. Red dashed line in (D-F) is the 95% confidence threshold on coherence of 0.45 for 12 degrees of freedom (Shumway and Stoffer, 2000). Red dashed line in (G-I) is the target reflection coefficient R of 0.5. Wave amplitude is 3 m.

Table 4.2. Summary of mean errors in estimated and corrected incident spectra and reflection coefficients for a wave amplitude of 3 m, known reflection coefficient of 0.5, and SNRs between infinity and 1. Errors in the estimated and corrected incident spectra, and 95% confidence intervals on corrected incident spectra, are given in terms of percentage of the target value S^+ .

SNR	\bar{C}	$\epsilon_{\widehat{S}^+}$ %	$\epsilon_{\widehat{S}_c^+}$ %	95% \widehat{S}_c^+ %	\widehat{R}	\widehat{R}_c	95% \widehat{R}_c
Inf	0.94	3.52	2.06	± 2.27	0.50	0.47	± 0.03
10.0	0.92	4.41	1.93	± 2.61	0.51	0.47	± 0.03
5.0	0.85	6.56	1.78	± 3.64	0.54	0.49	± 0.04
3.3	0.76	10.52	1.48	± 5.14	0.55	0.49	± 0.05
2.5	0.66	16.11	1.83	± 6.91	0.58	0.50	± 0.07
2	0.56	22.67	2.41	± 8.75	0.61	0.50	± 0.09
1.7	0.49	31.66	2.44	± 10.72	0.65	0.50	± 0.11
1.43	0.42	43.06	3.40	± 12.86	0.68	0.49	± 0.13
1.25	0.37	53.32	3.94	± 14.89	0.71	0.49	± 0.16
1.11	0.33	67.93	4.91	± 17.24	0.74	0.48	± 0.19
1	0.29	82.30	6.03	± 19.62	0.76	0.46	± 0.23

SNR = signal-to-noise ratio, \bar{C} = mean coherence, $\epsilon_{\widehat{S}^+}$ = mean percentage error on the estimated incident spectra, $\epsilon_{\widehat{S}_c^+}$ = mean percentage error on the corrected incident spectra, 95% \widehat{S}_c^+ = mean 95% confidence intervals on corrected incident spectra, \widehat{R} = mean estimated reflection coefficient, \widehat{R}_c = mean corrected reflection coefficient, 95% \widehat{R}_c = mean 95% confidence intervals on corrected reflection coefficients.

SNRs less than 1 (not shown) produce biases of $>100\%$ in \widehat{S}^+ , but the accuracy of the correction technique for these simulations remains in a reasonable range, typically less than 15%, albeit with larger confidence intervals. However, for SNRs less than ~ 1.5 , coherence falls below the 95% confidence threshold for 12 degrees of freedom. Nevertheless, degrees of freedom can be increased by frequency smoothing and/or increasing the number of segments when calculating the spectra, which would reduce the 95% confidence threshold for coherence. Therefore, it is beneficial to know that the correction technique is robust at withstanding extreme levels of noise.

4.3.4 Wave angle and directional spreading

The main assumption of array methods for calculating wave reflection is that waves are unidirectional and shore-normal. To investigate the sensitivity of the Gaillard et al. (1980) method, and consequently the noise correction presented in the previous sections, to wave angle, additional simulations were performed using waves approaching from angles up to $\pm 90^\circ$ relative to shore-normal. Results show that the impact of noise observed in the previous sections are unchanged with wave angles up to $\sim 40^\circ$. Wave angles higher than this begin to introduce an additional bias to \widehat{S}^+ and \widehat{S}^- , with a more significant bias impacting \widehat{S}^- . The reflected spectra are affected more since the primary result of oblique waves in the simulations is to increase the travel time of waves between the sensors, with the difference between actual and predicted travel times (i.e., difference between actual and predicted wave phase) increasing as the waves get closer to shore and return seaward. Figure 4.6 shows the normalised bias versus coherence for various wave angles between 0° and 90° . For wave angles of 15° and 30° , the normalised bias closely follows the trend predicted in Section 4.3.1. Whereas at 45° the normalised bias on \widehat{S}^- begins to increase, and at $\geq 60^\circ$ the bias impacting both \widehat{S}^+ and \widehat{S}^- is increased. The increase in bias is less

significant for lower levels of coherence and wave angle does not alter the coherence itself as the noise added to the time series for each SNR remains unchanged.

As a consequence of the results presented in Figure 4.6, an inefficient correction will be applied to the incident and reflected spectra for oblique wave angles $>40^\circ$. For example, for a coherence level of ~ 0.6 , a positive bias equal to 15% of \widehat{S}^+ would be corrected for. However, the actual bias impacting \widehat{S}^+ for wave angles of 45° , 60° , and 75° , is equal to 22%, 47%, and 56%, respectively. Whereas the bias impacting \widehat{S}^- for the same wave angles is equal to 46%, 73%, and 85% of \widehat{S}^+ , respectively. Since \widehat{S}^- experiences a larger bias due to wave angle than \widehat{S}^+ , and this difference remains after any correction, this results in an additional positive bias on \widehat{R} .

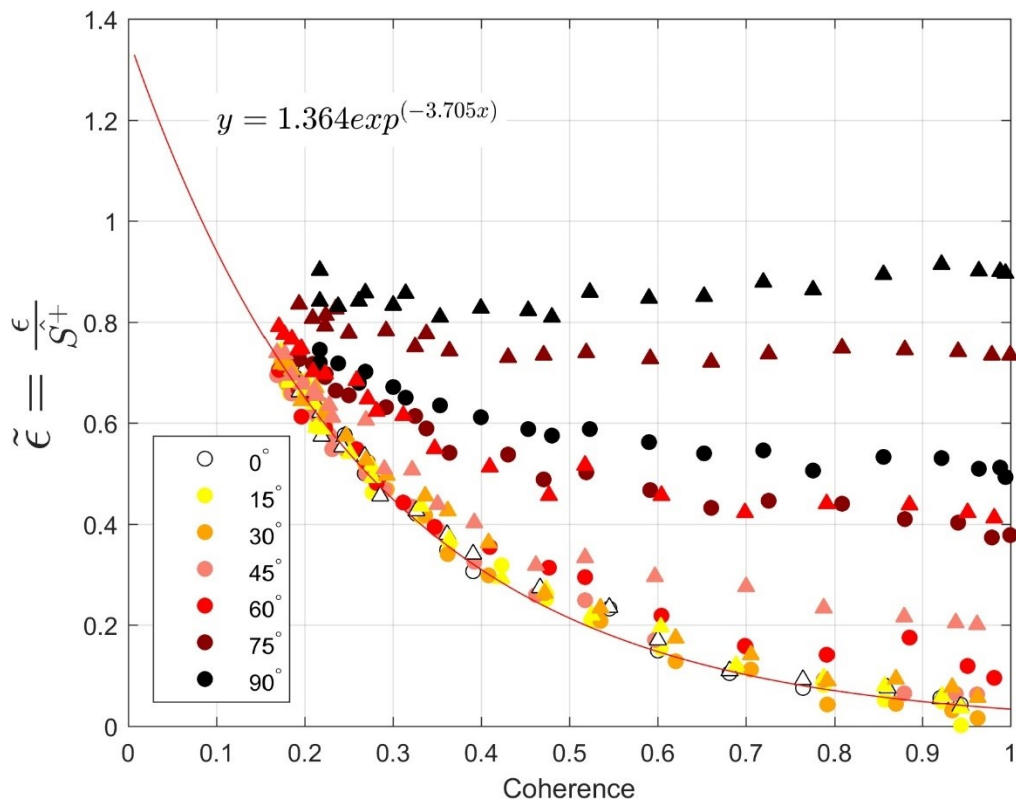


Figure 4.6. Normalised bias $\tilde{\epsilon}$ (ϵ/\widehat{S}^+ , where ϵ is bias) versus coherence for unidirectional waves of various angles, as given by the figure legend. Data have been smoothed providing 984 degrees of freedom. Solid red line is the exponential regression function, with coefficients given on the figure, defined in Figure 4.3 and that forms the basis of the noise correction technique (Equations 4.4-4.7). Circles correspond to the normalised bias on incident spectral estimates and triangles are the normalised bias on reflected spectral estimates.

In a natural wave field, although there is often a dominant angle of wave approach, waves are not entirely unidirectional but are rather distributed over a range of angles. Unlike unidirectional waves, the consequence of directionally spread waves is that the mean coherence between the sensors will decrease without the presence of noise. This could result in an unnecessary correction being applied to the incident and reflected spectra. To examine the impact of a directionally spread wave field on the reflection method and correction technique, simulations were performed using time series of waves with a spectrum of wave directions, both randomly distributed and distributed about shore-normal. In the case of waves distributed about shore-normal, the wave field is determined following a Mitsuyasu et al. (1975) directional distribution.

Figure 4.7 shows the impact of directional spreading on the normalised bias and the correction function. For simulations with waves distributed both $\pm 45^\circ$ and $\pm 90^\circ$ around shore-normal, the bias and coherence is unaffected in all cases. This is to be expected since very little wave energy is at high enough wave angles that were shown to have a detrimental impact in Figure 4.6 (i.e., $>40^\circ$). Coherence is more likely to be reduced when the wave energy is randomly distributed across a range of directions. Although, the bias in randomly distributed waves between $\pm 45^\circ$ follows the expected trend very well, with only a slight reduction in high levels of coherence (>0.8). The only significant impact occurs for randomly distributed waves between $\pm 90^\circ$. In this instance, coherence is reduced significantly as a result of directional spreading, particularly in cases of low noise when coherence should be high. For example, a SNR of 10 yields a coherence level of ~ 0.55 , whereas for unidirectional waves this value is typically >0.9 . As a result, a noise correction equivalent to 17% of \widehat{S}^+ would be applied; much greater than the required correction of only 4%. The consequence of this is a negative bias and an underestimation of R . As with unidirectional oblique waves, the impact of directional spreading is lessened as the level of noise increases (i.e., as the coherence is reduced).

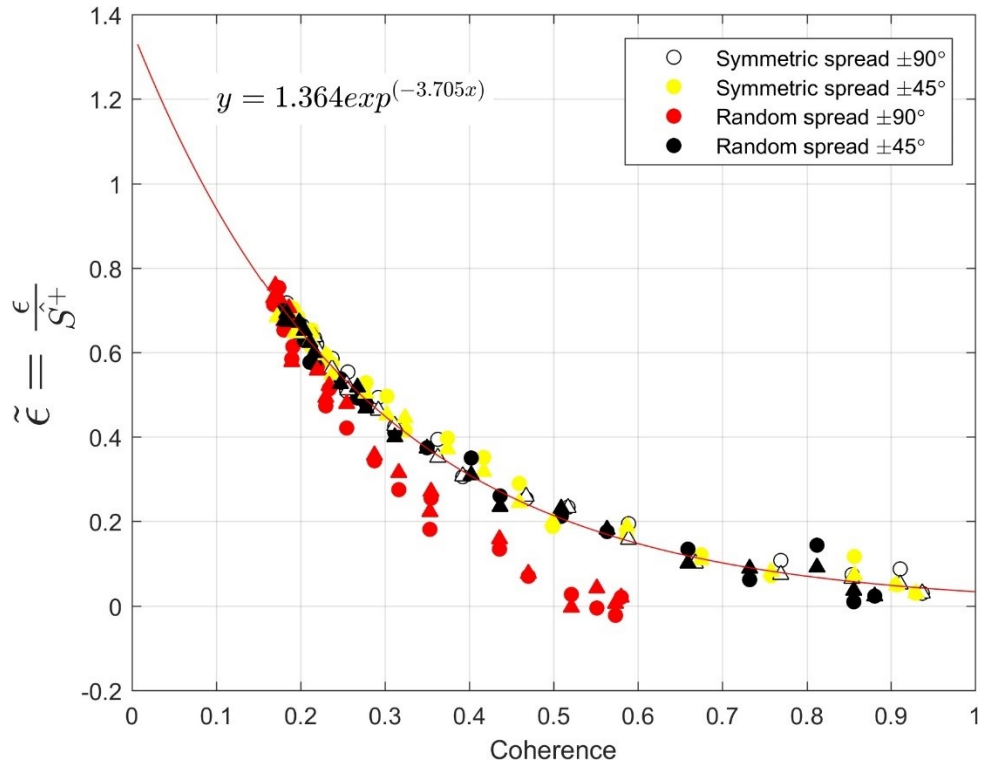


Figure 4.7. Normalised bias $\tilde{\epsilon}$ (ϵ/\widehat{S}^+ , where ϵ is bias) versus coherence for directionally spread waves between $\pm 45^\circ$ and $\pm 90^\circ$, as given by the figure legend. Data have been smoothed providing 984 degrees of freedom. Solid red line is the exponential regression function, with coefficients given on the figure, defined in Figure 4.3 and that forms the basis of the noise correction technique (Equations 4.4-4.7). Circles correspond to the normalised bias on incident spectral estimates and triangles are the normalised bias on reflected spectral estimates.

The results of simulations using oblique and directionally spread waves show that the Gaillard et al. (1980) method for separating incident and reflected waves, and therefore the noise correction technique outlined herein, is fairly robust when waves are not entirely shore-normal. An increase in bias due to oblique waves, and a drop in coherence due to directional spreading, only occurs during quite extreme cases that are unlikely to exist close to shore. This particularly applies to infragravity waves due to their large wavelengths and thus strong refraction properties. However, one should be aware of the potential consequences of oblique and directionally spread waves when decomposing incident and reflected waves and applying the noise correction to field data and ensure that the sensor array is aligned as close to the dominant wave direction as possible.

4.4 Discussion

4.4.1 Application to field data

To illustrate the application of the results to field data, measurements are used from the Perranporth field experiment. The data presented here were collected in the inner surf zone (mean water depth $\bar{h} = 1.5$ m) on 10th November 2014 (tide 6) with an offshore significant wave height H_o of 1.85 m and a spectral peak period T_p of 10.8 s. Spectra were calculated following Section 3.4.1.1 and separated into incident and reflected components using the Gaillard et al. (1980) as outlined in Section 3.4.1.3. Since the array set-up at Perranporth was designed for the study of infragravity waves, only infragravity data are presented here with a low frequency cut-off of 0.01 Hz as with the simulated data.

The general trend shown in Figure 4.8A is of higher magnitudes of \widehat{S}^+ and \widehat{S}^- at lower frequencies than higher frequencies with a spectral peak at $f = 0.016$ Hz; a trend which is preserved in \widehat{S}_c^+ and \widehat{S}_c^- . The largest correction in terms of spectral density occurs at the spectral peak where \widehat{S}_c^+ and \widehat{S}_c^- are reduced by 17.5% and 36.2% of \widehat{S}^+ and \widehat{S}^- , respectively. Larger magnitudes of both \widehat{S}_c^+ and \widehat{S}_c^- in the low frequency portion of the infragravity band yield higher \widehat{R}_c estimates with smaller corrections and confidence intervals than higher frequencies. For example, at $f = 0.020$ Hz, \widehat{R}_c is 0.67 (± 0.06) which is only 0.06 less than \widehat{R} . In contrast, at $f = 0.039$ Hz, the \widehat{R}_c value of 0.26 (± 0.11) is significantly less than the \widehat{R} estimate of 0.39. The mean infragravity \widehat{R} is 0.62 but this is reduced in \widehat{R}_c to 0.53 (± 0.02). Whilst it may not be strictly appropriate to average over the infragravity band given the frequency-dependence shown in the data, it does demonstrate the reduction in confidence intervals as a result of more degrees of freedom.

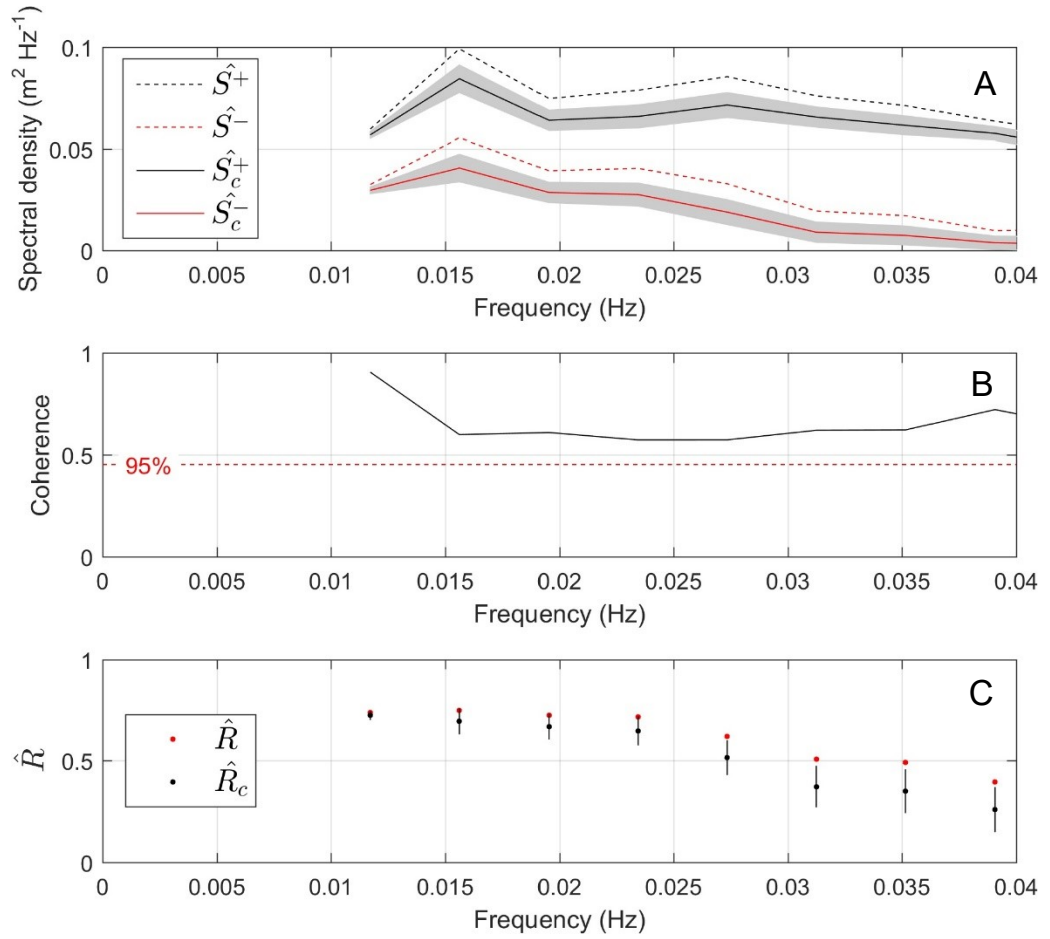


Figure 4.8. Data from the inner surf zone of Perranporth Beach, UK ($H_o = 1.85$ m, $T_p = 10.8$ s). Corrected incident \hat{S}_c^+ and reflected \hat{S}_c^- spectra, and uncorrected incident \hat{S}^+ and reflected \hat{S}^- spectra (A). Coherence (B) and corrected \hat{R}_c and uncorrected \hat{R} estimated reflection coefficients (C). Shaded areas in (A) are 95% confidence intervals on \hat{S}_c^+ and \hat{S}_c^- and error bars in (C) are 95% confidence intervals on \hat{R}_c . Red dashed line in (B) is the 95% confidence threshold on coherence of 0.45 for 12 degrees of freedom (Shumway and Stoffer, 2000).

The frequency-dependence of infragravity wave reflection, with high levels of reflection limited to low frequencies, is well-documented in the literature (e.g., De Bakker et al., 2014; Guedes et al., 2013). The results presented here suggest that, in failing to correct for bias, \hat{R} values at high infragravity frequencies where wave reflection is low, and indeed at short wave frequencies where reflection tends to be even more minimal, can be overestimated by more than 50%. This is likely to have impacted wave reflection estimates reported previously in the literature where wave sensor arrays have been used.

In the following results chapters, the noise correction technique will ultimately to be used to correct for noise in infragravity energy fluxes and energy (i.e., squared) reflection coefficients. Corrected incident \widehat{F}_c^+ and reflected \widehat{F}_c^- energy fluxes are calculated as

$$\widehat{F}_c^\pm = \widehat{S}_c^\pm \sqrt{gh} \quad 4.10$$

and corrected energy reflection coefficients $\Delta \widehat{R}_c^2$ as

$$\widehat{R}_c^2 = \frac{\widehat{S}_c^-}{\widehat{S}_c^+} \quad 4.11$$

The standard propagation of errors is used to estimate 95% confidence intervals on energy fluxes $\Delta \widehat{F}_c^\pm$ and energy reflection coefficients $\Delta \widehat{R}_c^2$ as

$$\Delta \widehat{F}_c^\pm = \Delta \widehat{S}_c^\pm \sqrt{gh} \quad 4.12$$

and

$$\Delta \widehat{R}_c^2 = \widehat{R}_c^2 \sqrt{\left(\frac{\Delta \widehat{S}_c^-}{\widehat{S}_c^-}\right)^2 + \left(\frac{\Delta \widehat{S}_c^+}{\widehat{S}_c^+}\right)^2} \quad 4.13$$

Figure 4.9 shows the cross-shore variation of corrected and uncorrected bulk infragravity energy fluxes and energy reflection coefficients. The uncorrected incident energy flux shows a brief increase at $h > 3.5$ m before decreasing towards the shoreline, whereas the reflected energy flux remains more constant without a clear increase or decrease. This trend is preserved in the corrected energy fluxes, although values are lower by an average of $0.003 \text{ m}^3 \text{ s}^{-1}$. Maximum and minimum corrections are equivalent to 20% and 6% of \widehat{F}_c^+ , respectively, and 67% and 22% of \widehat{F}_c^- , respectively. Corrected energy reflection coefficients are 0.05-0.15 less than the uncorrected values, with the correction typically becoming larger towards the shore where energy fluxes are lower. With the increase in

degrees of freedom from averaging over the infragravity frequency band, confidence limits on the corrected energy fluxes and energy reflection coefficients are very low at $\pm 0.0002 \text{ m}^3 \text{ s}^{-1}$ and ± 0.01 , respectively, and are thus not shown in Figure 4.9. This also applies to the results presented in Chapters 5 and 6.

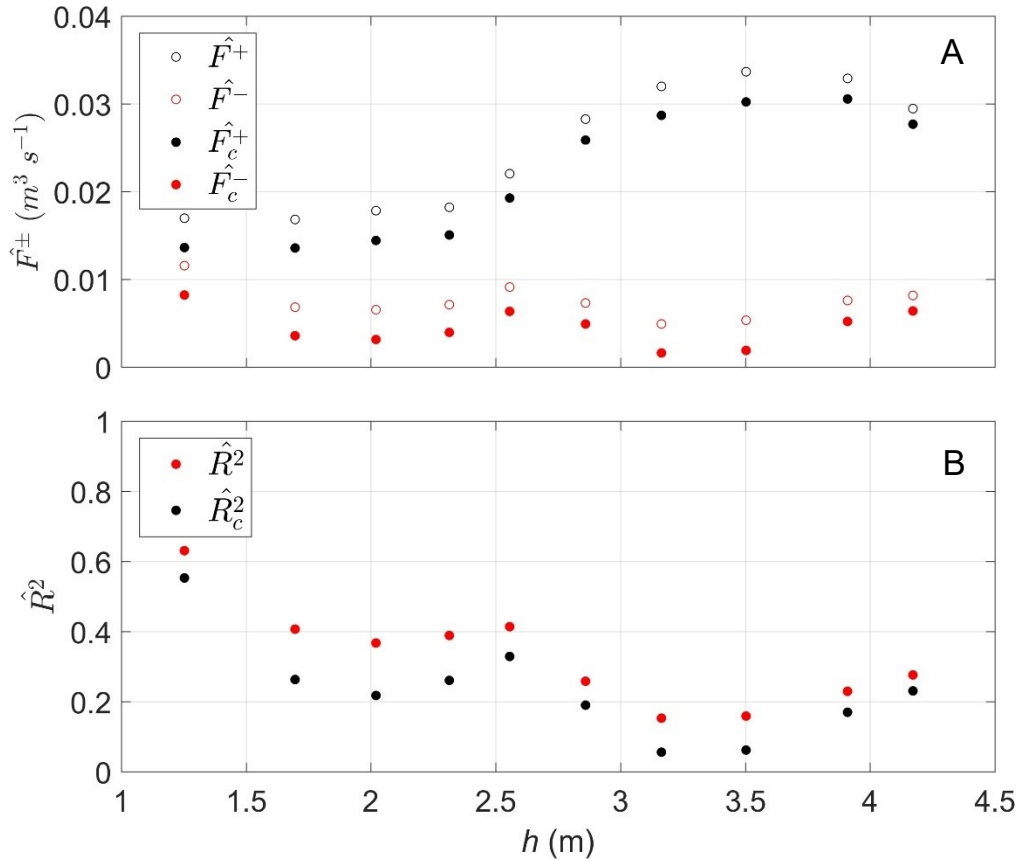


Figure 4.9. Data from the inner surf zone of Perranporth Beach, UK ($H_o = 1.85 \text{ m}$, $T_p = 10.8 \text{ s}$). Corrected incident \hat{F}_c^+ and reflected \hat{F}_c^- infragravity energy flux, and uncorrected incident \hat{F}^+ and reflected \hat{F}^- infragravity energy flux (A). Corrected \hat{R}_c^2 and uncorrected \hat{R}^2 infragravity energy (i.e., squared) reflection coefficients (B).

4.5 Conclusion

An existing two-dimensional method for separating incident and reflected wave spectra using an array of wave sensors is investigated for its sensitivity to random noise. Linear wave theory is used to generate simulated time series of water surface elevation at three cross-shore locations with varying wave amplitudes, known reflection coefficients, and signal-to-noise ratios. Both the incident and reflected spectra are shown to be positively

biased by noise and in turn this causes reflection coefficients to be overestimated. The magnitude of the bias is found to be dependent on wave amplitude, but not on the true reflection coefficient. Utilizing the systematic change in coherence with noise, a relatively simple and easy to apply method to correct for the observed bias is developed. This correction technique can be applied across all frequencies and is considerably accurate with residual error on corrected incident spectra estimates typically in the region of 2-3% for significant coherence levels; an improvement of over 90% for low signal-to-noise ratios. Applying the correction to field data implies that reflection coefficients can be overestimated by at least 50%. These findings imply that where similar array methods have been used in the literature, results may be significantly biased and the extent to which infragravity waves dissipate, particularly at the higher frequency end of the infragravity band, may be underestimated. Consequently, if accurate estimates of incident and reflected spectra and corresponding reflection coefficients are required, then potential signal noise must be acknowledged and accounted for.

To demonstrate that the method used herein to derive the correction function can be applied to other wave reflection algorithms with equal success, a correction technique for the method of Van Dongeren et al. (2007) is developed and validated in Appendix A.

4.6 List of chapter specific symbols

To aid in the interpretation of the results presented in this chapter, below is a list of the main symbol combinations used in the development of the correction function. Note that symbols listed below that include S also apply to F , and those including R also apply to R^2 .

S^\pm Known (i.e., target) auto-spectra

\widehat{S}^\pm Predicted auto-spectra

\widehat{S}_c^\pm	Predicted auto-spectra with correction
$\Delta\widehat{S}_c^\pm$	95% confidence interval on \widehat{S}_c^\pm
R	Known (i.e., target) amplitude reflection coefficient
\widehat{R}	Predicted amplitude reflection coefficient
\widehat{R}_c	Predicted amplitude reflection coefficient with correction
$\Delta\widehat{R}_c$	95% confidence interval on \widehat{R}_c
ϵ	Known (i.e., target) spectral bias
$\tilde{\epsilon}$	Normalised spectral bias
$\hat{\epsilon}$	Predicted spectral bias

Note: all incident and reflected spectra, and subsequent energy fluxes, wave heights, and reflection coefficients, presented in the remainder of this thesis have undergone the noise correction outlined in the present chapter but are shown in their original notation (see List of symbols and abbreviations) and without the additional subscripts and accents used here.

Chapter 5

Infragravity waves during swell and wind-sea (Perranporth experiment)²

The objective of this chapter is to investigate the dependence of infragravity waves on offshore forcing parameters, with particular attention given to the magnitude and spatial variation of the infragravity energy flux in the surf zone during contrasting swell and wind-wave conditions. In doing so, this contribution extends the work of other field studies that have largely been undertaken on low fetch coastlines and/or during low-moderate energy conditions.

An overview of the offshore wave conditions during the Perranporth field experiment are presented first, followed by an investigation into the relationship between various offshore forcing parameters and nearshore infragravity wave height. This is investigated further through the detailed analysis of three individual tides with contrasting forcing conditions to highlight differences between infragravity propagation, dissipation and reflection. Finally, possible dissipation mechanisms are alluded to and the results are put into context with previous studies.

5.1 Experimental conditions

5.1.1 Offshore wave conditions

A wide range of offshore wave conditions were present during the study period (Figure 5.1). Significant wave height H_o ranged from 0.38 to 3.88 m with a mean value of 1.84 m. There were 5 occasions during the study period during which H_o exceeded 2 m for 12

² *Published as:*

Inch, K., Davidson, M., Masselink, G., Russell, P. 2015. Propagation and dissipation of infragravity waves on a dissipative beach with energetic wave forcing. *Proceedings of Coastal Sediments 2015*, World Scientific, San Diego, USA.

Inch, K., Davidson, M., Masselink, G., Russell, P. 2017. Observations of nearshore infragravity wave dynamics under high energy swell and wind-wave conditions. *Continental Shelf Research*, 138, 19-31.

hours or more, and 2 periods of 12 hours during which H_o remained below 0.5 m. The spectral peak period T_p was also broadly ranging and varied between 6 and 20 s with a mean value of 12.5 s. The experiment spanned a spring-spring tidal cycle with spring and neap tidal ranges of around 6.7 m and 2.2 m, respectively. Wave direction at the buoy location was tidally modulated and typically ranged between 20° south and 15° north of shore-normal (mean = 4° south).

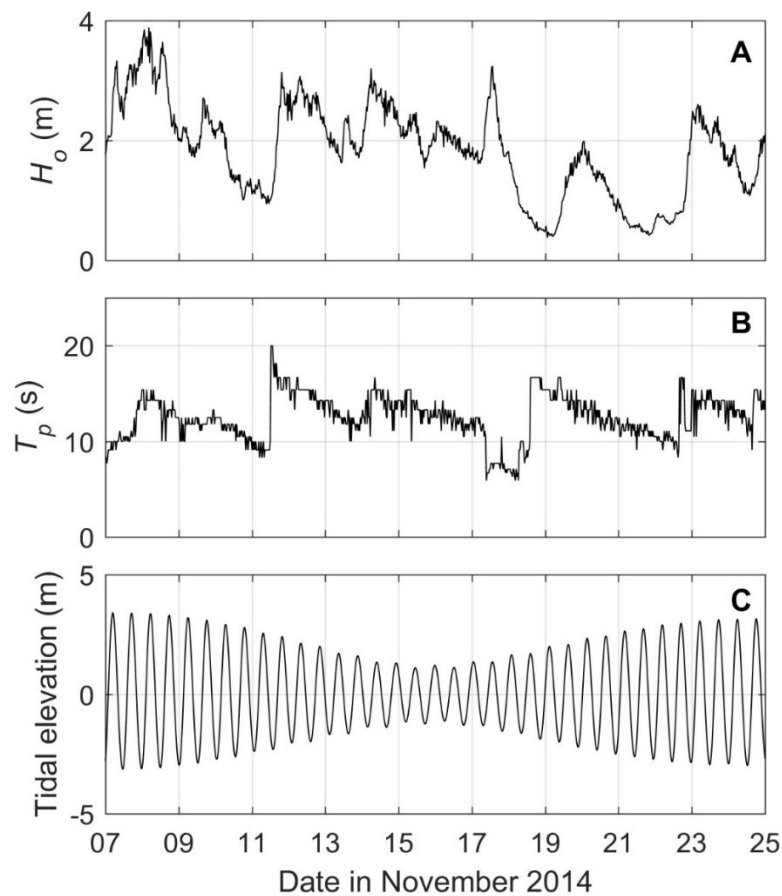


Figure 5.1. Offshore wave conditions during the study period, measured by a Datawell Directional Waverider buoy at a depth of approximately -17 m ODN. Significant wave height H_o (A), spectral peak period T_p (B), and tidal elevation relative to mean sea level (C).

5.1.2 Alongshore hydrodynamics

While the focal point of this thesis is cross-shore infragravity wave dynamics, it is prudent to assess the contribution of alongshore motions to the infragravity wave field to ensure that the results are not influenced by the presence of edge and/or shear waves.

Furthermore, the reflection analysis assumes infragravity waves of shore-normal incidence. Alongshore infragravity motions cannot be investigated using only pressure measurements in a cross-shore alignment, but this can be achieved through the analysis of the available co-located pressure and velocity data.

The ratio between the alongshore infragravity velocity variance and the cross-shore infragravity velocity variance is always <0.5 during the 10 tides in which the PUV rig was deployed, with an average (\pm one standard deviation) of 0.33 ± 0.07 (Figure 5.2A). As a second check, shear wave contributions to the total infragravity velocity variance, calculated following Lippmann et al. (1999), are $25\% \pm 11\%$ (Figure 5.2B). These values are well below the thresholds defined by Henderson et al. (2006) and De Bakker et al. (2014).

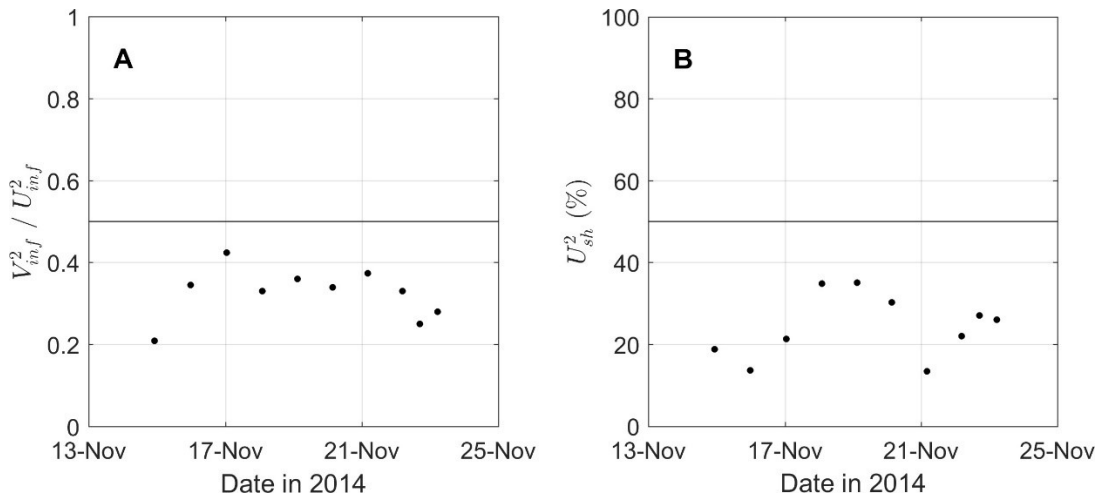


Figure 5.2. Ratio between the alongshore V_{inf}^2 and cross-shore U_{inf}^2 velocity variance in the infragravity band (A), and the percentage of shear wave contributions to the total infragravity velocity variance U_{sh}^2 (B), for the 10 tides during which the PUV rig was deployed in the Perranporth field experiment. Horizontal lines in (A) and (B) indicate 0.5 and 50%, respectively. Shear wave contributions were calculated following Lippmann et al. (1999).

These findings regarding alongshore motions are supported by those of Miles and Thorpe (2015) who observed tidally modulated mean alongshore currents at Perranporth which were close to zero at high tide. Austin et al. (2010) also reports that refraction due to the

local bathymetry between the offshore wave buoy and the shoreline creates near-normal incidence, resulting in weak or non-existent net longshore currents.

5.1.3 Short waves in the surf zone

The average breaker coefficient γ_b , defined as H_{SS}/h at the onset of short wave breaking, was 0.42 for the high tides that included sensors measuring outside of the surf zone (11 tides). These tides were selected from visual observations of the data, with the shoaling region being identified as a clear shoreward increase in H_{SS} , characteristic of shoaling waves outside the surf zone. Using γ_b , data are given a normalised surf zone position h/h_b , where h_b is the water depth at the short wave break point defined as $h_b = H_b/\gamma_b$, where H_b is the breaking wave height. H_b is calculated by shoaling H_o shoreward from the wave buoy using linear wave theory to the depth at which the shoaled wave height $\approx \gamma_b h$. A total of 82.4% of the data analysed corresponded to h/h_b values <1 , indicating that the majority of data were collected from within the surf zone. Furthermore, during particularly small wave conditions and/or spring tides, the most seaward sensor obtained measurements 2-3 surf zone widths from the shoreline. While γ_b corresponds to the breaking of the largest short waves, in the saturated inner surf zone, where all short waves are broken and H_{SS} is depth limited, the ratio of H_{SS} to h (often referred to as the breaker index γ) rises to a fairly constant value of ~ 0.52 .

5.2 Results

5.2.1 Basic hydrodynamic statistics

A summary of the hydrodynamic statistics recorded by the pressure sensors during the study period is given in Table 5.1. The maximum H_{inf} measured was 1.02 m at the most shoreward sensor ($h = 0.52$ m) on 8th November with a H_o of 3.51 m and a T_p of 13.8 s.

This also corresponds to the time and location at which infragravity energy was most dominant, accounting for 92.9% of the total wave variance. It was during this tide that the maximum values of H^+ and H^- were also measured, with a maximum H^+ of 0.70 m measured at $h = 3.25$ m, and a maximum H^- of 0.48 m occurring closer to shore at $h = 1.14$ m. In contrast, the minimum H_{inf} of 0.05 m was measured at the most seaward sensor ($h = 4.36$ m) on 22nd November when $H_o = 0.65$ m and $T_p = 9.3$ s. Here, seaward of the surf zone, infragravity variance accounted for only 0.06% of the total wave variance and it was during this tide that the lowest H^+ value of 0.04 m was measured at $h = 4.21$ m. With the breaking of sea-swell waves, the ratio of infragravity to sea-swell variance increased shoreward and averaged 2.52 at the shallowest sensor where infragravity variance exceeded sea-swell variance for 69.7% of the 33 high tides. Infragravity amplification, the ratio of infragravity wave height at the shallowest sensor relative to the deepest sensor, ranged from 0.84 to 3.30 with the strongest amplifications typically occurring when H_o and T_p were lower.

Table 5.1. Overview of basic hydrodynamic statistics (recorded during all tides and at all locations).

	h (m)	H_{SS} (m)	H_{inf} (m)	H^+ (m)	H^- (m)	S_{inf}/S_{SS}	A_{inf}
Mean	2.09	1.07	0.41	0.34	0.15	0.45	1.50
Standard Deviation	1.13	0.56	0.20	0.17	0.09	1.16	0.62
Minimum	0.20	0.25	0.05	0.04	0.01	0.01	0.84
Maximum	4.83	3.03	1.02	0.70	0.48	13.08	3.30

h = water depth, H_{SS} = sea-swell wave height, H_{inf} = total infragravity wave height, H^+ = incident infragravity wave height, H^- = reflected infragravity wave height, S_{inf}/S_{SS} = ratio of infragravity to sea-swell variance, A_{inf} = infragravity amplification.

5.2.2 Generation and forcing

With the range of forcing conditions experienced during the study period, as well as the changing tidal range, the instruments were measuring at different locations relative to the surf zone during each tide. In order to have a consistent value representing the infragravity wave height with which to relate to the offshore forcing conditions, here H_{inf} is averaged

over the range $0 < h/h_b < 0.33$ (i.e., inner one third of the surf zone) for each tide. This corresponds to between 2 and 7 measurement locations.

Figure 5.3A shows a strong positive correlation between H_{inf} and H_o with the coefficient of determination r^2 associated with the best-fit linear line revealing that 79% of the variability in H_{inf} is determined by H_o . Replacing H_o with H_{swell} (offshore wave height in the frequency band $0.04 < f < 0.14$ Hz) removes the influence of short period sea waves and yields an improved r^2 of 0.89 (Figure 5.3B). Conversely, H_{sea} (offshore wave height in the frequency band $0.14 < f < 0.33$ Hz) provides a much weaker prediction of H_{inf} with an r^2 of 0.28 (not shown). The transition from H_{swell} to H_{sea} at $f = 0.14$ Hz was chosen following Elgar et al. (1992) and Ruessink (1998a).

Using $(H_o L_o)^{1/2}$ as the independent variable in the linear regression to account for wave period (following Stockdon et al., 2006; Senechal et al., 2011; Fiedler et al., 2015) reduces the scatter seen in Figure 5.3A with an r^2 of 0.89 (not shown); the same accuracy as using H_{swell} . However, the strongest prediction of H_{inf} is achieved by using a parameter reflecting a linear wave theory estimate of the deep water wave power, $H_o^2 T_p$ (Figure 5.3C) and this yields an r^2 of 0.93. It could be argued that this latter parameter has a better physical justification than $(H_o L_o)^{1/2}$ as it is proportional to the offshore energy flux.

Infragravity saturation, where H_{inf} ceases to increase despite further increases in offshore forcing, is not observed in any of the linear regression models. A summary of the regression coefficients, coefficients of determination, and RMS errors from fitting H_{inf} with various offshore parameters is given in Table 5.2.

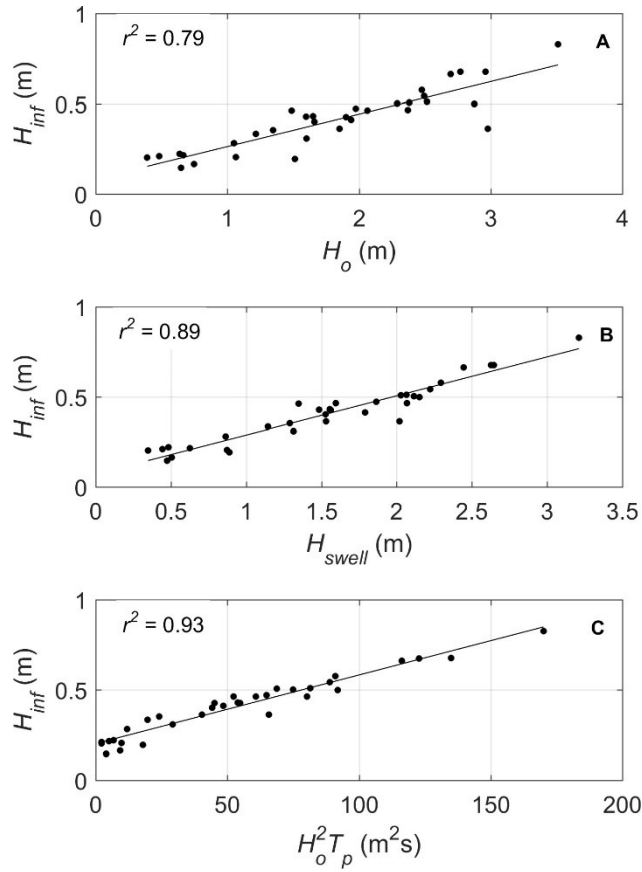


Figure 5.3. Infragravity wave height H_{inf} for $0 < h/h_b < 0.33$ versus offshore significant wave height H_o (A), offshore significant wave height in the swell frequency band H_{swell} (B), and $H_o^2 T_p$ (C). Black lines are best-fit linear regression lines with coefficients of determination given on the figure and regression coefficients given in Table 5.2.

Table 5.2. Regression parameters relating to linear fits between H_{inf} and various offshore forcing parameters. All coefficients of determination r^2 are significant at the 95% level.

Quantity modelled	Model input	Slope m	Intercept b	Coefficient of determination r^2	RMSE (cm)
H_{inf}	H_o	0.18 (± 0.04)	0.08	0.79	6.7
H_{inf}	H_{swell}	0.22 (± 0.03)	0.07	0.89	4.5
H_{inf}	H_{sea}	0.19 (± 0.11)	0.25	0.28	14.4
H_{inf}	T_p	0.03 (± 0.02)	0.03	0.19	15.3
H_{inf}	$(H_o L_o)^{1/2}$	0.02 (± 0.003)	0.00	0.89	4.6
H_{inf}	$H_o^2 T_p$	0.004 (± 0.0006)	0.20	0.93	4.2

H_{inf} = infragravity wave height where $0 < h/h_b < 0.33$, H_o = offshore significant wave height, H_{swell} = offshore significant wave height in the frequency range 0.04-0.14 Hz, H_{sea} = offshore significant wave height in the frequency range 0.14-0.33 Hz, T_p = offshore peak wave period, L_o = deep water wavelength corresponding to T_p .

A stronger infragravity response to swell than sea has been reported by others (e.g., Elgar et al., 1992; Okihira et al., 1992) and is consistent with bound wave theory (Longuet-Higgins and Stewart, 1962; Hasselmann, 1962), given the dissipative nature of the beach. This is investigated further by performing a cross-correlation between the wave group envelope at the most seaward sensor and the infragravity time series at all locations for the 11 tides during which data were collected outside of the surf zone (i.e., $h/h_b > 1$). If the dominant source of infragravity energy is bound waves, then the cross-correlation coefficient at zero time lag r^0 should go to -1 offshore of the surf zone because the wave group envelope and the bound infragravity waves are 180° out of phase. The 95% confidence intervals on cross-correlation coefficients, calculated as outlined in Garrett and Toulany (1981), are around ± 0.08 .

All of the tides show clear evidence of bound waves at the most seaward sensor with values of r^0 significantly less than 0. However, the strongest negative correlations of between -0.31 and -0.49 do not occur at zero time lag but at a lag of between 1.8 and 7.0 s (mean = 4.1 s). This implies that the trough of the bound infragravity wave is lagging behind the crest of the wave group envelope.

An example of the cross-correlations between the wave group envelope at the most seaward sensor and the infragravity time series at every shoreward location is shown in Figure 5.4 for tide 7 ($H_o = 1.05$ m, $T_p = 10.8$ s). At the most seaward location, the trough of the bound infragravity wave is lagged 3 s behind the crest of the wave group envelope and propagates shoreward at the group speed C_g , which in the present dataset $\approx \sqrt{gh}$, as shown by the bar of strong negative (blue) correlation. The correlation weakens very close to shore and the bar of negative correlation associated with the reflected infragravity wave, which agrees well with the shallow water wave speed \sqrt{gh} , is weaker than that of the incident infragravity wave. This is most likely due to strong dissipation, as shown in the

following section, but could also be related to the presence of a breakpoint forced infragravity wave that is positively correlated to the wave group envelope. However, a breakpoint forced infragravity wave should also generate a negatively correlated set-down wave radiating seaward of the surf zone, which is not clearly shown. The pattern shown in Figure 5.4 is consistent across the 11 tides with data collected seaward of the surf zone.

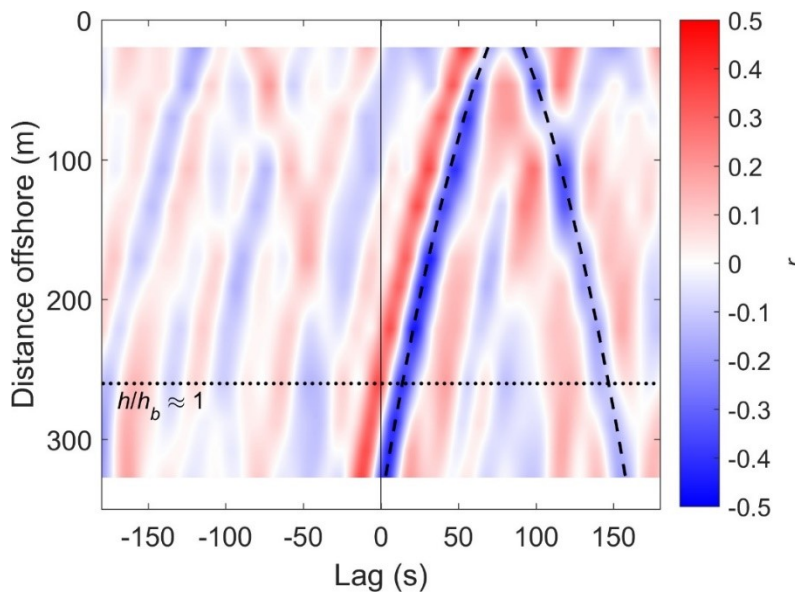


Figure 5.4. Cross-correlation between the wave group envelope at the most seaward sensor and the infragravity wave time series at all locations during tide 7 ($H_o = 1.05$ m, $T_p = 10.8$ s). The dashed black line is the predicted time lag for an incident and reflected wave propagating at \sqrt{gh} . The solid black line represents a time lag of 0 s and the horizontal dotted line shows the location of the short wave breakpoint at $h/h_b \approx 1$. Red indicates positive correlations and blue indicate negative correlations.

5.2.3 Propagation, dissipation, and reflection

To investigate the spatial trend in infragravity wave propagation and dissipation across all tides, Figure 5.5A shows F^+ normalised by the mean value $\overline{F^+}$ for each tide as a function of h/h_b . As can be seen, normalised values of F^+ outside of the surf zone generally show an increasing trend towards the short wave breakpoint suggesting that infragravity waves are gaining energy. This increase continues into the surf zone until $h/h_b \approx 0.7$ where a clear, rapid decrease towards the shoreline begins. This decrease,

consistent with infragravity dissipation, appears to accelerate slightly when h/h_b becomes less than ~ 0.3 . Figure 5.5B shows the correlation coefficient at zero time lag between the wave group envelope and the infragravity time series at all locations during all tides. It is clear that the switch from infragravity growth to dissipation at $h/h_b \approx 0.7$ coincides with a change in r^0 from negative to positive. The shift away from a negative correlation implies that the bound infragravity waves are being released as the short waves break and lose their group structure. Positive correlations in the inner surf zone imply that the largest short waves are propagating on the crests of the infragravity waves whilst the smaller short waves propagate in the infragravity wave troughs. This occurs as the infragravity wave crests increase the local water depth allowing larger short waves to prevail and restore some groupiness, though now in phase with the infragravity wave. The grouped nature of the short waves can be investigated by calculating the groupiness factor. Figure 5.5C shows a decrease in the groupiness factor starting at the short wave breakpoint and reaching a minimum in the middle of the surf zone, before increasing close to shore to levels similar to those outside of the surf zone.

This modulation of short wave height by infragravity waves is further demonstrated in Figure 5.6 which displays example sea-swell time series from three normalised surf zone locations during tide 27 ($H_o = 0.67$ m, $T_p = 11.4$ s). Outside of the surf zone at $h/h_b = 1.24$ (Figure 5.6A) groups of short waves occur predominantly where there are infragravity wave troughs (cool colours) such as at 60 s, 170 s, and 270 s. At $h/h_b = 0.68$ waves are in the transition zone where groupiness is reduced and the correlation between the wave group envelope and the infragravity time series is neither predominantly positive nor negative. Here the short wave time series displays no clear groups or relationship with the infragravity waves (Figure 5.6B). However, the time series at $h/h_b = 0.18$ shows the presence of wave groups, though now consisting of fewer waves, and these groups correspond to infragravity wave crests (warm colours) such as at 75 s, 200 s, and 340 s

(Figure 5.6C). A detailed study of short wave modulation by infragravity waves using laboratory data is provided by Tissier et al. (2015).

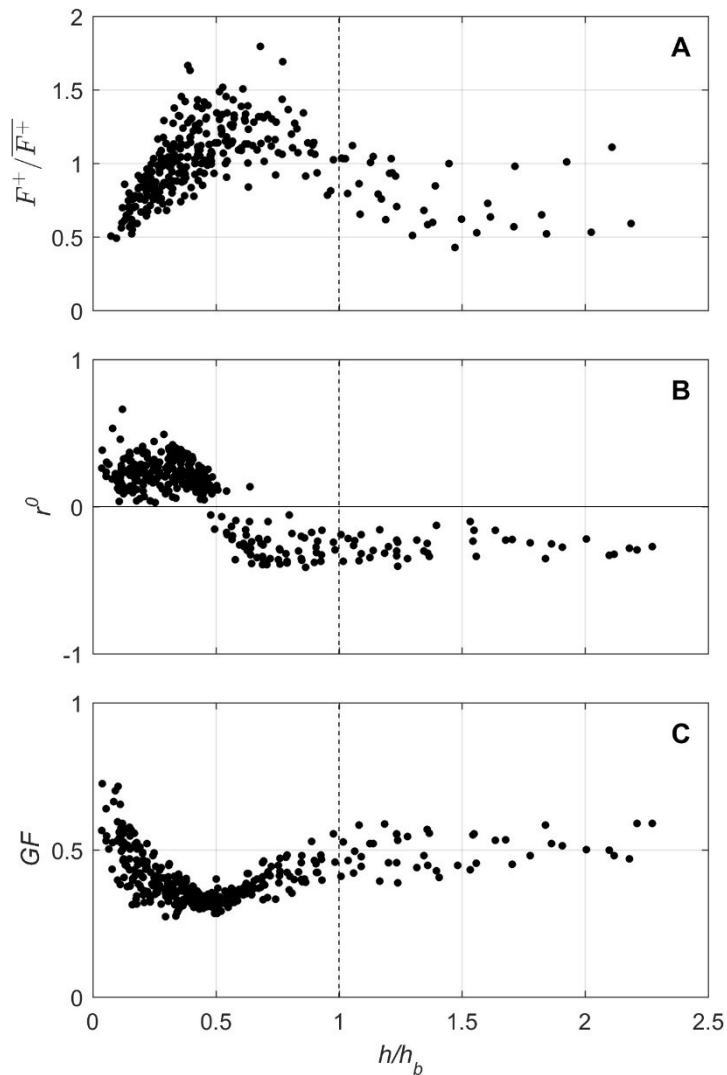


Figure 5.5. Bulk incident infragravity energy flux (F^+) normalised by the mean value ($\overline{F^+}$) for each tide (A), correlation coefficient at zero time lag r^0 between the wave group envelope and the infragravity time series (B), and groupiness factor GF (C), versus normalised surf zone width h/h_b for all locations during all tides. Dashed vertical lines indicate the seaward limit of the surf zone at $h/h_b = 1$. Only r^0 values significant at the 95% level are shown in (B).

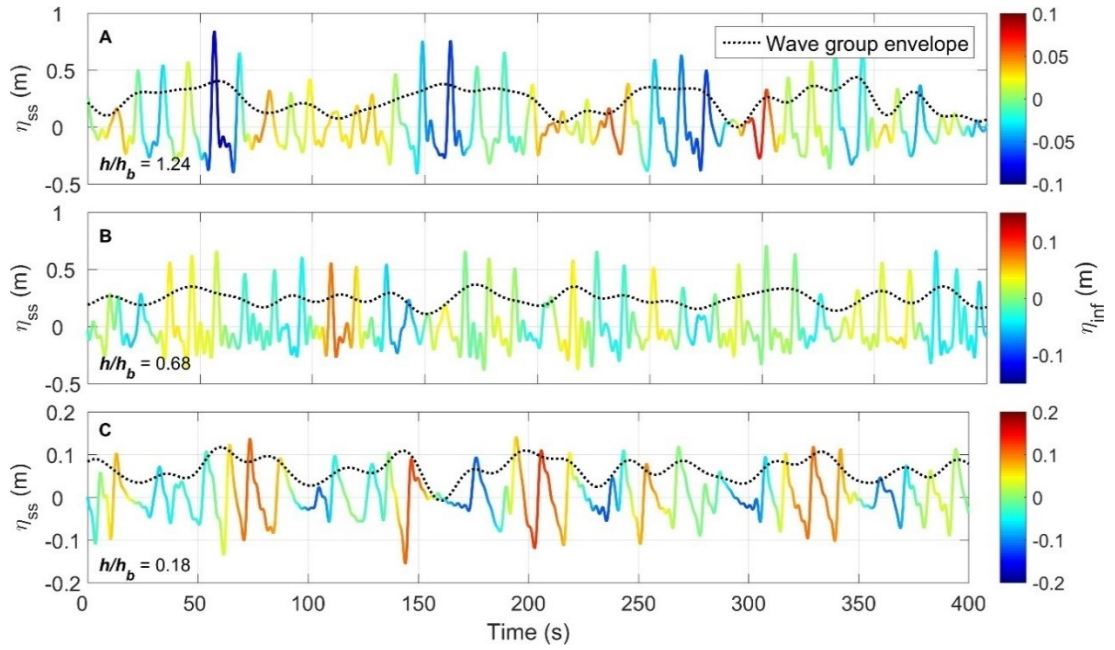


Figure 5.6. Example sea-swell time series η_{SS} from tide 27 ($H_o = 0.67$ m, $T_p = 11.4$ s) at three normalised surf zone h/h_b locations; 1.24 (A), 0.68 (B), and 0.18 (C). The dotted black line is the wave group envelope. Colour represents the infragravity water surface elevation η_{inf} with warm colours indicating infragravity wave crests and cool colours indicating infragravity wave troughs. Note the different axis scales.

To further examine the propagation and transformation of infragravity waves and the influence of offshore forcing, three individual tides are investigated in detail. The level of offshore forcing, characterised by $H_o^2 T_p$, varies considerably between the tides. This variability is not due to differences in H_o , which is ~ 3 m during each tide, but rather by variations in T_p . The purpose of selecting these particular tides is to accentuate the effect that offshore wave period has on infragravity wave characteristics. A summary of the environmental parameters for each tide is given in Table 5.3.

Table 5.3. Summary of environmental parameters during tides 10, 1, and 20.

Tide No.	H_o (m)	T_p (s)	$H_o^2 T_p$	TR (m)	H_b (m)	H_{inf} (m)	R^2	β
10	2.96	15.4	134.7	4.40	3.27	0.87	0.32	0.0319
1	2.88	11.1	92.3	6.68	3.12	0.63	0.43	0.0447
20	2.99	7.4	66.2	3.05	3.04	0.29	0.28	0.0188

H_o = offshore significant wave height, T_p = offshore peak wave period, TR = tidal range, H_b = breaking wave height, H_{inf} = infragravity significant wave height at the shoreline, R^2 = bulk infragravity reflection coefficient the shoreline, β = swash zone beach slope. Note the similarity in H_o for each tide but widely varying T_p .

To illustrate the difference in offshore forcing between the three tides, and its influence on infragravity energy levels in the surf zone, Figure 5.7 shows the offshore wave spectra at the wave buoy and in the surf zone at $h \approx 2$ m. The offshore wave spectrum for tide 10 shows a large, narrow-banded peak typical of long period swell, with little energy at frequencies >0.1 Hz. This develops into a large, narrow infragravity peak in the surf zone at $f = 0.0117$ Hz (85 s) which dominates the surf zone spectrum. In contrast, the peak in the offshore wave spectrum for tide 20 straddles the boundary between swell and sea frequencies, with very little energy at frequencies <0.1 Hz. The surf zone spectrum for tide 20 shows very low levels of infragravity energy and, of the three tides, it is the only one with swell and sea peaks exceeding those in the infragravity band. The offshore spectrum for tide 1 sits somewhat in the middle of tides 10 and 20, with its primary peak in the swell band at $f = 0.0900$ Hz (11.1 s) and a smaller peak in the sea band at $f = 0.1450$ Hz (6.9 s). This produces two infragravity peaks in the surf zone spectrum at $f = 0.0078$ Hz (128.2 s) and 0.0234 Hz (42.7 s); albeit these peaks are smaller than the infragravity peak in tide 10 by more than a factor of 3.

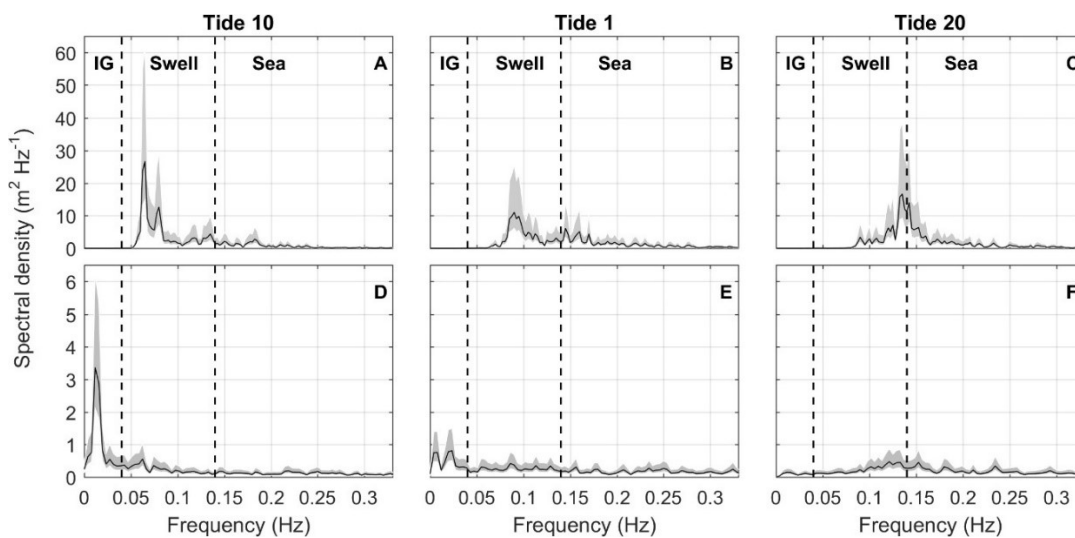


Figure 5.7. Offshore wave spectra at the wave buoy (A-C) and surf zone wave spectra at $h \approx 2$ m (D-F), for tides 10 (left panels), 1 (middle panels), and 20 (right panels). Shaded areas are 95% confidence intervals.

With H_o values of almost 3 m, the entire instrument array was situated within the surf zone during all three tides, as evident by the constant linear decrease in H_{ss} typical of a saturated surf zone (Figure 5.8A-C). Maximum H_{inf} values always occur at the shallowest sensor and reach 0.87 m during tide 10 which had the highest T_p of 15.4 s. This is a factor of 3 times larger than tide 20 during which T_p was only 7.4 s. Figure 5.8D-F shows evidence of infragravity wave dissipation during all three tides with F^+ exceeding F^- at all locations, and F^+ decreasing shoreward with maximum values at the deepest sensor and minimum values at the shallowest sensor. The magnitude of F^+ is considerably higher during the high period tides. For example, relative to tide 20, F^+ at $h \approx 3$ m is larger by a factor of 3 during tide 1, and by a factor of 5 during tide 10. Furthermore, maximum values of F^+ during tide 20 are less than the minimum values during tides 10 and 1.

Dissipation rates of the incident and reflected infragravity waves are shown in Figure 5.8G-I. Values of D^+ tend to increase shoreward with maximum values occurring between the shallowest sensors for all tides. However, D^+ is considerably larger when there is more energetic offshore forcing. For example, spatially averaged D^+ for $h < 3$ m is higher by almost a factor of 5 during tide 10 compared to tide 20. As a result of this, the difference in magnitude of F^+ between the three tides is smaller at the shoreline than it is in deeper water. For example, at $h \approx 3$ m, F^+ during tide 10 is $0.054 \text{ m}^3 \text{ s}^{-1}$ more than tide 1, which in turn is $0.042 \text{ m}^3 \text{ s}^{-1}$ more than tide 20. Whereas at $h \approx 1$ m these numbers are $0.036 \text{ m}^3 \text{ s}^{-1}$ and $0.022 \text{ m}^3 \text{ s}^{-1}$, respectively.

As further evidence of this dissipation, bulk infragravity reflection coefficients (Figure 5.8J-L) averaged across the array are 0.16, 0.23, and 0.15 for tides 10, 1, and 20, respectively. Bulk reflection coefficients increase slightly towards the shore where, despite reaching their maximum, are well below 0.5. This implies that considerable

dissipation of F^+ , equal to $>50\%$, occurs over the short and shallow cross-shore stretch between the shallowest sensor and the shoreline (typically ~ 30 m). The difference in R^2 at the shallowest sensor during the three tides can, at least partially, be attributed to differences in the swash zone beach slope. Tide 1, which had the highest shoreline R^2 of 0.43, was during the spring tide phase when the swash zone was located further landward and characterized by steeper slopes close to the fore dunes. Whereas tide 20 was during the neap tide phase when the swash zone was situated further seaward where the foreshore slope is gentler, hence the smaller shoreline R^2 of 0.28.

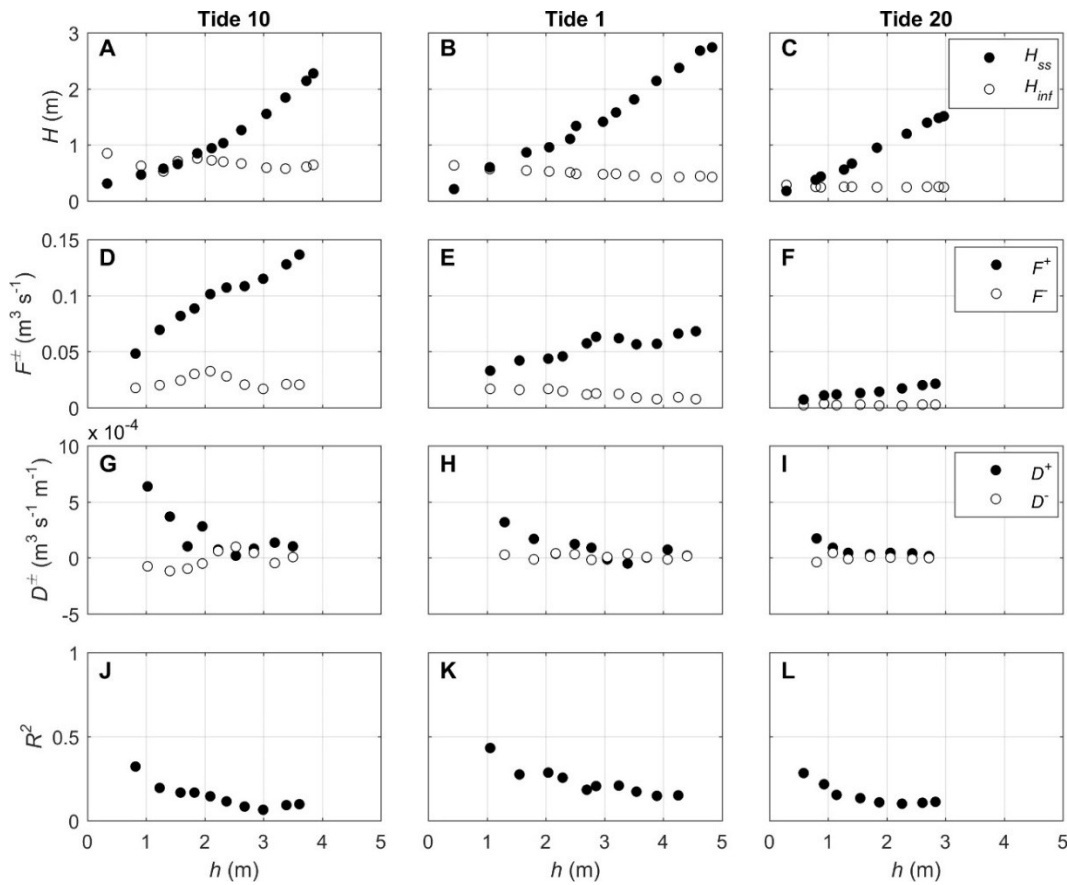


Figure 5.8. Sea-swell H_{SS} (dots) and infragravity H_{inf} (circles) significant wave height (A-C), bulk incident F^+ (dots) and reflected F^- (circles) infragravity energy flux (D-F), bulk incident D^+ (dots) and reflected D^- (circles) infragravity dissipation rate (G-I), and bulk infragravity reflection coefficient R^2 (J-L), versus water depth h for tides 10 (left panels), 1 (middle panels), and 20 (right panels). Mean 95% confidence intervals on F^\pm , calculated following the method outlined in Section 4.4.1, are $\pm 0.0013 \text{ m}^3 \text{ s}^{-1}$, $\pm 0.0010 \text{ m}^3 \text{ s}^{-1}$, and $\pm 0.0006 \text{ m}^3 \text{ s}^{-1}$ for tides 10, 1, and 20, respectively. Mean 95% confidence intervals on R^2 are ± 0.040 , ± 0.024 , and ± 0.034 for tides 10, 1, and 20, respectively.

To investigate the cross-shore structure of infragravity waves, as well as potential frequency-dependence, a frequency domain Complex Empirical Orthogonal Function (EOF) of the infragravity sea-surface elevation is implemented following Henderson et al. (2000). In this method, an eigenfunction analysis of the cross-spectral matrix at individual infragravity frequencies is performed with the foremost eigenfunction representing the dominant cross-shore structure of infragravity waves at that frequency. For the examples presented here, the dominant eigenfunction accounted for between 72% and 96% of the variance summed over the array. Figure 5.9 shows the EOF results and frequency-dependent reflection coefficients for three infragravity frequencies during the three example tides. These frequencies were chosen arbitrarily as representative low, medium, and high frequencies within the infragravity band. At the lowest frequency of $f = 0.0078$ Hz (128 s) the non-dimensional amplitude M of the dominant EOF displays a clear standing wave structure for all tides. The shoreward increase in M at distances < 100 m indicate the presence of an antinode at the shoreline, with a second antinode at a distance of approximately 225 m and a node at around 100 m, with a phase jump of $\pm\pi$ at the node. An (anti)nodal structure is also evident at $f = 0.0195$ Hz (51 s), although less clear, but phase now increases more linearly shoreward. The pattern at $f = 0.0391$ Hz (26 s) is one of decreasing amplitude in the shoreward direction for all tides and phase increases are entirely linear, indicative of progressive waves with little or no shoreline reflection. The patterns shown by the EOFs agree well with the frequency-dependent reflection coefficients which, at each frequency, are similar for the three tides and average (\pm one standard deviation) 0.45 ± 0.09 , 0.21 ± 0.05 , and 0.05 ± 0.02 for 0.0078 Hz, 0.0195 Hz, and 0.0391 Hz, respectively (Figure 5.9G-I).

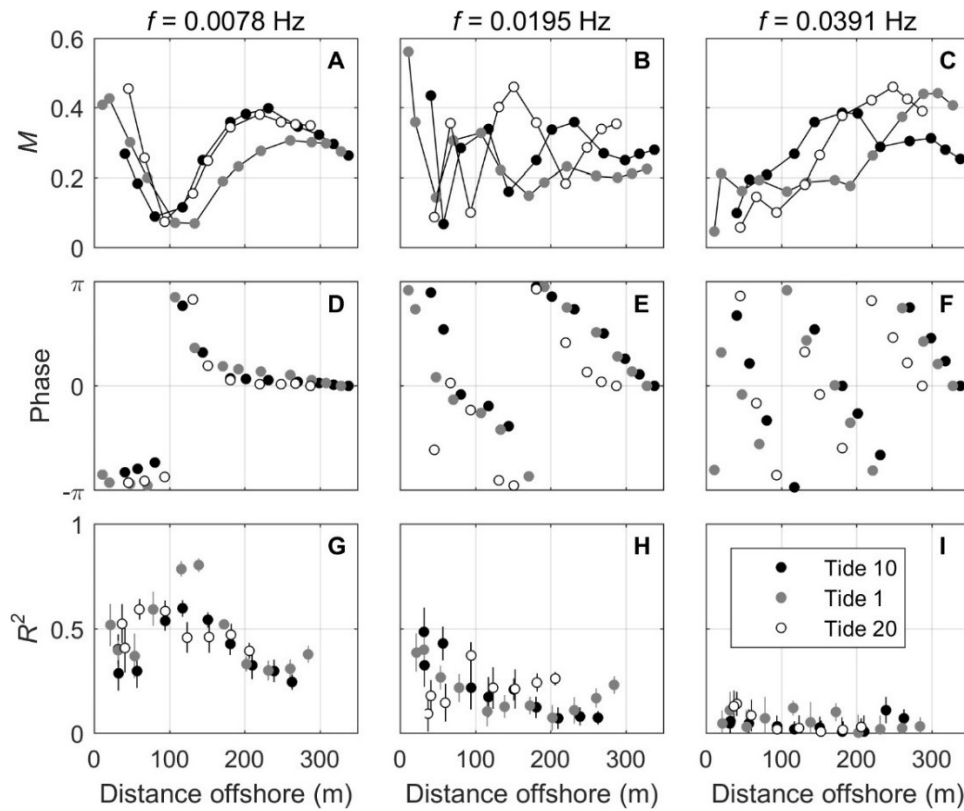


Figure 5.9. Non-dimensional amplitude M (A-C), phase (D-F), and reflection coefficients R^2 (G-I) versus distance offshore for $f = 0.0078$ Hz (left panels), $f = 0.0195$ Hz (middle panels), and $f = 0.0391$ Hz (right panels). Black dots are tide 10, grey dots are tide 1, and circles are tide 20. M and phase are associated with the dominant Empirical Orthogonal Function (EOF), computed following Henderson et al. (2000). Error bars in G-I are 95% confidence intervals on R^2 following the method outlined in Section 4.4.1.

These observations imply that dissipation of infragravity waves is frequency-dependent, with high frequency waves dissipating more than low frequency waves. To demonstrate this further, the infragravity band is partitioned into three smaller bands; low ($0.005 < f < 0.017$ Hz), medium ($0.017 < f < 0.028$ Hz), and high ($0.028 < f < 0.04$ Hz). At $h \approx 3$ m during tide 10, the ratio of F^+ in the low frequency band to that in the high frequency band is 1.99. Whereas at $h \approx 1$ m, increased dissipation in the high frequency band has increased this ratio to 7.95. During tide 20, energy in the low frequency infragravity band is less than that in the high frequency band at $h \approx 3$ m with a ratio of 0.57. Similar to tide 10, however, this ratio increases shoreward to 1.06 at $h \approx 1$ m, indicative of high frequency dissipation. At the shallowest sensor, $>90\%$ of the total F^- is within the low

infragravity frequency band for the three tides. This implies that almost all of F^+ remaining at frequencies >0.017 Hz must have dissipated between the shallowest sensor and the shoreline.

Figure 5.10 shows bulk R values for the total infragravity band and the three partitioned infragravity bands during all 33 tides versus β_H . In calculating β_H , H^+ is estimated as $H^+ = 4 \sqrt{\int_{lf}^{hf} S^+(f) df}$, where hf and lf represent the high and low frequency cut-offs for each infragravity band, respectively, and T is taken as the central wave period of each frequency band. The location at which the mean water level at the shallowest sensor intersected the beach face was taken as the centre of the swash zone. The infragravity runup elevation was estimated as $S_{ig} = 0.06(H_o L_o)^{1/2}$, following Stockdon et al. (2006), and this was used to calculate the swash zone beach slope for each tide. For the total infragravity band (Figure 5.10A), R values are typically in the range 0.2 – 0.5, placing them in a mild sloping regime, and increase with β_H which is predominantly <2 . Values of $R < 0.4$ agree well with the theoretical curve of Van Dongeren et al. (2007); however, R values >0.4 show evidence of a more gentle increase with β_H . A clear relationship between partitioned R values and β_H can be seen in Figure 5.10B, with R in the high frequency band corresponding to β_H values less than 2. Higher values of R in the low and medium frequency bands correspond to typical β_H values of $2 < \beta_H < 7$ and $1 < \beta_H < 3$, respectively. For the two higher frequency infragravity bands, R values tend to increase with increasing β_H . However, R in the low frequency band plateaus around 0.7 when $\beta_H \approx 3$, thus distinguishing the mild to steep sloping regime. The location of this transition implies that infragravity frequencies >0.017 Hz are in the mild sloping regime and dissipate energy due to wave breaking, whereas frequencies <0.017 Hz are more commonly in the steep sloping regime allowing for stronger reflection. It must be noted that β_H is influenced by the bandwidth of the frequency range used in its calculation.

Therefore, the comparison of β_H for different size frequency bands (i.e., Figures 5.10A and 5.10B) should be carried out with caution.

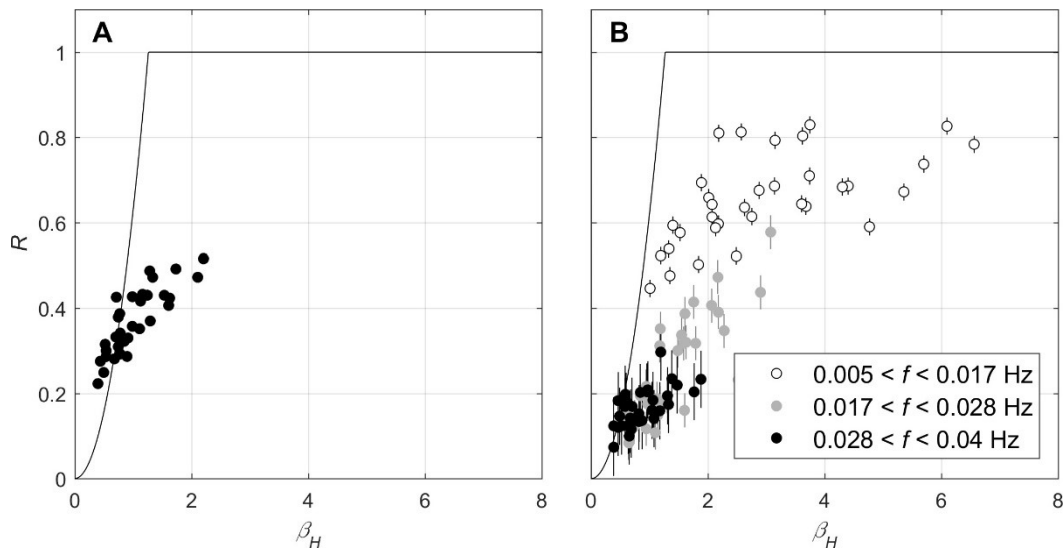


Figure 5.10. Bulk amplitude reflection coefficients R for the total infragravity band (A) and for partitioned infragravity bands (B) versus the normalised bed slope parameter β_H . The solid black lines are $\min(1, R = 0.2\pi\beta_H^2)$, following Van Dongeren et al. (2007). Error bars in B are 95% confidence intervals on R following the method outlined in Section 4.3.2. The R values in A have 95% confidence intervals that are too small to be included on the figure, with mean and maximum confidence intervals of ± 0.020 and ± 0.034 , respectively.

5.3 Discussion

5.3.1 Relationship with offshore forcing

The infragravity waves measured during this study were well correlated with the wave conditions offshore, suggesting that they are driven by the local short wave regime rather than travelling from a distant source. The much stronger correlation between infragravity wave height and offshore swell waves rather than sea waves has been observed at other sites (e.g., Elgar et al., 1992; Okihiro et al., 1992; Ruessink, 1998a).

Infragravity wave height is best predicted by using an independent variable that accounts for wave period. This is consistent with the findings of Stockdon et al. (2006) and Senechal et al. (2011) whilst studying infragravity runup, although a stronger prediction

is obtained by using $H_o^2 T_p$ rather than their parameter $(H_o L_o)^{1/2}$. The parameter $H_o^2 T_p$ is proportional to the offshore energy flux and therefore has arguably better physical justification than $(H_o L_o)^{1/2}$.

The stronger correlation between infragravity wave height close to shore and H_{swell} or another a parameter that accounts for wave period is explained by longer period swells tending to have a narrower spectrum than shorter period wind-sea. To demonstrate this in the present study, the dimensionless bandwidth parameter (Longuet-Higgins, 1984), which provides a measure of the narrowness of the spectrum, was calculated and found to be positively correlated with T_p with an r^2 of 0.51. In bound wave theory, the strength of the coupling between pairs of sea-swell waves is stronger under narrow-banded conditions and when the two frequencies are close together, whereas under broad-banded conditions energy transfers are weaker and spread over a larger range of frequencies (Hasselmann, 1962; Longuet-Higgins and Stewart, 1962). Stronger coupling and higher levels of infragravity energy under narrow-banded conditions has been demonstrated by field (e.g., Elgar and Guza, 1985), laboratory (e.g., De Bakker et al., 2015), and modelling (e.g., Okihiro et al., 1992; Norheim et al., 1998) studies.

Further support for bound wave theory is provided by the negative correlation between the infragravity waves and the wave group envelope. The observed time lag of the infragravity wave behind the wave group envelope was also observed by List (1991) and Masselink (1995), and has been shown to be a necessary condition for the transfer of energy from short waves to shoaling bound waves (e.g., Janssen et al., 2003; Battjes et al., 2004). The bound infragravity waves appear to be released, as indicated by a change from negative to positive correlations with the wave group envelope, not at the initiation of short wave breaking but further into the surf zone at $h/h_b \approx 0.7$, where all short waves are likely to have broken and the ‘offshore’ wave groups are destroyed.

The best fit linear slope of infragravity wave height to H_o is steeper than that measured by De Bakker et al. (2014) on a dissipative beach in the Netherlands with similar wave heights, but much smaller wave periods. Indeed, the maximum offshore wave period measured during their study was less than the minimum wave period during any of the high tides in the present study. However, it must be noted that De Bakker et al. (2014) observed some saturation for $H_o > 3$ m which would act to lower the slope of the linear fit line.

In the present dataset, the swell frequency band accounts for an average of 73% of the total short wave energy offshore and T_p is in the swell band for all high tides. Field campaigns on limited fetch coastlines, such as the Netherlands, observe T_p , and presumably the bulk of the short wave energy, in the sea frequency band. This likely plays a role in the smaller infragravity wave heights and responses to H_o reported on these coastlines, and possibly the likelihood of saturation occurring.

Whilst the infragravity wave height increases with offshore forcing without signs of saturation, infragravity dissipation rates in the surf zone also increase and amplification of the infragravity wave height from the deepest sensor to the shallowest decreases. That is to say, as the offshore forcing intensifies, the corresponding increase in infragravity wave height and energy flux reaching the shoreline becomes progressively smaller. In fact, had the largest amplification of the infragravity wave height that occurred during low offshore wave forcing also occurred during the most energetic offshore conditions, the shoreline infragravity wave height would be 2.67 m rather than the 1.02 m that was observed. Similar observations were found by Fiedler et al. (2015) on a fetch-unlimited beach and, interestingly, the largest infragravity wave height they measured with $H_o > 7$ m was around 1.2 m; only 0.18 m more than that measured in the present study with H_o less than half the size.

5.3.2 Infragravity dissipation

Consistent with previous field studies (e.g., Henderson et al., 2000; Guedes et al., 2013; De Bakker et al., 2014), the infragravity dissipation observed is frequency-dependent with more energy being conserved at lower frequencies. Furthermore, dissipation rates are higher in the inner surf zone and reflection coefficients indicate that a significant amount of dissipation occurs between the shallowest sensor and the shoreline. Relating R to β_H places infragravity frequencies >0.017 Hz in the mild sloping regime suggesting that dissipation at these frequencies, at least at the shoreline, is due to infragravity wave breaking. The transition between mild and steep sloping regime at $\beta_H \approx 3$ is higher than $\beta_H \approx 1.25$ observed by Van Dongeren et al. (2007), but consistent with the field measurements of De Bakker et al. (2014); however, as the aforementioned study acknowledged, obtaining measurements on the edge of the swash zone is more problematic in the field compared to the laboratory, especially when using an array of pressure sensors to estimate reflection.

In contrast to the dissipation observed in the present study, the dissipation observed by Thomson et al. (2006), which was ascribed to non-linear energy transfers, was strongest in the middle of the surf zone and decreased closer to shore where there was almost complete reflection. Interestingly, however, Thomson et al. (2006) observed the transition from increasing to decreasing F^+ at a normalised surf zone (their x_{sz}) position of 0.7, as was found in the present study. Baldock (2012) points out that, during energetic offshore conditions (H_o and T_p), the larger short waves may not be true shallow water waves at the time of breaking and that, until the short waves are in shallow water, the bound infragravity wave does not satisfy the free wave dispersion relationship required for its release. The conditions required for short waves to be in shallow water when they break can be parameterized in terms of the deep water short wave steepness (Baldock and

O'Hare, 2004) as $\frac{H_o}{L_o} \leq 0.016\gamma_b$. In the present study, the largest short waves broke as shallow water waves for only 6 out of the 33 high tides, corresponding to lower values of $H_o^2 T_p$. Based on this theory, a possible explanation for the release and onset of infragravity wave dissipation at $h/h_b \approx 0.7$ is that the bound waves are still being forced past the breakpoint of the largest short waves and into the surf zone until shallow water wave conditions are satisfied.

5.3.3 Non-linear energy transfer

Bispectral analysis, first introduced by Hasselmann et al. (1963), is performed on the data to examine the possible role of non-linear energy transfer in the observed infragravity dissipation. The bispectrum B_{f_1, f_2} describes triad interactions between frequencies f_1 and f_2 , and their sum frequency $f_3 = f_1 + f_2$. A detailed description of bispectral analysis is provided by, for example, Elgar and Guza (1985) and Collis et al. (1998). The imaginary part of the bispectrum is used to examine the direction and magnitude of energy transfers; positive interactions indicate a transfer of energy from f_1 and f_2 to their sum f_3 , whereas negative interactions indicate a transfer of energy from f_3 to f_1 and f_2 . In calculating the bispectrum, longer time series of 16384 were used and bispectral estimates were averaged to give a frequency resolution of 0.0117 Hz and 186 degrees of freedom. This was necessary to lower the 95% significance threshold on bicoherence to 0.18 (Kim and Powers, 1979).

Figure 5.11 shows the imaginary part of the bispectrum at three cross-shore locations during tide 10; the example tide with the highest T_p value. In the middle of the surf zone at $h/h_b = 0.44$ (Figure 5.11A), a positive (red) interaction at $B(0.065, 0.065)$ indicates that, despite being well within the surf zone, energy is still being transferred from the spectral peak to its first harmonic at $f_3 = 0.130$ Hz, where a weaker positive interaction

shows that energy is being transferred to the second harmonic also. A negative (blue) interaction near $B(0.047, 0.012)$ is associated with a transfer of energy from $f_3 = 0.59$ Hz, close to the peak frequency, to $f_1 = 0.047$ Hz and to the infragravity band at $f_2 = 0.012$ Hz.

Further shoreward at $h/h_b = 0.27$ (Figure 5.11B), the positive interaction involving the spectral peak has weakened significantly (note change in colour scale), whereas the negative interaction transferring energy to the infragravity band remains strong. A positive infragravity-infragravity interaction has now emerged at around $B(0.023, 0.012)$ transferring energy from these low infragravity frequencies to the higher infragravity frequency $f_3 \approx 0.035$ Hz.

Very close to shore at $h/h_b = 0.11$ (Figure 5.11C), two positive interactions exist involving the infragravity spectral peak. The peak-peak interaction at $B(0.012, 0.012)$ indicates a transfer of energy to a higher infragravity harmonic at $f_3 = 0.024$ Hz, which subsequently appears to be transferred to the next harmonic close to the boundary with the sea-swell band.

Similar trends as seen in Figure 5.11 are present during most tides, although interactions weaken with decreasing energy offshore and are spread out over a larger range of frequencies when the offshore wave period is lower and the spectrum is more broad-banded. This is consistent with past studies such as Elgar and Guza (1985), Norheim et al. (1998), and De Bakker et al. (2015).

The results of the bispectral analysis suggest that non-linear energy transfers from infragravity to sea-swell frequencies do not play an important role in the observed infragravity energy loss. Rather, transfers of infragravity energy to higher frequencies tend to occur in shallow water as an energy transfer to higher harmonics of the

infragravity wave. This transfer of energy to higher infragravity harmonics is analogous to the shoaling process of sea-swell waves outside the surf zone and ultimately supports the steepening and eventual breaking of infragravity waves close to shore.

Due to the lack of co-located pressure and velocity data, bispectra were calculated using the total wave signal as opposed to the decomposed incident wave signal. This has been shown to cause a decrease in levels of bicoherence (Elgar and Guza, 1985; De Bakker et al., 2015); however, general trends in the bispectra are relatively unaffected, especially with narrow-banded spectra when the coupling between frequencies is strong, such as that shown in Figure 5.11.

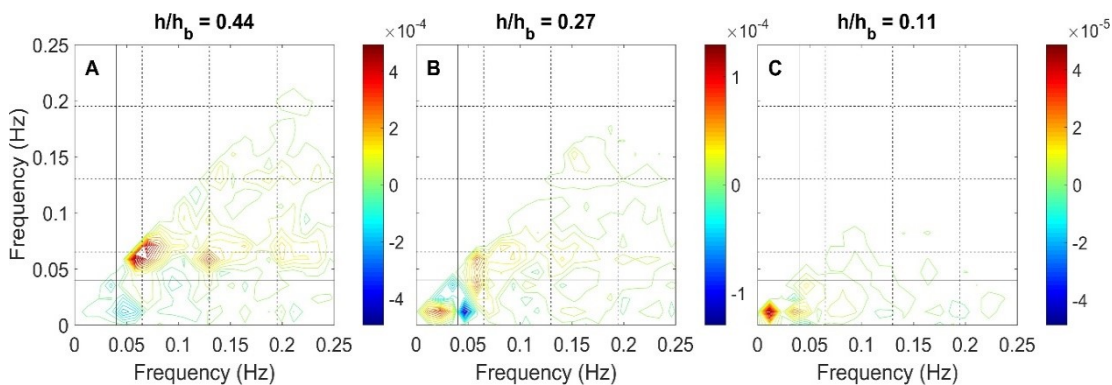


Figure 5.11. Imaginary part of the bispectrum from tide 10 ($H_o = 2.96$ m, $T_p = 15.4$ s) at three normalised surf zone h/h_b locations; 0.44 (A), 0.27 (B), and 0.11 (C). Where the corresponding bicoherence is below the 95% significant threshold of 0.18, bispectral estimates are set to zero. Solid black lines indicate the transition between infragravity and sea-swell frequency bands. Dashed lines indicate the offshore peak period and its higher harmonics.

5.4 Conclusion

Observations from a dissipative beach during a wide range of offshore forcing conditions demonstrate the difference in nearshore infragravity wave characteristics under contrasting sea and swell wave conditions. Infragravity waves are shown to be generated predominantly in accordance with bound wave theory and are released as free waves just seaward of the mid-surf zone position. Infragravity wave height at the shoreline is well

correlated with H_o , but a more accurate prediction is obtained by using $H_o^2 T_p$, which represents the offshore energy flux. Strong infragravity dissipation is observed in the surf zone and the rate of this dissipation increases with offshore forcing, thus showing a possible sign of proto-saturation of the infragravity waves. Dissipation and consequent shoreline reflection is highly frequency-dependent as waves with frequencies <0.017 Hz display a cross-shore standing wave structure and $R^2 \approx 0.4$, whereas waves with frequencies >0.028 Hz are onshore progressive and undergo almost complete dissipation ($R^2 < 0.1$). The relationship between R and β_H suggests that wave breaking is the dominant dissipation mechanism at the shoreline as all but the lowest frequency waves are in the mild sloping regime. Non-linear energy transfers in shallow water occur between the infragravity peak and its higher harmonics, thus providing further support for infragravity wave breaking.

Chapter 6

Effect of bed roughness on infragravity waves (Freshwater West experiment)

This chapter presents results of the field experiment conducted at Freshwater West, Pembrokeshire, UK. These are the first documented measurements recorded simultaneously on a beach and shore platform by two parallel instrument arrays. This work contributes to the almost complete lack of research on infragravity waves across Type A rocky shore platforms and will investigate what impact the extreme roughness of the platform compared to the beach (see Figure 3.5) has on infragravity wave dynamics.

First, an overview of the experimental conditions experienced during the study period is given, including an assessment of the alongshore contribution to infragravity hydrodynamics. Next, the dependence of infragravity wave height close to shore on offshore forcing is explored to reaffirm the effectiveness of $H_o^2 T_p$ as an infragravity forcing parameter and to determine the response difference on the beach and the platform. A more detailed comparison of infragravity wave transformation on the beach and the platform is performed using non-parametric box plots of various hydrodynamic parameters at normalised surf zone locations.

6.1 Experimental conditions

6.1.1 Offshore wave conditions

Offshore wave conditions for the study period are presented in Figure 6.1. Offshore wave height ranged between 0.78 m and 5.66 m, with a mean value of 2.34 m. Wave height was typically 2-3 m for the first five days of the study period and exceeded 3 m on two occasions for ~6 hours. A calmer period prevailed during the middle part of the experiment (days 6-11) with the wave height falling below 2 m for 5.5 days straight, but

only below 1 m for shorter periods of <6 hours. Energetic conditions returned for the final week with the offshore wave height staying above 2 m from day 12 through to the end of the study period, exceeding 4.5 m on six occasions and 5 m twice. Mean spectral peak period was 10.7 s and ranged between 9 s and 13 s for 74% of the study period. Maximum and minimum peak periods were 18.1 s and 4.8 s, respectively. Wave direction θ typically fluctuated between $\pm 20^\circ$ relative to shore-normal (245°), with more oblique wave angles coinciding with times of lower wave period (<10 s).

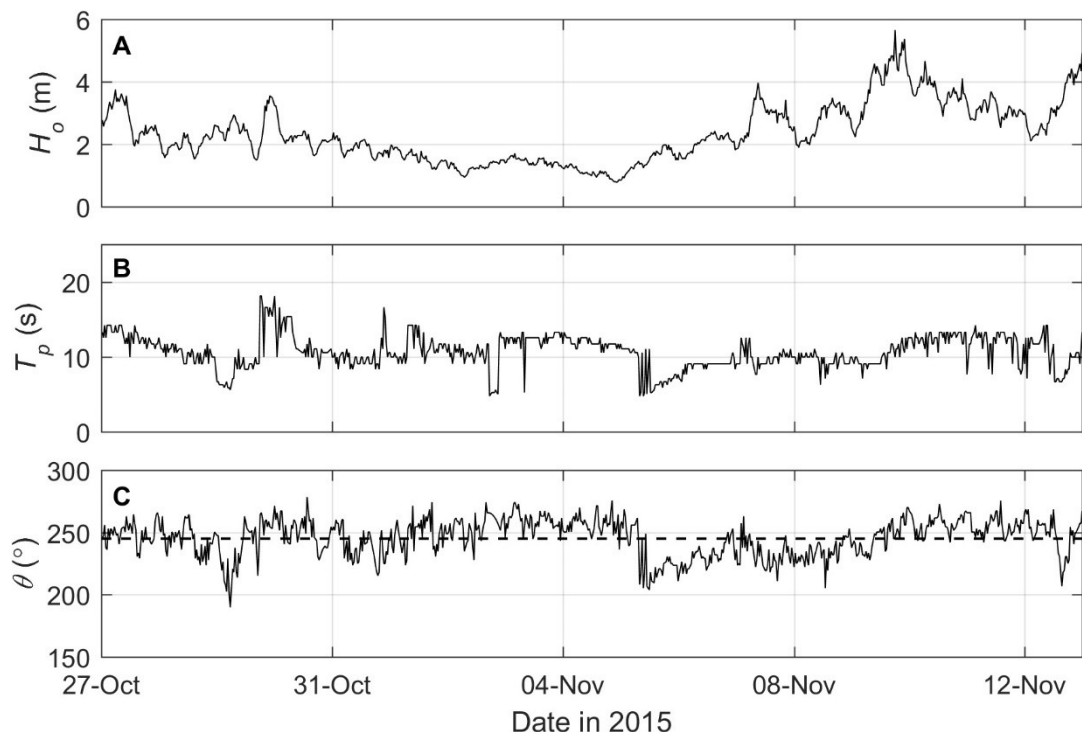


Figure 6.1. Offshore wave conditions during the study period measured by a Datawell Directional Waverider buoy at an approximate depth of -40 m ODN. Significant wave height H_o (A), spectral peak period T_p (B), and wave direction θ (C). The dashed line in (C) represents shore-normal incidence (245°).

6.1.2 Alongshore hydrodynamics

As mentioned in Section 5.1.2, it is important to assess the contribution of alongshore infragravity motions to the total infragravity signal to ensure that the results are truly representative of cross-shore infragravity waves. The same procedure as was performed

on the Perranporth data was also used with the Freshwater West data, except here PUV data are available for the entire study period rather than select tides.

At Freshwater West, the mean ratio between the alongshore and cross-shore infragravity velocity variance is 0.30 ± 0.10 and 0.24 ± 0.13 on the beach and platform, respectively (Figure 6.2A,C). While shear wave contributions to the total infragravity velocity variance are $34\% \pm 13\%$ and $30\% \pm 16\%$ on the beach and platform, respectively (Figure 6.2B,D). Following Henderson et al. (2006) and De Bakker et al. (2014), data bursts with ratios between the alongshore and cross-shore infragravity velocity variance exceeding 0.5, or shear wave contributions exceeding 50%, were excluded from further analysis. In total, 56 bursts (13%) from the beach and 18 bursts (11%) from the platform were excluded.

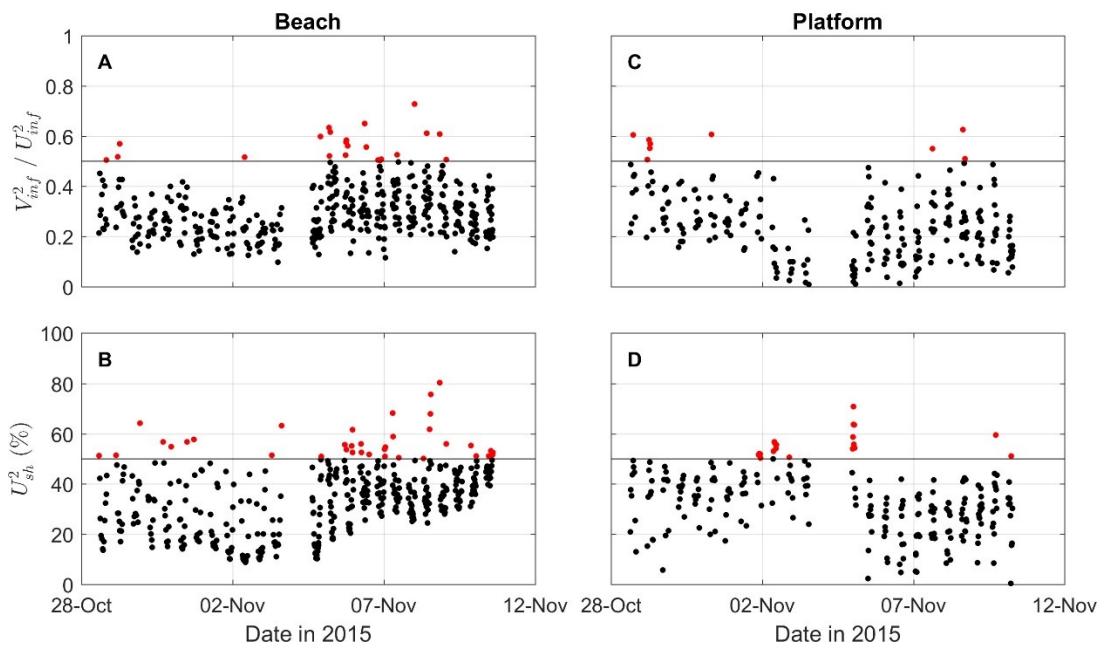


Figure 6.2. Ratio between the alongshore V_{inf}^2 and cross-shore U_{inf}^2 velocity variance in the infragravity band (A, C), and the percentage of shear wave contributions to the total infragravity velocity variance U_{sh}^2 (B, D), for the beach (left panels) and platform (right panels), during the Freshwater West field experiment. Horizontal lines in (A, C) and (B, D) indicate 0.5 and 50%, respectively. Values above these thresholds are shown in red and all data from these bursts are rejected from further analysis. Shear wave contributions were calculated following Lippmann et al. (1999).

6.2 Results and discussion

6.2.1 Basic hydrodynamic statistics

Table 6.1 provides a summary of the basic hydrodynamic statistics during the study period measured by the pressure sensors on both the beach and the platform. Mean sea-swell wave height was 0.20 m larger on the beach compared to the platform (0.90 m and 0.70 m, respectively). This can be attributed to the instrument array on the platform extending higher up the profile and thus experiencing shallower water depths. Mean values of total infragravity wave height were identical on both the beach and the platform at 0.35 m, but whilst the maximum infragravity wave height on the beach exceeded 1 m, the platform had a maximum of 0.90 m. Incident infragravity wave heights were similar on the beach and the platform with means of 0.32 m and 0.37 m, respectively, and maximums of 0.90 m and 0.88 m, respectively. However, reflected infragravity wave heights were slightly higher on the platform, as were the bulk infragravity reflection coefficients with a mean of 0.18, compared to 0.15 on the beach. Reflection coefficients well below 1 indicate significant levels of dissipation at both sites.

Table 6.1. Overview of basic hydrodynamic statistics on the beach and platform (recorded during all tides and at all locations).

	h (m)	H_{ss} (m)	H_{inf} (m)	H^+ (m)	H^- (m)	S_{inf}/S_{ss}	R^2
Beach							
Mean	2.34	0.90	0.35	0.32	0.12	0.30	0.15
Standard Deviation	1.31	0.49	0.14	0.13	0.07	0.58	0.09
Minimum	0.25	0.01	0.05	0.10	0.01	0.01	0.01
Maximum	5.81	2.43	1.03	0.90	0.49	17.29	0.46
Platform							
Mean	1.64	0.70	0.35	0.37	0.16	0.51	0.18
Standard Deviation	0.96	0.43	0.16	0.14	0.09	0.85	0.11
Minimum	0.25	0.01	0.01	0.08	0.01	0.01	0.01
Maximum	5.04	2.18	0.90	0.88	0.58	12.99	0.71

h = water depth, H_{ss} = sea-swell wave height, H_{inf} = total infragravity wave height, H^+ = incident infragravity wave height, H^- = reflected infragravity wave height, S_{inf}/S_{ss} = ratio of infragravity to sea-swell variance, R^2 = bulk infragravity reflection coefficient.

6.2.2 Generation and parameterization by offshore forcing

As with the Perranporth data (Chapter 5), in relating infragravity wave height to offshore forcing conditions, H_{inf} is averaged over the range $0 < h/h_b < 0.33$ to obtain a consistent value despite the large tidal excursion. Figure 6.3 shows that H_{inf} is well parametrized by H_o on both the beach and platform with H_o determining 76% and 75% of the variability in H_{inf} , respectively. However, consistent with the findings of Chapter 5, replacing H_o with $H_o^2 T_p$ as the independent variable in the linear regression yields improved r^2 values of 0.79 and 0.80 on the beach and platform, respectively, thus further demonstrating the importance of wave period when predicting infragravity energy levels close to shore. There is some evidence of the increase in H_{inf} slowing down for $H_o^2 T_p$ values $> 200 \text{ m}^2\text{s}$; however, there are too few values in this range to be sure whether or not this is the emergence of infragravity saturation.

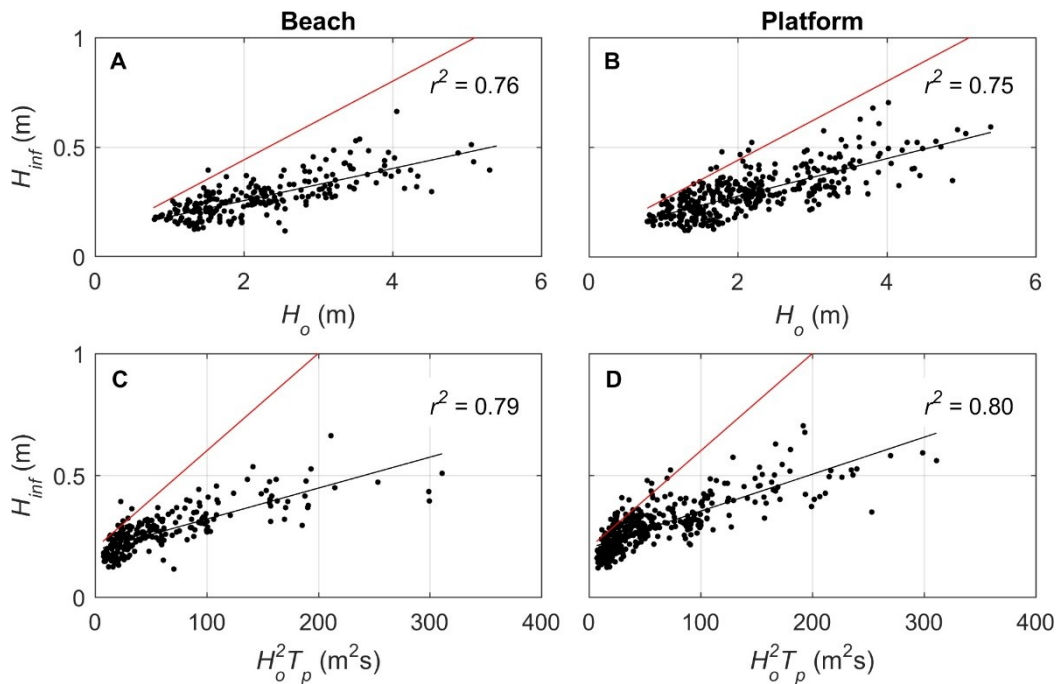


Figure 6.3. Infragravity wave height H_{inf} for $0 < h/h_b < 0.33$ versus offshore significant wave height H_o (A,B) and $H_o^2 T_p$ (C,D) on the beach (left panels) and platform (right panels). Black lines are best-fit linear regression lines with coefficients of determination given on the figure and regression coefficients given in Table 6.2. Red lines are the best fit linear regression lines for the Perranporth dataset with coefficients given in Table 6.2.

Table 6.2 gives the regression coefficients, coefficients of determination, and RMS errors associated with linear fits shown in Figure 6.3, and with other offshore parameters on the beach and platform, as well as at Perranporth. If the increased roughness of the platform compared to the beach had a dissipative effect on the infragravity wave height, then the slope of the linear regression lines would be expected to be more gentle. However, there is very little difference between the linear regression lines of the beach and platform regardless of the offshore forcing parameter used as the independent variable. Indeed, for both H_o and $H_o^2 T_p$, the regression slope is significantly steeper on the platform than the beach, albeit only slightly.

The most striking difference is between the regression lines of Freshwater West and those of Perranporth (red lines in Figure 6.3); the associated regression slopes from Perranporth are considerably steeper than those from both the beach and the platform. For example, a $H_o^2 T_p$ value of 100 m²s (approximately equivalent to $H_o = 3$ m and $T_p = 11$ s) yields $H_{inf} = 0.29$ m on the Freshwater West beach and $H_{inf} = 0.60$ m at Perranporth; a factor of 2 difference. An enquiry into the offshore wave spectra at Freshwater West and Perranporth revealed no clear shape difference between the two sites, with a similar range of dimensionless bandwidth parameters (Longuet-Higgins, 1984). This implies that the response difference observed in Figure 6.3 is related to subtle differences in the wave field that are not immediately evident from the wave spectra, or possibly related to morphological factors. If the latter is true, with similar nearshore beach slopes ($\beta \approx 0.012$ and $\beta \approx 0.011$ at Perranporth and Freshwater West beach, respectively), this could be complex and may require data from a greater range of sites and conditions to investigate fully.

Table 6.2. Regression parameters relating to linear fits between H_{inf} and various offshore forcing parameters. All coefficients of determination r^2 are significant at the 95% level.

Quantity modelled	Model input	Slope m	Intercept b	Coefficient of determination r^2	RMSE (cm)
Freshwater West - Beach					
H_{inf}	H_o	0.07 (± 0.008)	0.11	0.76	5.9
H_{inf}	H_{swell}	0.06 (± 0.006)	0.14	0.78	5.7
H_{inf}	H_{sea}	0.08 (± 0.020)	0.19	0.39	8.4
H_{inf}	$H_o^2 T_p$	0.001 (± 0.0001)	0.19	0.79	5.6
Freshwater West - Platform					
H_{inf}	H_o	0.09 (± 0.008)	0.10	0.75	6.8
H_{inf}	H_{swell}	0.07 (± 0.006)	0.13	0.80	6.3
H_{inf}	H_{sea}	0.07 (± 0.022)	0.22	0.33	9.8
H_{inf}	$H_o^2 T_p$	0.002 (± 0.0001)	0.20	0.80	6.2
Perranporth					
H_{inf}	H_o	0.18 (± 0.04)	0.08	0.79	6.7
H_{inf}	H_{swell}	0.22 (± 0.03)	0.07	0.89	4.5
H_{inf}	H_{sea}	0.19 (± 0.11)	0.25	0.28	14.4
H_{inf}	$H_o^2 T_p$	0.004 (± 0.0006)	0.20	0.93	4.2

H_{inf} = infragravity wave height where $0 < h/h_b < 0.33$, H_o = offshore significant wave height, H_{swell} = offshore significant wave height in the frequency range 0.04-0.14 Hz, H_{sea} = offshore significant wave height in the frequency range 0.14-0.33 Hz, T_p = offshore peak wave period.

To further illustrate the positive relationship between $H_o^2 T_p$ and infragravity wave height, Figure 6.4 shows the time series of $H_o^2 T_p$ during the study period and H_{inf} at locations on the beach and the platform where the water depth was about the same. Similar to the trend in H_o shown in Figure 6.1, there are two clear peaks in $H_o^2 T_p$ ($\sim 200 \text{ m}^2\text{s}$) during the first week of the study period and another broader peak towards the end (both during the spring tide phase), with a much less energetic period during the middle stage of the study period. Infragravity wave height closely replicates the trend in $H_o^2 T_p$ with no discernible difference between the beach and the platform.

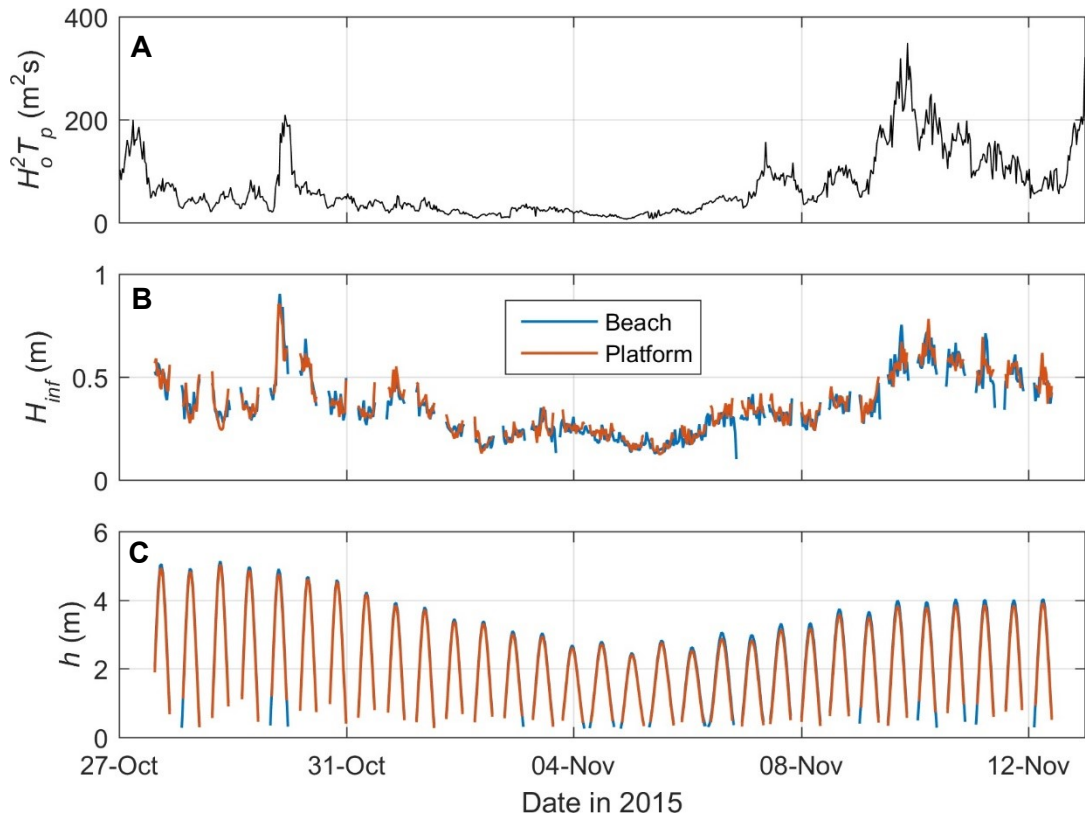


Figure 6.4. $H_o^2 T_p$ during the study period measured by a Datawell Directional Waverider buoy at an approximate depth of -40 m ODN (A), infragravity wave height H_{inf} (B), and water depth h (C) at similar elevations on the beach and the platform.

The stronger correlation with $H_o^2 T_p$ is supportive of bound wave theory as the dominant infragravity wave generation mechanism since high wave periods are typical of narrow-banded spectra which generates stronger coupling between pairs of sea-swell waves (Hasselmann, 1962; Longuet-Higgins and Stewart, 1962). Further evidence of bound wave theory on both the beach and the platform is shown in Figure 6.5 which shows the correlation coefficient at zero time lag between the wave group envelope and the infragravity time series at all locations, versus h/h_b . Values of h/h_b throughout this chapter are estimated following the method outlined in Section 5.1.3. Figure 6.5 shows predominantly negative correlations, indicative of out of phase bound waves, at $h/h_b > 0.8$ before transitioning to entirely positive correlation coefficients in the inner surf zone where the bound waves are now free and presumably modulating the sea-swell wave height. Box plots in Figure 6.5C show that there is generally no significant

difference between the correlation coefficients on the beach and the platform. The use of non-parametric box plots is adopted in this chapter as the binned data used to derive the statistics are often slightly skewed, likely owing to the few very high energy tides during the study period.

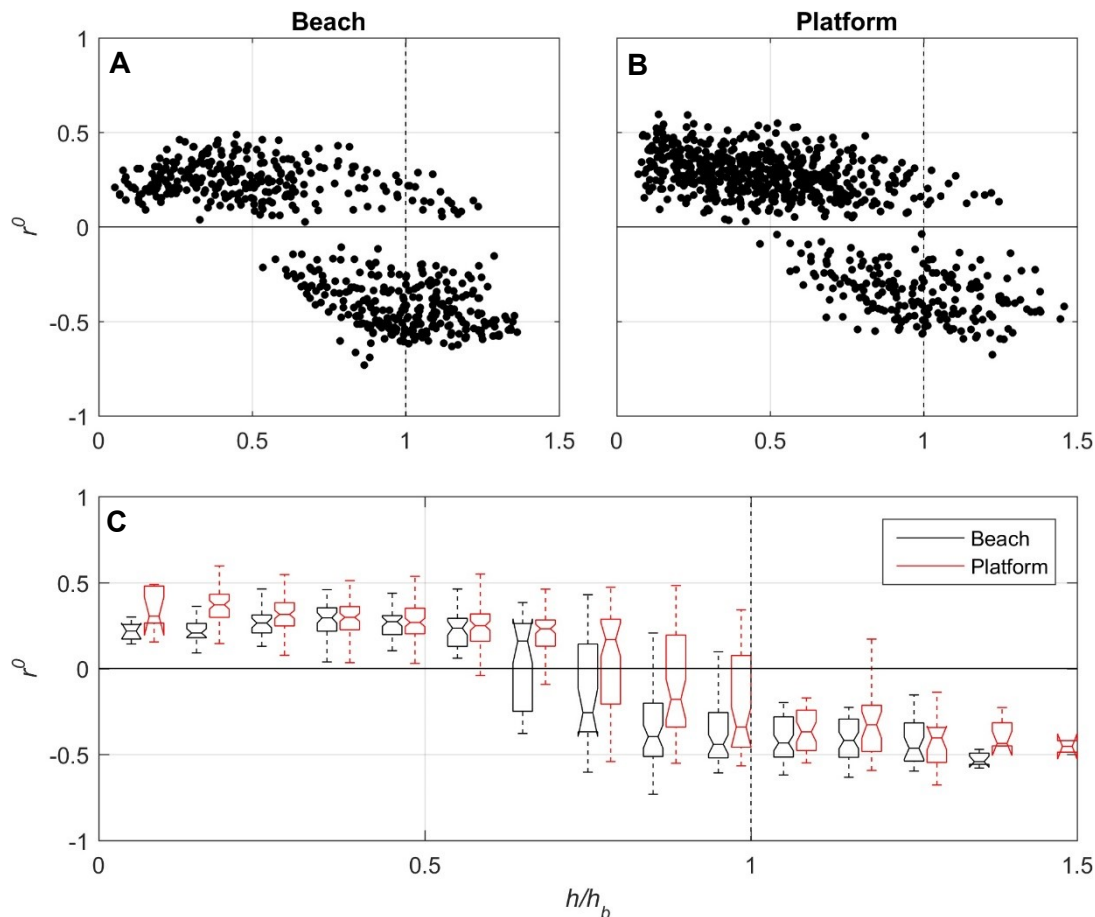


Figure 6.5. Correlation coefficient at zero time lag r^0 between the wave group envelope and the infragravity time series versus h/h_b on the beach (A) and platform (B). Box plots of r^0 versus h/h_b (C). Boxes represent a bin width of 0.1. On each box, the central line is the median, box edges are the 25th and 75th percentiles, and whiskers extend to the most extreme values not considered outliers (<0.4th percentile or >99.6th percentile). Notches in the boxes indicate the 95% confidence intervals on the median (i.e., medians are not significantly different if notches overlap). For ease of comparison, platform boxes are offset on the x-axis by 0.04. Dashed vertical lines indicate the seaward limit of the surf zone at $h/h_b = 1$. Only r^0 values significant at the 95% level are shown.

Cross-correlation between the wave group envelope outside the surf zone and the infragravity motion through the surf zone (not shown) does not exhibit any positive

correlation that may be evidence of breakpoint forced infragravity waves on either the beach or the platform.

Type B shore platforms and coral reefs promote the dominance of breakpoint forced infragravity waves due to their steep sloping regime which allows limited time for sea-swell wave shoaling and thus energy transfer to bound waves. In these environments, sea-swell waves approach out of deep water and breaking is focused on the reef crest where infragravity waves are generated in phase with the wave groups (Pomeroy et al., 2012). The platform at Freshwater West does not feature a steep platform edge but rather remains gently sloping throughout and through the transition to sand around the low tide mark. Therefore, it is logical for bound wave theory to be the dominant generation mechanism of infragravity waves on the platform as well as the beach. Values of the normalised bed slope parameter β_b (Battjes et al., 2004) are well within the mild sloping regime and lower than several other beaches where bound wave forcing has dominated over breakpoint forcing (Van Dongeren et al., 2007).

6.2.3 Sea-swell wave propagation

The cross-shore variability in sea-swell wave height, shown in Figure 6.6, displays the commonly observed ‘saturated’ behaviour in the surf zone. The breaker index γ (H_{ss}/h), derived from a linear regression of the H_{ss} values in the surf zone ($h/h_b < 1$) fit to h , is 0.38 ± 0.008 and 0.43 ± 0.012 on the beach and platform, respectively. Several studies have found that γ is positively correlated with beach gradient and interestingly the γ values for the beach and platform at Freshwater West are predicted almost exactly by Masselink and Hegge’s (1995) relationship derived from meso and macrotidal sandy beaches in Australia ($\gamma = 3.67\beta + 0.35$), which yields $\gamma = 0.39$ and $\gamma = 0.42$ for the beach and platform, respectively. The relationships proposed by Sallenger and Holman (1985) and Raubenheimer et al. (1996) predict slightly lower γ values but predict the

difference between the beach and platform accurately. These results suggest that the small difference observed in γ is likely a result of the slightly steeper slope on the platform and not the increased bed roughness. This is supported by the findings of Poate et al. (under review) who found that γ values on the other shore platforms that were studied for the WASP project are also well predicted by formulations derived from sandy beaches.

The γ values presented here are quite similar to those observed on lower gradient, Type B shore platforms; 0.4 (Ogawa et al., 2011) and 0.4-0.6 (Ogawa et al., 2015; depending on platform gradient). However, these studies calculated γ based on upper-bound values and not a regression analysis as was used herein.

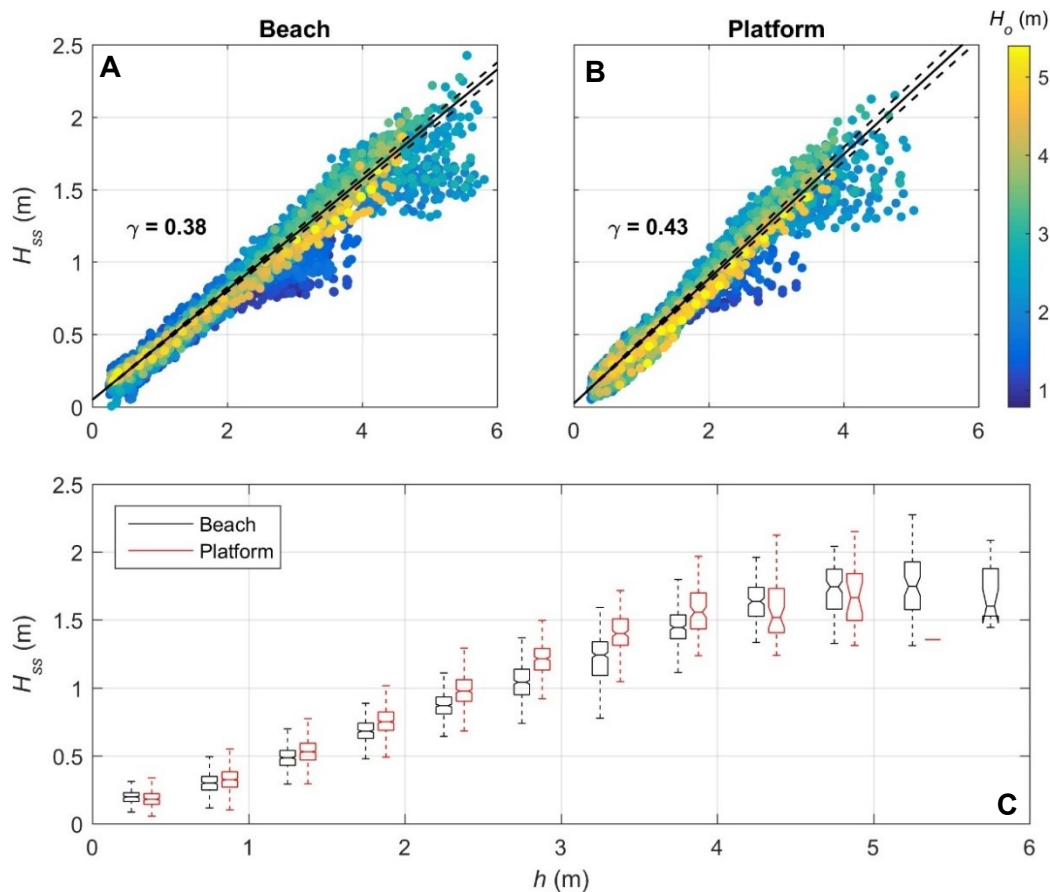


Figure 6.6. Sea-swell wave height H_{ss} versus water depth h on the beach (A) and platform (B). Box plots of H_{ss} versus h (C). Boxes represent a bin width of 0.5 m. For a description of the boxes, see Figure 6.5. For ease of comparison, platform boxes are offset on the x-axis by 0.13 m. Colour in (A) and (B) represents H_o . Solid lines in (A) and (B) are linear regression lines fit to the data, omitting values corresponding to $h/h_b > 1$, from which the breaker index γ is derived and given on the figure. Dashed lines in (A) and (B) correspond to the 95% confidence intervals on γ .

6.2.4 Infragravity wave propagation, transformation and reflection

Infragravity wave height is expressed against h/h_b in Figure 6.7. Despite considerable scatter associated with $H_o^2 T_p$, there is a general trend of decreasing H_{inf} towards the shoreline. Indeed, the largest H_{inf} of 1.03 m on the beach appears to have been measured just seaward of the sea-swell wave breakpoint. This is contrary to early infragravity wave research on sandy beaches where H_{inf} was observed to increase shoreward and contrary to the studies of Beetham and Kench (2011) and Ogawa et al. (2015), both of which measured maximum values of H_{inf} at the cliff toe on Type B shore platforms. Figure 6.7A-B shows very few H_{inf} values of less than 0.20 m, whereas 0.20 m was the peak infragravity wave height measured by Beetham and Kench (2011), and infragravity wave heights measured by Pomeroy et al. (2012) on a coral reef were <0.30 m, albeit forcing conditions were less energetic during these studies. Whilst the platform maintains a greater range of infragravity wave heights close to shore, Figure 6.7C shows that there are generally no significant differences in H_{inf} between the beach and the platform. The greater range in the results shown for the platform in Figure 6.7, and succeeding figures, can be attributed to there being twice as many pressure sensors on the platform than the beach and covering a larger cross-shore distance (see Figure 3.4).

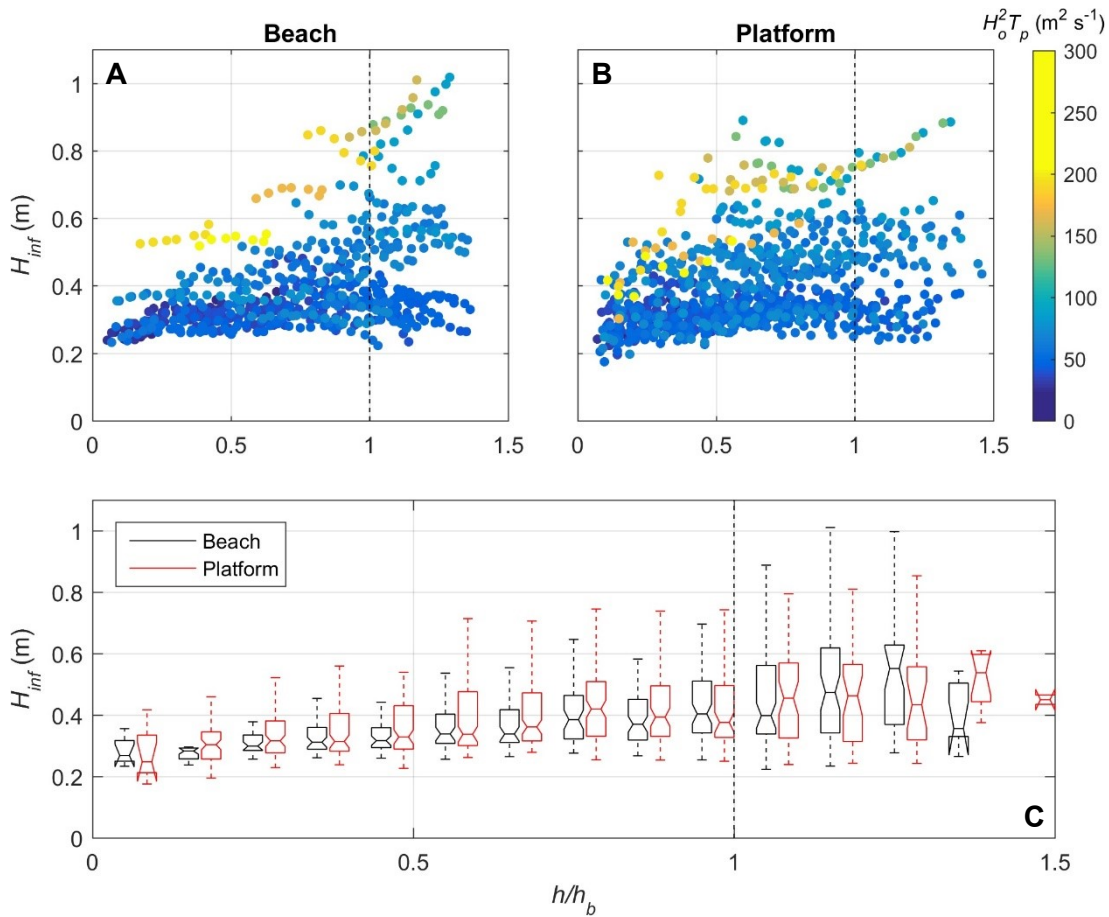


Figure 6.7. Infragravity wave height H_{inf} versus h/h_b on the beach (A) and platform (B). Box plots of H_{inf} versus h/h_b (C). Box plots represent a bin width of 0.1. For a description of the boxes, see Figure 6.5. For ease of comparison, platform boxes are offset on the x-axis by 0.04. Dashed vertical lines indicate the seaward limit of the surf zone at $h/h_b = 1$. Colour in (A) and (B) represents $H_o^2 T_p$.

Despite the shoreward decrease in H_{inf} , Figure 6.8A-B shows that infragravity waves become increasingly important relative to sea-swell waves in shallow water. Infragravity waves typically make up <20% of the total wave variance where $h > 4$ m, but can dominate the water motion, accounting for >80%, in depths of <1 m. Although, sea-swell energy can still dominate during low energy conditions when infragravity waves can account for <10% of the total variance even in shallow water. The depth at which infragravity waves become more significant tends to increase under higher energy conditions ($H_o^2 T_p > 150$), as evident by the distribution of green-yellow dots in Figure

6.8A-B. These results closely reflect the difference in H_{inf} with $H_o^2T_p$ observed in Figure 6.7.

Figure 6.8C shows that infragravity waves on the platform, at times, accounts for a small but significant amount more of the total variance compared to the beach. For example, the boxplots corresponding to $h = 0.5$ m show that median infragravity wave contributions are $51.1\% \pm 6.2\%$ on the beach and $65.0\% \pm 5.5\%$ on the platform, respectively. However, values for the platform also span a greater range, particularly at $h < 2$ m.

The switch in dominance from sea-swell waves to infragravity waves in shallow water, particularly during more energetic conditions, is consistent with many studies on dissipative sandy beaches, as well as some Type B shore platforms and coral reefs. Beetham and Kench (2011), however, whilst reporting a shoreward increase in H_{inf} , did not observe infragravity dominance at the shoreline with maximum H_{inf} values only equal to 74% of H_{SS} .

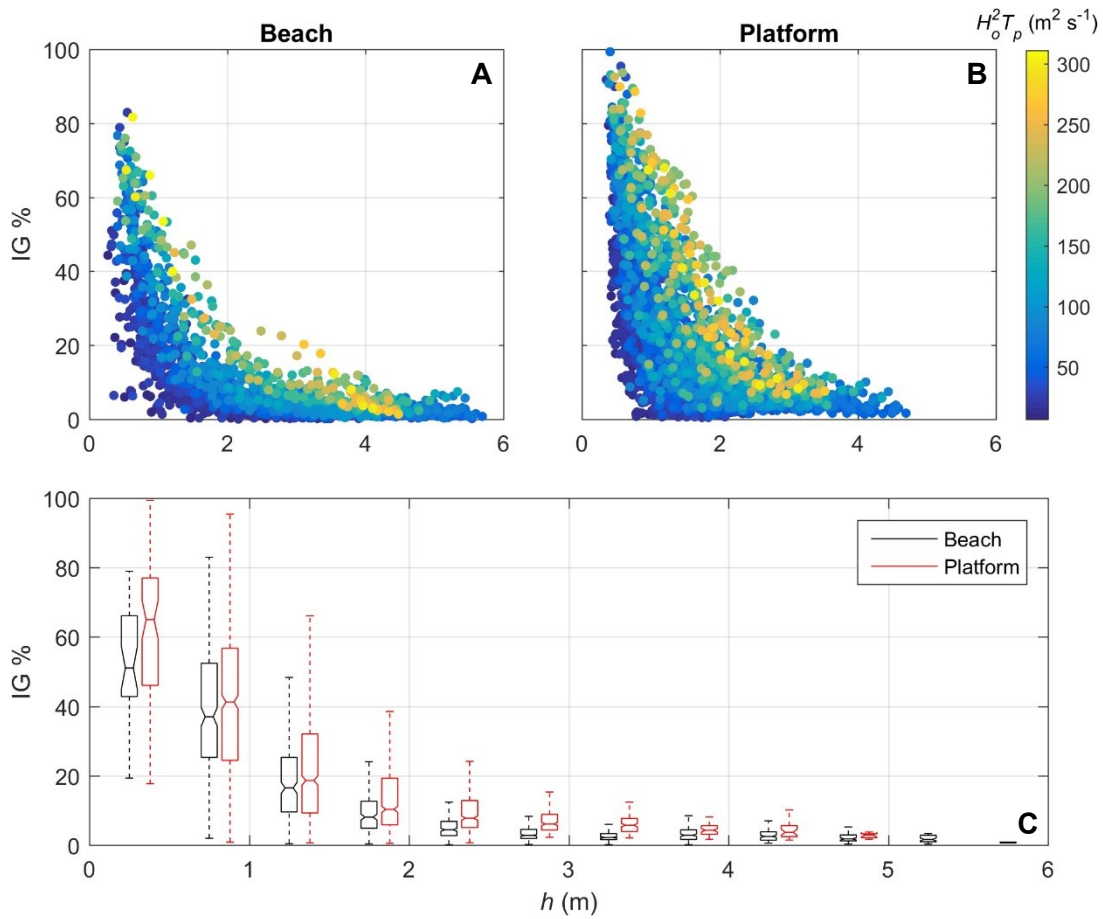


Figure 6.8. Percentage of total variance in the infragravity band IG% versus water depth h on the beach (A) and platform (B). Box plots of IG% versus h (C). Boxes represent a bin width of 0.5 m. For a description of the boxes, see Figure 6.5. For ease of comparison, platform boxes are offset on the x-axis by 0.13 m. Colour in (A) and (B) represents $H_o^2 T_p$.

To investigate the actual dissipation of infragravity waves on the beach and the platform, Figure 6.9 presents the bulk incident infragravity energy fluxes normalised by the mean value for each tide to collapse the data. Despite some scatter and no clear pattern outside the surf zone, there is clearly a trend of decreasing energy flux inside the surf zone, especially at $h/h_b < 0.8$. This is consistent with the dissipation of infragravity waves and is in close agreement with the results from the Perranporth field experiment presented in Chapter 5.

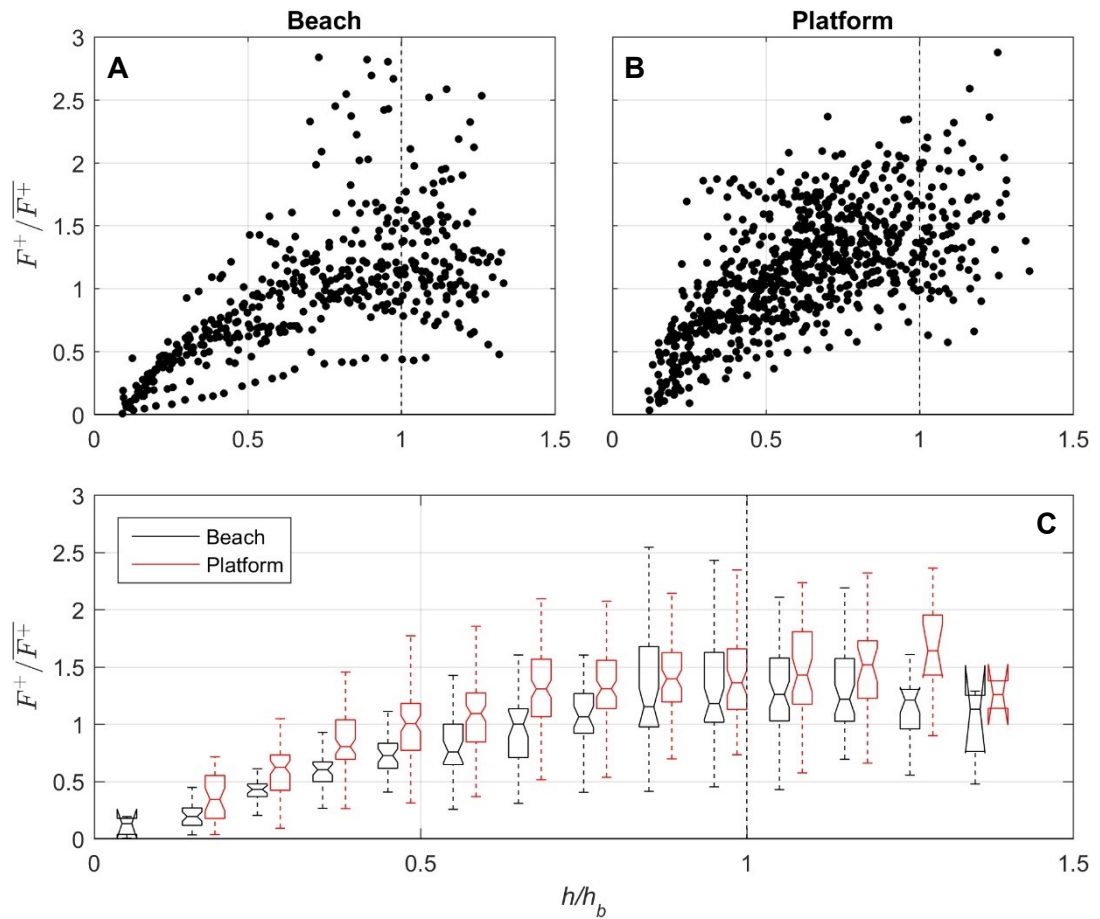


Figure 6.9. Bulk incident infragravity energy flux F^+ normalised by the mean value $\overline{F^+}$ versus h/h_b on the beach (A) and platform (B). Box plots of $F^+/\overline{F^+}$ versus h/h_b (C). Box plots represent a bin width of 0.1. For a description of the boxes, see Figure 6.5. For ease of comparison, platform boxes are offset on the x-axis by 0.04. Dashed vertical lines indicate the seaward limit of the surf zone at $h/h_b = 1$.

To investigate this dissipation in more detail and specifically any differences between the beach and the platform, Figure 6.10 presents bulk infragravity dissipation rates associated with the incident infragravity waves. Dissipation rates from the shoaling zone through to around the mid surf zone position show no clear trend with much of the data scattered around zero. The box plots in Figure 6.10C show that, outside of the surf zone, median dissipation rates on both the beach and the platform are not significantly different from zero. This is indicative of conservative infragravity wave shoaling in this region. However, in the inner surf zone ($h/h_b < 0.5$) dissipation rates go predominantly positive and reach levels similar to that observed at Perranporth during the highest energy example tide ($0.0005\text{-}0.001 \text{ m}^3 \text{ s}^{-1} \text{ m}^{-1}$), although some scattered values on the platform are

considerably higher. The highest dissipation rates occur in the shallowest water depths ($h < 1$ m), as emphasised by the colour scheme in Figure 6.10A-B. Box plots of dissipation rates in the inner surf zone are always significantly higher than zero; however, there is no significant difference between infragravity dissipation rates on the beach and the platform.

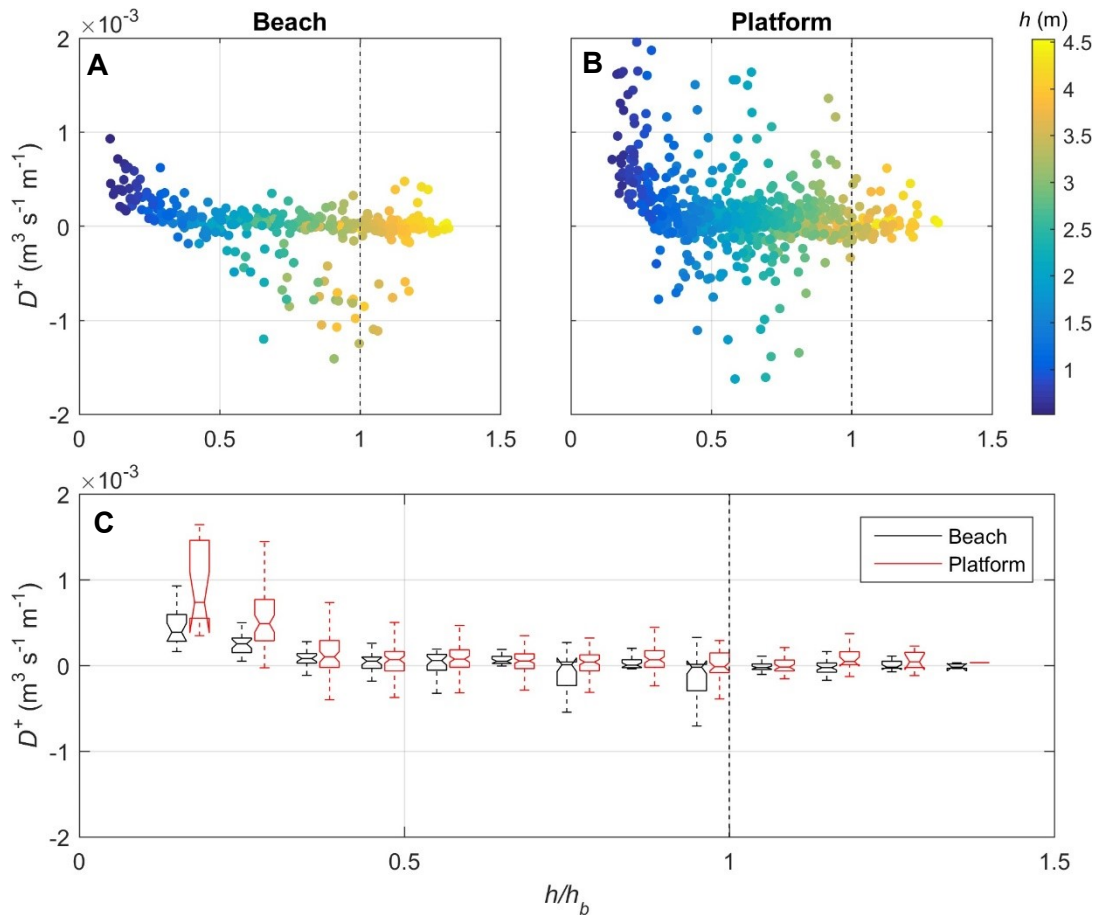


Figure 6.10. Bulk incident infragravity dissipation rate D^+ versus h/h_b on the beach (A) and platform (B). Box plots of D^+ versus h/h_b (C). Box plots represent a bin width of 0.1. For a description of the boxes, see Figure 6.5. For ease of comparison, platform boxes are offset on the x-axis by 0.04. Dashed vertical lines indicate the seaward limit of the surf zone at $h/h_b = 1$. Colour in (A) and (B) represents h .

The difference in wave transformation between the beach and the platform is further demonstrated in Figure 6.11 which presents the cross-shore variation in H_{SS} , H_{inf} , F^+ , and D^+ for tide 30 ($H_o = 3.18$ m, $T_p = 12.6$ s, $H_o^2 T_p = 127.4$ $\text{m}^2 \text{s}$). Tide 30 was chosen to provide an individual example as it well-represents moderate-high energy conditions and

occurred during the spring tide phase, thus providing a good range of spatial and temporal data. Data from ± 1.5 hours either side of high tide are used here.

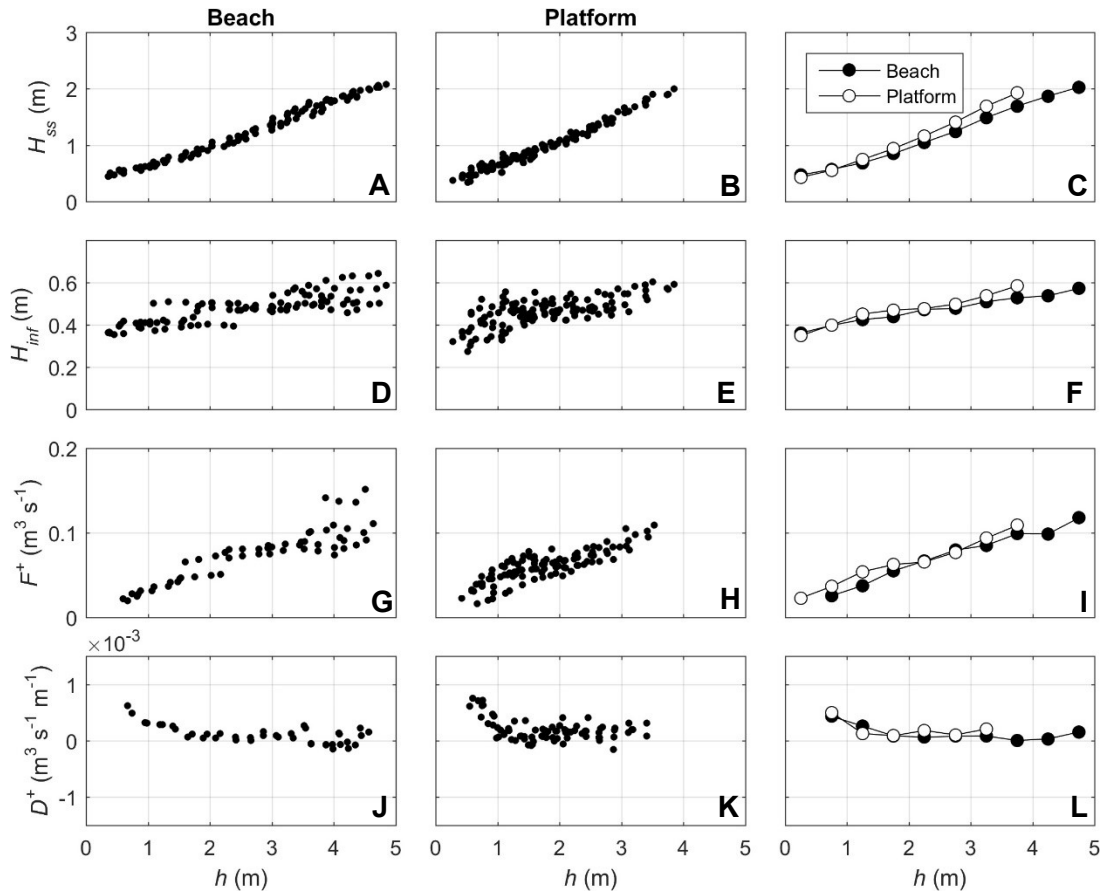


Figure 6.11. Sea-swell significant wave height H_{SS} (A-C), infragravity significant wave height H_{inf} (D-F), bulk incident infragravity energy flux F^+ (G-I), and bulk incident infragravity dissipation rate D^+ (J-L), versus water depth h for tide 30 ($H_o = 3.18$ m, $T_p = 12.6$ s). Left panels are the beach, middle panels are the platform, and right panels are bin-averaged values for the beach and the platform using a bin width of 0.5. Mean 95% confidence intervals on F^+ , calculated following the method outlined in Section 4.4.1, are ± 0.0005 $\text{m}^3 \text{s}^{-1}$ and ± 0.0007 $\text{m}^3 \text{s}^{-1}$ for the beach and platform, respectively.

The linear decrease in H_{SS} on both the beach and the platform provides evidence that all of the sensors were logging in the surf zone. Values of H_{SS} are quite similar on both sites, decreasing from $H_{SS} \approx 1.5\text{-}2.0$ m at $h = 4$ m, to $H_{SS} \approx 0.5$ m at $h < 0.5$ m. The slightly higher H_{SS} on the platform at $h > 2$ m reflects the slightly higher breaker index on the platform compared to the beach. The cross-shore trend in H_{inf} is also similar between the beach and the platform, decreasing from ~ 0.6 m to ~ 0.3 m whilst propagating from $h = 4$

m to $h = 0.5$ m. A clear reduction in F^+ can be seen for both sites and this is reflected in D^+ which is quite low until $h \approx 1.5$ m, after which it increases into shallow water. Mean D^+ at $h = 2.5-3.0$ m is $0.0001 \text{ m}^3 \text{ s}^{-1} \text{ m}^{-1}$ on both the beach and the platform, increasing to $0.0005 \text{ m}^3 \text{ s}^{-1} \text{ m}^{-1}$ and $0.0004 \text{ m}^3 \text{ s}^{-1} \text{ m}^{-1}$ at $h = 0.5-1.0$ m on the beach and platform, respectively.

The infragravity energy fluxes and dissipation rates that have been presented, as well as infragravity and sea-swell wave heights, convincingly suggest that there is no significant difference between the dissipation of infragravity waves, or indeed sea-swell waves, on the beach and the rocky shore platform. That is to say, the extreme roughness of the platform relative to the beach does not appear to cause any significant damping effect on the infragravity waves and both sites display hydrodynamic characteristics analogous to Perranporth and other dissipative beaches. To further verify the apparent lack of frictional dissipation on the platform and further demonstrate the similarities between the beach and the platform, the normalised bed slope parameter was calculated and is shown against the amplitude reflection coefficient in Figure 6.12. In calculating β_H , values for H^+ , T , and β are estimated as outlined in Section 5.2.3. Results for the beach replicate closely those of Perranporth with R in the frequency bands 0.017-0.028 Hz and 0.028-0.04 Hz showing an increase with β_H and averaging 0.37 ($R^2 = 0.14$) and 0.28 ($R^2 = 0.08$), respectively. Values of R in the frequency band 0.005-0.017 Hz, however, show evidence of levelling off for $\beta_H > 3-4$, with a mean R of 0.66 ($R^2 = 0.43$). Following Van Dongeren et al. (2007), these results place frequencies < 0.017 Hz in the steep sloping regime where waves undergo high levels of reflection, whereas waves with frequencies > 0.017 Hz are in the mild sloping regime making them liable to dissipation by breaking. Data from the platform yield similar results with amplitude reflection coefficients of 0.55 ($R^2 = 0.30$), 0.30 ($R^2 = 0.09$), and 0.24 ($R^2 = 0.06$) for the frequency bands 0.005-0.017 Hz, 0.017-

0.028 Hz, and 0.028-0.04 Hz, respectively. Though less clear, increases in R appear to plateau around $\beta_H \approx 3-4$, as with the beach.

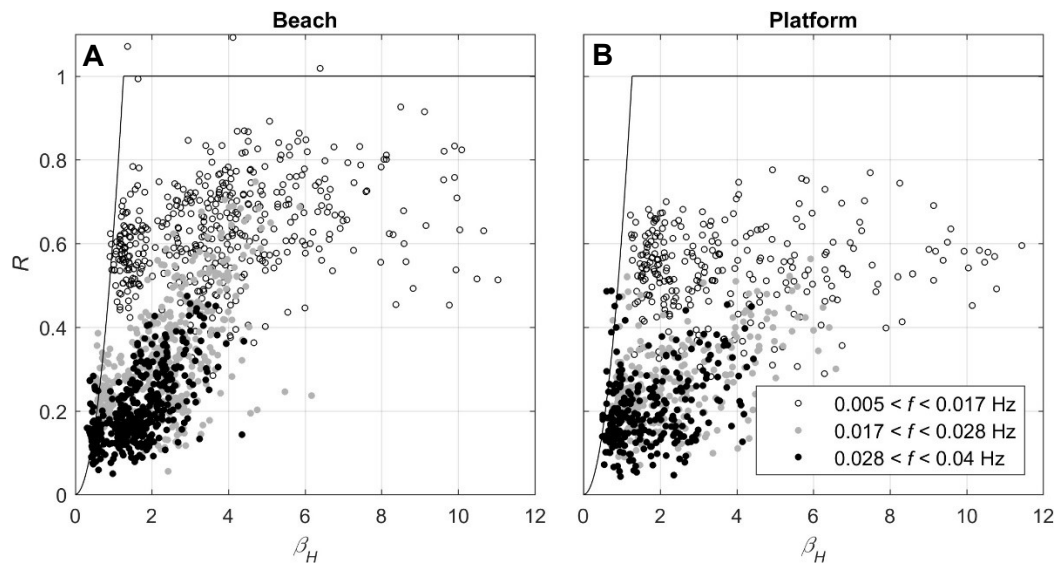


Figure 6.12. Bulk amplitude reflection coefficients R for partitioned infragravity bands versus the normalised bed slope parameter β_H for the beach (A) and platform (B). The solid black lines are $\min(1, R = 0.2\pi\beta_H^2)$, following Van Dongeren et al. (2007). Maximum 95% confidence intervals on beach values of R , calculated following the method outlined in Section 4.3.2, are ± 0.05 , ± 0.01 , and ± 0.004 for the frequency ranges 0.005-0.017 Hz, 0.017-0.028 Hz, and 0.028-0.04 Hz, respectively. The same confidence intervals for the platform values of R are ± 0.02 , ± 0.009 , and ± 0.008 , respectively.

These results provide an indication that the dominant dissipation mechanism of infragravity waves on the rocky shore platform is the same as that of the sandy beach and is most likely infragravity wave breaking, influenced by the gentle platform slope rather than its roughness characteristics. Numerical modelling by Poate et al. (under review) showed that bed friction only plays a significant role in sea-swell wave dissipation on very rough, flat platforms during small (< 0.5 m) wave conditions. Even under these idealised conditions, bed friction was found to account for only $\sim 20\%$ of the observed energy loss. Assuming that these conditions also apply to infragravity wave dissipation, these conditions were not met at Freshwater West since, whilst the platform is very rough, the platform gradient can only marginally be classified as flat and the wave heights

observed in the present study (both sea-swell and infragravity) were predominantly >0.5 m. In contrast, the study by Pomeroy et al. (2012), which concluded that bed friction was the dominant infragravity dissipation mechanism, took place on a flat, hydraulically rough coral reef with sea-swell and infragravity wave heights <0.3 m, thus fulfilling the conditions outlined by Poate et al. (under review). Whereas the study by Cheriton et al. (2016) took place on a relatively smooth reef under very energetic forcing ($H_o = 6$ m, $T_p = 16$ s), thus not meeting the conditions for bed friction, and they observed skewed and asymmetrical, bore-like infragravity waves that suggest breaking.

6.3 Conclusion

The first simultaneous observations of infragravity wave transformation on a Type A rocky shore platform ($\beta \approx 0.018$) and gently sloping sandy beach ($\beta \approx 0.011$) are presented. Despite the much higher level of roughness on the platform compared to the beach ($K_\sigma = 0.14$ and 0.01 , respectively), results for moderate to high energy conditions show that infragravity wave characteristics, and indeed sea-swell waves, are very similar across the two sites. Sea-swell wave height is only slightly different on the platform and this can be explained by the slightly steeper bed slope and is well predicted using formulations derived for sandy beaches. Infragravity waves dissipate considerably in the inner surf zone at rates that are not significantly different between the beach and the platform, showing that frictional dissipation due to platform roughness is a secondary dissipation mechanism at best. The relationship between R and β_H , and similarities with results of the Perranporth field experiment presented in Chapter 5, indicate that wave breaking is the dominant dissipation mechanism of medium to high frequency infragravity waves. These findings are in contrast to some other studies, mostly on flat coral reefs, where considerable frictional dissipation has been reported under predominantly low energy forcing conditions. Overall, offshore wave conditions and bed slope appear to be more

important than bed roughness in controlling infragravity wave behaviour on a Type A shore platform, at least under moderate to high energy forcing.

The difference in infragravity response to offshore forcing between Freshwater West and Perranporth is intriguing, showing that the level of infragravity energy close to shore at Perranporth is significantly larger than at Freshwater West under the same level of $H_o^2 T_p$. Though unresolved, this is an important issue that warrants further investigation and may require data from a range of study sites and environmental conditions to address fully.

Chapter 7

Discussion and conclusion

The fundamental aim of this study has been to improve the quantitative understanding of cross-shore infragravity wave dynamics on sandy beaches and rocky shore platforms. This chapter will bring together the different components that have been studied to address this aim and critically examines the findings in light of the previous state of the subject as outlined in Chapter 2. Suggestions for further infragravity wave research are also made. This is followed by the overall conclusions of the thesis.

7.1 Discussion and wider context

7.1.1 Noise correction in wave reflection analysis

The process of separating a wave signal into its incident and reflected components is an integral part of any study investigating the propagation and potential dissipation of infragravity waves. The results presented in Chapter 4 have shown that uncorrelated signal noise can introduce a significant positive bias to estimated incident and reflected spectra, and corresponding reflection coefficients, when an array method is used. This is the first time such an analysis has been performed using an array reflection method. The bias effects induced by uncorrelated noise were first noted in a provisional investigation by Huntley et al. (1999) using two PUV methods. However, many of the existing aspects of infragravity wave research that are in need of further study require spatially dense measurements in transects extending from the shoaling zone to the shore. This is far more achievable, both logistically and economically, using an array of pressure sensors as opposed to co-located pressure and velocity sensors, hence array methods of wave reflection analysis are likely to see more widespread use in the future.

The mathematical function that is developed to correct for noise induced bias is shown to be extremely effective, reducing bias by >90%. Applying the correction function to field data implies that infragravity reflection coefficients may be overestimated by more than 50% if noise is unaccounted for and high infragravity frequencies are most severely impacted since the level of reflection here is already low. For example, reflection coefficients associated with the Perranporth field experiment presented in Chapter 5 averaged 0.42 and 0.06 for the frequency bands 0.005-0.017 Hz and 0.028-0.040 Hz, respectively, but without applying the correction function these reflection coefficients would be 0.55 and 0.19, respectively.

This implies that levels of infragravity wave dissipation reported by studies using an array method (e.g., Battjes et al., 2004; Van Dongeren et al., 2007; De Bakker et al., 2014) may be underestimated and that the observed frequency-dependence may be even more striking. This could have further ramifications such as determining the frequency transition between mild and steep sloping regimes, and thus the frequency at which infragravity waves begin to break. Overall, these findings show that future investigations into the dissipation and reflection of infragravity waves must acknowledge and correct for the impact of noise to avoid potentially significant errors when decomposing infragravity motion into its incident and reflected components.

The derivation of a correction function for the array method of Van Dongeren et al. (2007) using the exact same methodology (Appendix A) demonstrates that (1) the problem of noise is not a method specific problem but most likely impacts all array methods, and (2) coherence acts as an excellent proxy for noise and should allow a correction function to be developed for any array method, using the methodology developed in this research. Despite being used in this study to accurately estimate incident and reflected infragravity wave spectra, the correction function is applicable to any frequency range, assuming that

the array is set-up appropriately for the frequencies of interest. This means that the technique is not limited to infragravity wave research but can be applied in other fields such as wave reflection from coastal structures in deep water.

The results of this work pair well with the study by Baldock and Simmonds (1999) who investigated the error on wave reflection estimates if array methods designed for use on horizontal beds are not modified for wave shoaling when used on sloping bathymetry. The influence of oblique wave angles and directional spreading, despite being addressed briefly in Chapter 4, warrants further study in spite of results showing minimal impact for all but the most extreme cases.

7.1.2 Infragravity waves during swell and wind-sea

Longuet-Higgins and Stewart (1962) and Hasselmann (1962) demonstrated theoretically that the coupling between pairs of sea-swell waves is stronger under narrow-banded wave spectra, and this has been confirmed in the field (e.g., Elgar and Guza, 1985). It is well known that long period swell is typically narrow-banded compared to short period wind-sea; hence, it is surprising that more studies have not included offshore wave period in parameterizing the nearshore infragravity response. The importance of wave period has been demonstrated here through the forcing parameter $H_o^2 T_p$ which is proportional to the offshore sea-swell energy flux and so has arguably more physical justification than other proposed forcing parameters that include wave period. Comparison of the results with previous studies undertaken on low fetch coastlines further demonstrates the importance of long period swell in forcing high energy infragravity waves. For example, De Bakker et al. (2014) measured maximum infragravity energy fluxes of $\sim 0.05 \text{ m}^3 \text{ s}^{-1}$ with an offshore wave height of around 3 m and a wave period of 6.8 s. In the present study, under a similar offshore wave height but with a wave period of 15.4 s, maximum energy fluxes were larger by a factor of three at $\sim 0.15 \text{ m}^3 \text{ s}^{-1}$. The larger infragravity energy levels

observed during long period swell compared to short period wind-sea implies that infragravity waves are more likely to affect morphological change on fetch-unlimited coastlines, including erosion, than on fetch-limited coasts. As such, knowledge of infragravity wave dynamics gathered from energetic, fetch-unlimited coasts is crucial, especially since it has been demonstrated here that dissipation rates are also a function of the relative dominance of swell and wind-sea components.

Perhaps the most intriguing aspect of these results is the difference in H_{inf} response to $H_o^2 T_p$ between Perranporth and Freshwater West. With similar levels of $H_o^2 T_p$ and no significant difference in spectral shape, it seems that another variable is at play here, perhaps a hydrodynamic subtlety that is not immediately evident from the wave spectra, or possibly related to morphodynamic variations between the two sites. To investigate this further, data from a variety of beach types and forcing conditions would be required. Furthermore, a high number of pressure sensors extending from the surf zone to the shoaling zone would allow the generation process of the infragravity waves to be explored in detail. In particular, the phase lag between the wave group envelope and the infragravity waves, responsible for energy transfer to infragravity frequencies, may be an important factor but is lacking in field observations, particularly during very high energy conditions, due largely to difficulties in deploying instruments in the subtidal zone.

The parameterization of H_{inf} close to shore with $H_o^2 T_p$ provides a useful first order estimate of the amount of infragravity energy reaching the shore. However, to accurately represent infragravity waves in wave propagation and shoreline evolution models, information about the shoreward transformation of infragravity waves is required. In Chapters 5 and 6, strong frequency-dependent infragravity dissipation is observed, thus extending the findings of recent field studies (e.g., Guedes et al., 2013; De Bakker et al., 2014) to a wider range of forcing conditions. The influence of offshore wave conditions

(i.e., swell and wind-sea) on infragravity dissipation has not yet been discussed in the literature. However, it was demonstrated in Chapter 5 that the dissipation rate of infragravity waves increases with more energetic offshore forcing. Although saturation of H_{inf} with $H_o^2 T_p$ was not observed herein, increasing infragravity dissipation rates with $H_o^2 T_p$ could be a sign of the pending emergence of infragravity saturation and could provide a physical explanation for the infragravity saturation observed by other studies (e.g., Ruessink et al., 1998; Ruggiero et al., 2004; Senechal et al., 2011).

Results from both Perranporth and Freshwater West indicate that wave breaking is the dominant infragravity wave dissipation mechanism, through the application of bispectral analysis and the normalised bed slope parameter. These observations from energetic, long period swell conditions extend the findings from laboratory (Battjes et al., 2004; Van Dongeren et al., 2007; De Bakker et al., 2015), modelling (Ruju et al., 2012), and field studies on low fetch coastlines (De Bakker et al., 2014). We are now able to say with confidence that infragravity waves dissipate their energy primarily through breaking on gentle slopes. Nonetheless, further investigation into the surf zone location of infragravity wave breaking and the transition frequency between breaking and reflection in relation to beach slope is required to truly understand the infragravity wave breaking process. High-resolution data, both spatially and temporally, are required over a large cross-shore extent to address this thoroughly.

The influence of offshore forcing and the main changes that infragravity waves undergo as they propagate shoreward through the surf zone, as described in this section, are summarised in the conceptual model shown in Figure 7.1.

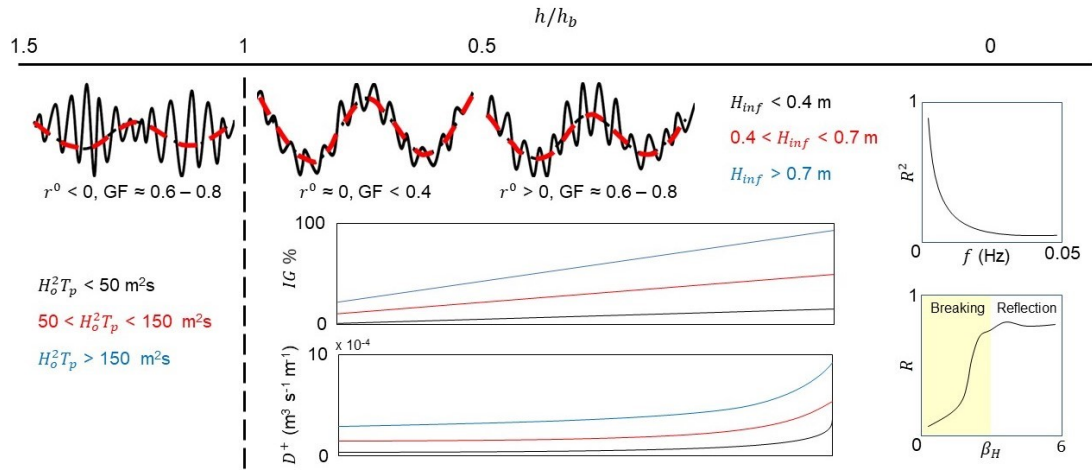


Figure 7.1. Conceptual model illustrating the change in infragravity wave characteristics with changing cross-shore location relative to the surf zone. In the top part of the figure, the black and red (dashed) wave trains represent the sea-swell waves and infragravity motion, respectively. Elsewhere, blue, red, and black colours represent high ($H_o^2 T_p > 150 \text{ m}^2\text{s}$), medium ($50 < H_o^2 T_p < 150 \text{ m}^2\text{s}$), and low ($H_o^2 T_p < 50 \text{ m}^2\text{s}$) levels of offshore forcing, respectively. For a full glossary of the symbols used in the figure, refer to the List of symbols and abbreviations on page xix. The values corresponding to various parameters are approximate and provided as a guide.

7.1.3 Implications for sediment transport

The significant contribution of infragravity waves to surf and swash zone hydrodynamics has led to a large number of studies investigating the suspension and cross-shore transport of sediment by infragravity waves dating back to the 1980s. However, these studies have reported contrasting results in relation to the direction and relative importance of infragravity sediment transport, partly owing to the range of offshore wave conditions and beach slopes.

The latest, ‘state-of-the-art’ study by De Bakker et al. (2016b) proposes that the cross-shore sediment transport direction due to infragravity waves, and the reasoning behind past contrasting observations, can be explained by the ratio of infragravity wave height to sea-swell wave height H_{inf}/H_{SS} . They suggest that, in the inner surf zone of gently sloping beaches where infragravity waves can be very energetic, sediment transport by infragravity waves is offshore directed if $H_{inf}/H_{SS} > 0.4$ (Figure 7.2A), regardless of the

local sea-swell waves. Under this scenario, seaward infragravity sediment transport accounted for up to 60% of the total cross-shore transport. Further seaward, where $0.25 < H_{inf}/H_{ss} < 0.4$ and the largest sea-swell waves tend to occur on infragravity wave crests, infragravity sediment transport tends to be onshore directed.

Figure 7.2B-D shows H_{inf}/H_{ss} as a function of h and $H_o^2 T_p$ during the Perranporth and Freshwater West (beach and platform) field experiments. For $h < 0.5$ m, H_{inf}/H_{ss} is entirely > 0.4 at all three sites, implying that infragravity sediment transport is always offshore directed in the very inner surf zone. Moreover, whilst H_{inf}/H_{ss} is typically < 0.4 where $h > 1$ m during low energy conditions, under the most energetic conditions ($H_o^2 T_p \geq 200$; green-yellow dots) H_{inf}/H_{ss} was > 0.4 from as far out as $h \approx 4-5$ m. Following the conceptual model of De Bakker et al. (2016b), this indicates that offshore directed sediment transport due to infragravity waves may occur over a very wide cross-shore extent extending into relatively deep water during very energetic forcing conditions.

Interestingly, during the field experiment on a gently sloping beach from which De Bakker et al.'s (2016) conceptual model is based, values of H_{inf}/H_{ss} were predominantly < 0.5 despite H_o exceeding 4 m. In contrast, H_{inf}/H_{ss} values > 0.5 account for 31%, 33%, and 52% of all H_{inf}/H_{ss} values at Perranporth and Freshwater West (beach and platform), respectively. Since the De Bakker et al. (2016b) experiment took place on a low fetch beach in the Netherlands with a maximum offshore wave period of 7.0 s, this further demonstrates the importance of wave period in nearshore infragravity wave dynamics, including sediment transport. Measurements of suspended sediment concentration and velocity are required to test the applicability of De Bakker et al.'s (2016b) conceptual model to conditions of high energy, long period swell and storms. However, the evidence presented here suggests that infragravity waves likely contribute significantly and

regularly to the offshore transport of sediment across the surf zone during energetic conditions.

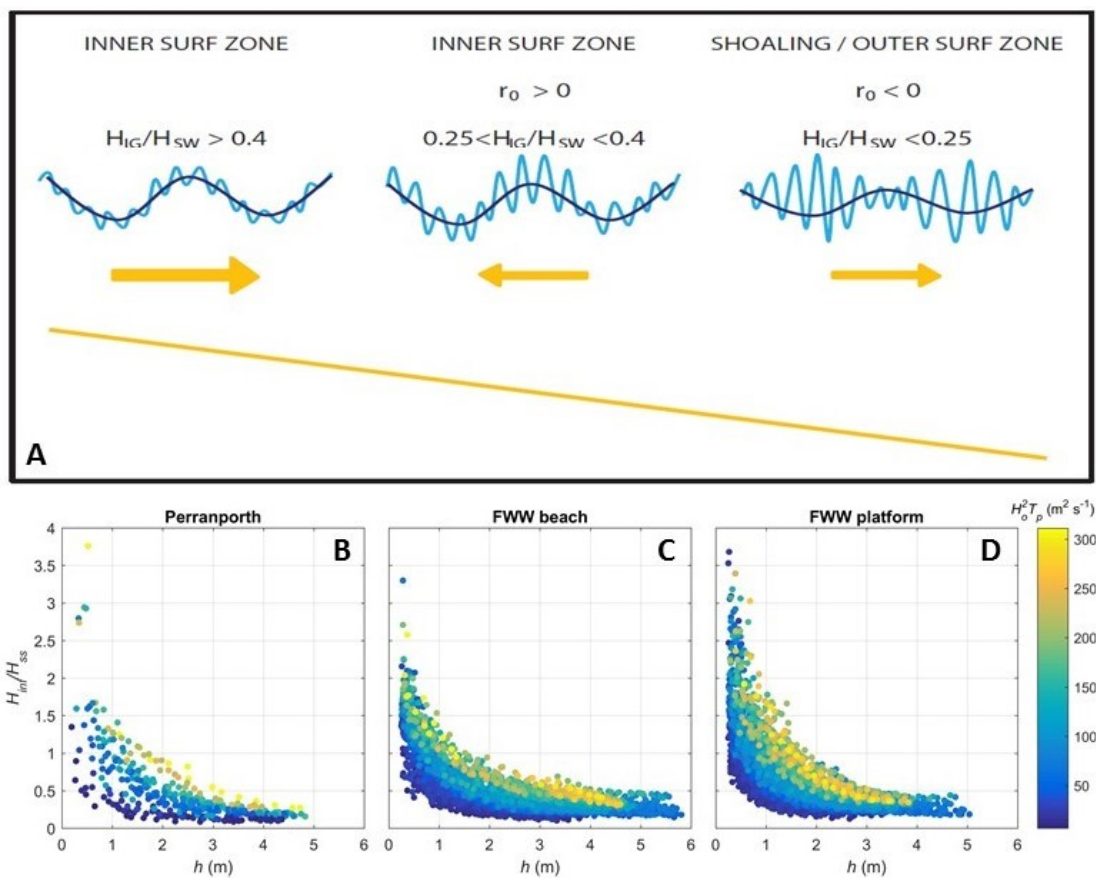


Figure 7.2. Conceptual figure for sand suspension mechanisms and resulting transport directions for a gently sloping beach, from De Bakker et al. (2016b) (A). Ratio of infragravity wave height to sea-swell wave height H_{inf}/H_{ss} versus water depth h at Perranporth (B), Freshwater West beach (C), and Freshwater West platform (D). Colour in (B-D) represents $H_0^2 T_p$.

7.1.4 Infragravity waves and bed roughness

The unique dataset analysed in Chapter 6 represents the most extensive field dataset of infragravity waves on a rocky shore platform, both in terms of environmental conditions and experimental set-up, and it is the first time infragravity waves have been measured simultaneously on a rocky shore platform and adjacent sandy beach. Therefore, these results are original and make a significant contribution to the infragravity wave and rocky coast literature.

Previous studies on Type B shore platforms have not reported infragravity wave dissipation or alluded to potential dissipation mechanisms, with most observing a shoreward increase in infragravity energy (e.g., Beetham and Kench, 2011; Marshall and Stephenson, 2011; Ogawa et al., 2011). Whereas, a small number of studies on coral reefs (e.g., Pomeroy et al., 2012; Pequignet et al., 2014) have reported that bed friction is the primary infragravity dissipation mechanism, in contrast to the results presented here which show no significant difference between the beach and the platform, thus no accelerated dissipation due to the increased roughness of the platform.

Numerical modelling by Poate et al. (under review) found that for bed friction to play an important role in sea-swell wave dissipation, the bed has to be very rough and flat and wave height must be small (<0.5 m). Although this was determined for sea-swell waves, for which the results herein agree well, similarities of infragravity wave dynamics between the beach and the platform, as well as with Perranporth, show that these criteria may well apply to infragravity waves. This is supported by the fact that past studies that have reported frictional dissipation of infragravity waves have done so using data from rough and flat reefs and predominantly low energy conditions (e.g., Pomeroy et al., 2012; Pequignet et al., 2014). Furthermore, the study by Cheriton et al. (2016) was undertaken in storm conditions ($H_o >6$ m), thus not meeting the above criteria, and did not report dissipation due to bed friction but rather provided evidence suggestive of infragravity wave breaking. Water depth has also been shown to influence bed friction effects in previous studies (e.g., Pequignet et al., 2009; Van Dongeren et al., 2013), with higher rates of frictional dissipation in shallow water. Dissipation rates on the Freshwater West platform are highest in shallow water, but this is also true for both the Freshwater West beach and at Perranporth, indicating that this is not due to bed friction. Similarities between the three study sites in this thesis indicate that bed slope and offshore forcing are the main controls on nearshore infragravity energy levels and dissipation patterns during

moderate-high energy conditions. Further research on a range of shore platforms and during all levels of offshore forcing are required to assess the generality of these findings and to confirm whether or not bed roughness plays a role in infragravity dissipation, but the results here strongly suggest not. Regardless of the role of bed friction, the findings from the platform at Freshwater West are important for rocky coast geomorphology and shoreline modelling, since they show that, like dissipative beaches, infragravity waves dominate the water motion at the shoreline and thus likely play a significant role in cliff erosion and the removal of cliff toe debris.

7.2 Thesis conclusions

This thesis aimed to improve the quantitative understanding of cross-shore infragravity wave dynamics on sandy beaches and rocky shore platforms. For the purposes of this investigation, a new analysis tool was developed to provide an accurate decomposition of reflective wave fields. The main conclusions from this aspect of the work were:

- Incident and reflected wave spectra, and corresponding reflection coefficients, experience a significant positive bias as a result of uncorrelated signal noise. The quantity of this bias can exceed 100% for low signal-to-noise ratios. Accordingly, any analysis involving the decomposition of a reflective wave field into its incident and reflective components should acknowledge and account for the presence of noise.
- Coherence acts as a good proxy for signal noise and is used to develop a mathematical correction function. This correction function is effective at reducing noise induced bias by up to 90% and can be developed for any reflection analysis technique whereby an array of wave sensors is used. Further, confidence intervals on corrected incident and reflected spectra are estimated as a function of the coherence and degrees of freedom.

With reference to infragravity waves during a range of swell and wind-sea conditions, the main conclusions to be drawn are:

- Infragravity wave height close to shore is best predicted using a parameter that incorporates wave period, specifically $H_o^2 T_p$, which represents the short wave energy flux, rather than wave height alone. Offshore wave spectra are shown to be much narrower banded under high wave periods and, as such, coupling between sea-swell waves resulting in the transfer of energy to infragravity frequencies is stronger.
- Infragravity waves dissipate strongly in the surf zone, beginning shoreward of the short wave breakpoint where the bound waves are fully released. The rate of infragravity dissipation increases with increasing frequency and with $H_o^2 T_p$ (i.e., the short wave energy flux and hence the magnitude of infragravity energy). The latter is a sign of proto-saturation of the infragravity waves.
- The shoreline reflection of infragravity waves with frequencies >0.017 Hz is very low and the dependence of these frequencies on a normalised bed slope parameter places them in a mild sloping regime. This is indicative of infragravity wave breaking, which is further supported by the results of bispectral analysis showing predominantly infragravity-infragravity interactions in shallow water and the development of infragravity harmonics.

This thesis has presented the first in depth measurements of infragravity waves on a rocky shore platform, from which it is concluded that:

- Extreme bed roughness does not significantly accelerate the dissipation of infragravity waves, or indeed sea-swell waves. Infragravity waves on macrotidal shore platforms behave analogously to those on dissipative sandy beaches, showing

that bed slope and the level of forcing ($H_o^2 T_p$) are more important to infragravity wave dynamics than bed roughness during moderate-high energy conditions.

References

- Ardhuin, F., Rawat, A., Aucan, J. 2014. A numerical model for free infragravity waves: Definition and validation at regional and global scales. *Ocean Modelling*, 77, 20-32.
- Aucan, J., Ardhuin, F. 2013. Infragravity waves in the deep ocean: An upward revision. *Geophysical Research Letters*, 40, 3435-3439.
- Austin, M., Scott, T., Brown, J., Brown, J., MacMahan, J., Masselink, G., Russell, P. 2010. Temporal observations of rip current circulation on a macro-tidal beach. *Continental Shelf Research*, 30, 1149-1165.
- Austin, M.J., Scott, T.M., Russell, P.E., Masselink, G. 2013. Rip current prediction: development, validation, and evaluation of an operational tool. *Journal of Coastal Research*, 29, 283-300.
- Baldock, T.E. 2012. Dissipation of incident forced long waves in the surf zone – implications for the concept of “bound” wave release at short wave breaking. *Coastal Engineering*, 60, 276-285.
- Baldock, T.E., Huntley, D.A., Bird, P.A.D., O’Hare, T., Bullock, G.N. 2000. Breakpoint generated surf beat induced by bichromatic wave groups. *Coastal Engineering*, 39, 213-242.
- Baldock, T.E., Huntley, D.A. 2002. Long-wave forcing by the breaking of random gravity waves on a beach. *Proceedings of the Royal Society of London A*, 458, 2177-2201.
- Baldock, T.E., O’Hare, T.J. 2004. Energy transfer and dissipation during surf beat conditions. *Proceedings of the 29th Conference on Coastal Engineering*. World Scientific, New Jersey.
- Baldock, T.E., Simmonds, D.J. 1999. Separation of incident and reflected waves over sloping bathymetry. *Coastal Engineering*, 38, 167-176.
- Battjes, J.A. 1974. Surf similarity. *Proceedings of the 14th Conference on Coastal Engineering*. ASCE, New York.
- Battjes, J.A., Bakkenes, H.J., Janssen, T.T., van Dongeren, A.R. 2004. Shoaling of subharmonic gravity waves. *Journal of Geophysical Research*, 109, C02009.
- Becker, J.M., Merrifield, M.A., Yoon, H. 2016. Infragravity waves on fringing reefs in the tropical Pacific: Dynamic setup. *Journal of Geophysical Research*, 121, 3010-3028.

- Beetham, E.P., Kench, P.S. 2011. Field observations of infragravity waves and their behaviour on rock shore platforms. *Earth Surface Processes and Landforms*, 36, 1872-1888.
- Bertin, X., Prouteau, E., Letetrel, C. 2013. A significant increase in wave height in the North Atlantic Ocean over the 20th century. *Global and Planetary Change*, 106, 77-83.
- Biéssel, F. 1952. Équations générales au second ordre de la houle irrégulière. *La Houille Blanche*, 7, 372-376.
- Bird, E.C.F. 2000. *Coastal geomorphology: an introduction*. Wiley, Chichester.
- Brander, R.W., Kench, P.S., Hart, D. 2004. Spatial and temporal variations in wave characteristics across a reef platform, Warraber Island, Torres Strait, Australia. *Marine Geology*, 207, 169-184.
- Centre for Environment, Fisheries, and Aquaculture Science (CEFAS). 2017. *WaveNet*. Available at: <https://www.cefas.co.uk/cefas-data-hub/wavenet/> [Accessed 18 April 2017].
- Channel Coastal Observatory (CCO). 2017. *Regional Coastal Monitoring Programmes: Perranporth*. Available at: http://www.channelcoast.org/data_management/real_time_data/charts/?chart=76&tab=waves&disp_option [Accessed 18 April 2017].
- Cheriton, O.M., Storlazzi, C.D., Rosenberger, K.J. 2016. Observations of wave transformation over a fringing coral reef and the importance of low-frequency waves and offshore water levels to runup, overwash, and coastal flooding. *Journal of Geophysical Research*, 121, 3121-3140.
- Collis, W.B., White, P.R., Hammond, J.K. 1998. Higher-order spectra: the bispectrum and trispectrum. *Mechanical Systems and Signal Processing*, 12, 375-394.
- Contardo, S., Symonds, G. 2013. Infragravity response to variable wave forcing in the nearshore. *Journal of Geophysical Research*, 118, 7095-7106.
- Crawford, W., Ballu, V., Bertin, X., Karpytchev, M. 2015. The sources of deep ocean infragravity waves observed in the North Atlantic Ocean. *Journal of Geophysical Research*, 120, 5120-5133.
- De Bakker, A.T.M., Tissier, M.F.S., Ruessink, B.G. 2014. *Shoreline dissipation of infragravity waves*. *Continental Shelf Research*, 72, 73-82.

- De Bakker, A.T.M., Herbers, T.H.C., Smit, P.B., Tissier, M.F.S., Ruessink, B.G. 2015. Nonlinear infragravity-wave interactions on a gently sloping laboratory beach. *Journal of Physical Oceanography*, 45, 589-605.
- De Bakker, A.T.M., Tissier, M.F.S., Ruessink, B.G. 2016a. Beach steepness effects on nonlinear infragravity-wave interactions: a numerical study. *Journal of Geophysical Research*, 121, 554-570.
- De Bakker, A.T.M., Brinkkemper, J.A., Van Der Steen, F., Tissier, M.F.S., Ruessink, B.G. 2016b. Cross-shore sand transport by infragravity waves as a function of beach steepness. *Journal of Geophysical Research*, 121, 1786-1799.
- Dickson, M.E., Pentney, R. 2012. Micro-seismic measurements of cliff motion under wave impact and implications for the development of near-horizontal shore platforms. *Geomorphology*, 151, 27-38.
- Dickson, M.E., Ogawa, H., Kench, P.S., Hutchinson, A. 2013. Sea-cliff retreat and shore platform widening: steady-state equilibrium? *Earth Surface Processes and Landforms*, 38, 1046-1048.
- Dodet, G., Bertin, X., Taborda, R. 2010. Wave climate variability in the North-East Atlantic Ocean over the last six decades. *Ocean Modelling*, 31, 120-131.
- Donat, M.G., Renggli, D., Wild, S., Alexander, L.V., Leckebusch, G.C., Ulbrich, U. 2011. Reanalysis suggests long-term upward trends in European storminess since 1871. *Geophysical Research Letters*, 38, L14703.
- Dong, G., Ma, X., Xu, J., Ma, Y., Wang, G. 2009. Experimental study of the transformation of bound long waves over a mild slope with ambient currents. *Coastal Engineering*, 56, 1035-1042.
- Elgar, S., Guza, R.T. 1985. Observations of bispectra of shoaling surface gravity waves. *Journal of Fluid Mechanics*, 161, 425-448.
- Elgar, S., Herbers, T.H.C., Okihiro, M., Oltman-Shay, J., Guza, R.T. 1992. Observations of infragravity waves. *Journal of Geophysical Research*, 97, 15573-15577.
- Emery, K.O., Kuhn, G.C. 1982. Sea cliffs: their processes, profiles, and classification. *Geological Society of America Bulletin*, 93, 644-654.
- Fiedler, J.W., Brodie, K.L., McNinch, J.E., Guza, R.T. 2015. Observations of runup and energy flux on a low-slope beach with high-energy, long-period ocean swell. *Geophysical Research Letters*, 42, 9933-9941.

- Frigaard, P., Brorsen, M. 1995. A time-domain method for separating incident and reflected irregular waves. *Coastal Engineering*, 24, 205-215.
- Gaillard, P., Gauthier, M., Holly, F. 1980. Method of analysis of random wave experiments with reflecting coastal structures. *Proceedings of the 17th Conference on Coastal Engineering*. ASCE, New York.
- Garrett, C.J.R., Toulany, B. 1981. Variability of the flow through the Strait of Belle Isle. *Journal of Marine Research*, 39, 163-189.
- Goda, Y., Suzuki, Y. 1976. Estimation of incident and reflected waves in random wave experiments. *Proceedings of the 15th Conference on Coastal Engineering*. ASCE, New York.
- Guedes, R.M.C., Bryan, K.R., Coco, G. 2013. Observations of wave energy fluxes and swash motions on a low-sloping, dissipative beach. *Journal of Geophysical Research*, 118, 3651-3669.
- Guza, R.T., Bowen, A.J. 1976. Resonant interactions for waves breaking on a beach. *Proceedings of the 15th Conference on Coastal Engineering*. ASCE, New York.
- Guza, R.T., Thornton, E.B. 1982. Swash oscillations on a natural beach. *Journal of Geophysical Research*, 87, 483-491.
- Guza, R.T., Thornton, E.B. 1985. Observations of surf beat. *Journal of Geophysical Research*, 90, 3161-3172.
- Hasselmann, K. 1962. On the non-linear energy transfer in a gravity-wave spectrum: Part 1. General theory. *Journal of Fluid Mechanics*, 12, 481-500.
- Hasselmann, K., Munk, W., MacDonald, G. 1963. Bispectra of ocean waves. In *Time Series Analysis*, M. Rosenblatt (Ed.). John Wiley, New York. pp. 125-139.
- Haubrich, R.A. 1965. Earth noise, 5 to 500 millicycles per second: 1. Spectral stationarity, normality, and nonlinearity. *Journal of Geophysical Research*, 70, 1415-1427.
- Henderson, S.M., Bowen, A.J. 2002. Observations of surf beat forcing and dissipation. *Journal of Geophysical Research*, 107, 3193.
- Henderson, S.M., Elgar, S., Bowen, A.J. 2000. Observations of surf beat propagation and energetics. *Proceedings of the 27th Conference on Coastal Engineering*. ASCE, New York.

- Henderson, S.M., Guza, R.T., Elgar, S., Herbers, T.H.C., Bowen, A.J. 2006. Nonlinear generation and loss of infragravity wave energy. *Journal of Geophysical Research*, 111, C12007.
- Herbers, T.H.C., Elgar, S., Guza, R.T. 1994. Infragravity-frequency (0.005-0.05 Hz) motions on the shelf. Part 1: forced waves. *Journal of Physical Oceanography*, 24, 917-927.
- Herbers, T.H.C., Elgar, S., Guza, R.T. 1995. Generation and propagation of infragravity waves. *Journal of Geophysical Research*, 100, 24863-24872.
- Herbers, T.H.C., Russnogle, N.R., Elgar, S. 2000. Spectral energy balance of breaking waves within the surf zone. *Journal of Physical Oceanography*, 30, 2723-2737.
- Holman, R.A. 1981. Infragravity energy in the surf zone. *Journal of Geophysical Research*, 86, 6442-6450.
- Holman, R.A., Sallenger Jr, A.H. 1985. Setup and swash on a natural beach. *Journal of Geophysical Research*, 90, 945-953.
- Hughes, S.A. 1993. *Physical models and laboratory techniques in coastal engineering*. World Scientific, Singapore.
- Huntley, D.A., Guza, R.T., Thornton, E.B. 1981. Field observations of surf beat: 1. Progressive edge waves. *Journal of Geophysical Research*, 86, 6451-6466.
- Huntley, D.A., Kim, C.S. 1984. Is surf beat forced or free? *Proceedings of the 19th Conference on Coastal Engineering*. ASCE, New York.
- Huntley, D.A., Simmonds, D., Tatavarti, R. 1999. Use of collocated sensors to measure coastal wave reflection. *Journal of Waterway, Port, Coastal, and Ocean Engineering*, 125, 46-52.
- Inch, K., Masselink, G., Puleo, J.A., Russell, P., Conley, D.C. 2015. Vertical structure of near-bed cross-shore flow velocities in the swash zone of a dissipative beach. *Continental Shelf Research*, 101, 98-108.
- Inch, K., Davidson, M., Masselink, G., Russell, P. 2017. Correcting wave reflection estimates in the coastal zone. *Coastal Engineering*, 119, 65-71.
- Inch, K., Davidson, M., Masselink, G., Russell, P. 2017. Observations of nearshore infragravity wave dynamics under high energy swell and wind-wave conditions. *Continental Shelf Research*, 138, 19-31.

- Janssen, T.T., Battjes, J.A., Van Dongeren, A.R. 2003. Long waves induced by short-wave groups over a sloping bottom. *Journal of Geophysical Research*, 108, 3252.
- Jenkins, G.M., Watts, D.G. 1968. *Spectral analysis and its applications*. Holden-Day, San Francisco.
- Kim, Y., Powers, E. 1979. Digital bispectral analysis and its applications to nonlinear wave interactions. *IEEE Transactions on Plasma Science*, 7, 120-131.
- Knutson, T.R., McBride, J.L., Chan, J., Emanuel, K., Holland, G., Landsea, C., Held, I., Kossin, J.P., Srivastava, A.K., Sugi, M. 2010. Tropical cyclones and climate change. *Nature Geoscience*, 3, 157-163.
- Lin, Y.H., Hwung, H.H. 2012. Infra-gravity wave generation by the shoaling wave groups over beaches. *China Ocean Engineering*, 26, 1-18.
- Lippmann, T.C., Herbers, T.H.C., Thornton, E.B. 1999. Gravity and shear wave contributions to nearshore infragravity motions. *Journal of Physical Oceanography*, 29, 231-239.
- List, J.H. 1991. Wave groupiness variations in the nearshore. *Coastal Engineering*, 15, 475-496.
- List, J.H. 1992. A model for the generation of two-dimensional surf beat. *Journal of Geophysical Research*, 97, 5623-5635.
- Longuet-Higgins, M.S., Stewart, R.W. 1962. Radiation stress and mass transport in gravity waves with applications to 'surf beats'. *Journal of Fluid Mechanics*, 13, 481-504.
- Longuet-Higgins, M.S., Stewart, R.W. 1964. Radiation stresses in water waves; a physical discussion, with applications. *Deep Sea Research and Oceanographic Abstracts*, 11, 529-562.
- Longuet-Higgins, M.S. 1984. Statistical properties of wave groups in a random sea state. *Philosophical Transactions of the Royal Society of London Series A*, 312, 219-250.
- Lowe, R.J., Falter, J.L., Bandet, M.D., Pawlak, G., Atkinson, M.J., Monismith, S.G., Koseff, J.R. 2005. Spectral wave dissipation over a barrier reef. *Journal of Geophysical Research*, 110, C04001.
- Lugo-Fernandez, A., Roberts, H.H., Wiseman Jr, W.J., Carter, B.L. 1998. Water level and currents of tidal and infragravity periods at Tague Reef, St. Croix (USVI). *Coral Reefs*, 17, 343-349.

- Madsen, P.A., Sorensen, O.R., Schaffer, H.A. 1997. Surf zone dynamics simulated by a Boussinesq type model. Part II: surf beat and swash oscillations for wave groups and irregular waves. *Coastal Engineering*, 32, 289-319.
- Mansard, E.P.D., Funke, E.R. 1980. The measurement of incident and reflected spectra using a least squares method. *Proceedings of the 17th Conference on Coastal Engineering*. ASCE, New York.
- Marshall, R.J.E., Stephenson, W.J. 2011. The morphodynamics of shore platforms in a micro-tidal setting: interactions between waves and morphology. *Marine Geology*, 288, 18-31.
- Masselink, G. 1995. Group bound long waves as a source of infragravity energy in the surf zone. *Continental Shelf Research*, 15, 1525-1547.
- Masselink, G., Hegge, B. 1995. Morphodynamics of meso- and macrotidal beaches: examples from central Queensland, Australia. *Marine Geology*, 129, 1-23.
- Masselink, G., Austin, M., Scott, T., Poate, T., Russell, P. 2014. Role of wave forcing, storms and NAO in outer bar dynamics on a high-energy, macro-tidal beach. *Geomorphology*, 226, 76-93.
- Masselink, G., Castelle, B., Scott, T., Dodet, G., Suanez, S., Jackson, D., Floch, F. 2016a. Extreme wave activity during 2013/2014 winter and morphological impacts along the Atlantic coast of Europe. *Geophysical Research Letters*, 43, 2135-2143.
- Masselink, G., Scott, T., Poate, T., Russell, P., Davidson, M., Conley, D. 2016b. The extreme 2013/2014 winter storms: hydrodynamic forcing and coastal response along the southwest coast of England. *Earth Surface Processes and Landforms*, 41, 378-391.
- McGranahan, G., Balk, D., Anderson, B. 2007. The rising tide: assessing the risks of climate change and human settlements in low elevation coastal zones. *Environment and Urbanization*, 19, 17-37.
- Miles, J., Thorpe, A. 2015. Bedform contributions to cross-shore sediment transport on a dissipative beach. *Coastal Engineering*, 98, 65-77.
- Mitsuyasu, H., Tasai, F., Suhara, T., Mizuno, S., Ohkusu, M., Honda, T., Rikiishi, K. 1975. Observations of the directional spectrum of ocean waves using a cloverleaf buoy. *Journal of Physical Oceanography*, 5, 750-760.
- Morden, D.B., Richey, E.P., Christensen, D.R. 1976. Decomposition of co-existing random wave energy. *Proceedings of the 15th Conference on Coastal Engineering*. ASCE, New York.

- Munk, W.H. 1949. Surf beats. *Eos Transactions AGU*, 30, 849-854.
- Nakaza, E. 1991. Bore-like surf beat in a reef zone caused by wave groups of incident short period waves. *Fluid Dynamics Research*, 7, 89-100.
- Norheim, C.A., Herbers, T.H.C., Elgar, S. 1998. Nonlinear evolution of surface wave spectra on a beach. *Journal of Physical Oceanography*, 28, 1534-1551.
- Nutall, A.H. 1971. *Spectral estimation by means of overlapped FFT processing of windowed data*. Naval Underwater Systems Center (NUSC) Report No. 4169. New London, Connecticut.
- Ogawa, H., Dickson, M.E., Kench, P.S. 2011. Wave transformation on a sub-horizontal shore platform, Tatapouri, North Island, New Zealand. *Continental Shelf Research*, 31, 1409-1419.
- Ogawa, H., Kench, P., Dickson, M. 2012. Field measurements of wave characteristics on a near-horizontal shore platform, Mahia Peninsula, North Island, New Zealand. *Geographical Research*, 50, 179-192.
- Ogawa, H., Dickson, M.E., Kench, P.S. 2015. Hydrodynamic constraints and storm wave characteristics on a sub-horizontal shore platform. *Earth Surface Processes and Landforms*, 40, 65-77.
- Okiihiro, M., Guza, R.T., Seymour, R.J. 1992. Bound infragravity waves. *Journal of Geophysical Research*, 97, 11453-11469.
- Oltman-Shay, H., Howd, P.A., Birkemeier, W.A. 1989. Shear instabilities of the mean longshore current: 2. Field observations. *Journal of Geophysical Research*, 94, 18031-18042.
- Pequignet, A.C.N., Becker, J.M., Merrifield, M.A., Aucan, J. 2009. Forcing of resonant modes on a fringing reef during tropical storm Man-Yi. *Geophysical Research Letters*, 36, L03607.
- Pequignet, A.C.N., Becker, J.M., Merrifield, M.A. 2014. Energy transfer between wind waves and low-frequency oscillations on a fringing reef, Ipan, Guam. *Journal of Geophysical Research*, 119, 6709-6724.
- Poate, T., Masselink, G., Russell, P., Austin, M. 2014. Morphodynamic variability of high-energy macrotidal beaches, Cornwall, UK. *Marine Geology*, 350, 97-111.

- Poate, T., Masselink, T., Austin, M., Dickson, M., Kench, P. 2016. Observations of wave transformation on macro-tidal rocky platforms. *Journal of Coastal Research*, SI75, 602-606.
- Poate, T., Masselink, G., Austin, M.J., Dickson, M., McCall, R. under review. The role of bed roughness in wave transformation across sloping rock shore platforms. *Journal of Geophysical Research*.
- Pomeroy, A., Lowe, R., Symonds, G., van Dongeren, A., Moore, C. 2012. The dynamics of infragravity wave transformation over a fringing reef. *Journal of Geophysical Research*, 117, C11022.
- Prodger, S., Russell, P., Davidson, M., Miles, J., Scott, T. 2016. Understanding and predicting the temporal variability of sediment grain size characteristics on high-energy beaches. *Marine Geology*, 376, 109-117.
- Raubenheimer, B., Guza, R.T., Elgar, S. 1996. Wave transformation across the inner surf zone. *Journal of Geophysical Research*, 101, 25589-25597.
- Raubenheimer, B., Elgar, S., Guza, R.T. 1998. Estimating wave heights from pressure measured in sand bed. *Journal of Waterway, Port, Coastal, and Ocean Engineering*, 124, 151-154.
- Rijnsdorp, D.P., Ruessink, G., Zijlema, M. 2015. Infragravity-wave dynamics in a barred coastal region, a numerical study. *Journal of Geophysical Research*, 120, 4068-4089.
- Roelvink, D., Reniers, A., van Dongeren, A., van Thiel de Vries, J., McCall, R., Lescinski, J. 2009. Modelling storm impacts on beaches, dunes and barrier islands. *Coastal Engineering*, 56, 1133-1152.
- Ruessink, B.G. 1998a. The temporal and spatial variability of infragravity energy in a barred nearshore zone. *Continental Shelf Research*, 18, 585-605.
- Ruessink, B.G. 1998b. Bound and free infragravity waves in the nearshore zone under breaking and nonbreaking conditions. *Journal of Geophysical Research*, 103, 12795-12805.
- Ruessink, B.G., Kleinhan, M.G., van den Beukel, P.G.L. 1998. Observations of swash under highly dissipative conditions. *Journal of Geophysical Research*, 103, 3111-3118.
- Ruggiero, P., Holman, R.A., Beach, R.A. 2004. Wave run-up on a high-energy dissipative beach. *Journal of Geophysical Research*, 109, C06025.

- Ruju, A., Lara, J.L., Losada, I.J. 2012. Radiation stress and low-frequency energy balance within the surf zone: a numerical approach. *Coastal Engineering*, 68, 44-55.
- Russell, P.E. 1993. Mechanisms for beach erosion during storms. *Continental Shelf Research*, 13, 1243-1265.
- Sallenger, A.H., Holman, R.A. 1985. Wave energy saturation on a natural beach of variable slope. *Journal of Geophysical Research*, 90, 11939-11944.
- Schaffer, H.A. 1993. Infragravity waves induced by short-wave groups. *Journal of Fluid Mechanics*, 247, 551-588.
- Senechal, N., Coco, G., Bryan, K.R., Holman, R.A. 2011. Wave runup during extreme storm conditions. *Journal of Geophysical Research*, 116, C07032.
- Sheremet, A., Guza, R.T., Elgar, S., Herbers, T.H.C. 2002. Observations of nearshore infragravity waves: seaward and shoreward propagating components. *Journal of Geophysical Research*, 107, C8.
- Shimozono, T., Tajima, Y., Kennedy, A.B., Nobuoka, H., Sasaki, J., Sato, S. 2015. Combined infragravity wave and sea-swell runup over fringing reefs by super typhoon Haiyan. *Journal of Geophysical Research*, 120, 4463-4486.
- Shumway, R.H., Stoffer, D.S. 2000. *Time Series Analysis and Its Applications*. Springer, New York.
- Small, C., Nicholls, R.J. 2003. A global analysis of human settlement in coastal zones. *Journal of Coastal Research*, 19, 584-599.
- Stockdon, H.F., Holman, R.A., Howd, P.A., Sallenger Jr., A.H. 2006. Empirical parameterization of setup, swash, and runup. *Coastal Engineering*, 53, 573-588.
- Sunamura, T. 1992. *Geomorphology of rocky coasts*. Wiley, New York.
- Symonds, G., Huntley, D., Bowen, A.J. 1982. Two-dimensional surf beat: long wave generation by a time-varying breakpoint. *Journal of Geophysical Research*, 87, 492-498.
- Tatavarti, R.V.S.N., Huntley, D.A., Bowen, A.J. 1988. Incoming and outgoing wave interactions on beaches. *Proceedings of the 21st Conference on Coastal Engineering*. ASCE, New York.
- Tissier, M., Bonneton, P., Michallet, H., Ruessink, G. 2015. Infragravity-wave modulation of short-wave celerity in the surf zone. *Journal of Geophysical Research*, 120, 6799-6814.

- Thomson, J., Elgar, S., Raubenheimer, B., Herbers, T.H.C., Guza, R.T. 2006. Tidal modulation of infragravity waves via nonlinear energy losses in the surfzone. *Geophysical Research Letters*, 33, L05601.
- Thornton, E.B., Guza, R.T. 1982. Energy saturation and phase speeds measured on a natural beach. *Journal of Geophysical Research*, 87, 9499-9508.
- Trenhaile, A.S. 1987. *The geomorphology of rock coasts*. Oxford University Press, Oxford.
- Tucker, M.J. 1950. Surf beats: sea waves of 1 to 5 minutes period. *Proceedings of the Royal Society London A*, 202, 565-573.
- Van Dongeren, A., Bakkenes, H.J., Janssen, T. 2002. Generation of long waves by short wave groups. *Proceedings of the 28th Conference on Coastal Engineering*. World Scientific, New Jersey.
- Van Dongeren, A., Battjes, J., Janssen, T., van Noorloos, J., Steenhauer, K., Steenbergen, G., Reniers, A. 2007. Shoaling and shoreline dissipation of low-frequency waves. *Journal of Geophysical Research*, 112, C02011.
- Van Dongeren, A., Lowe, R., Pomeroy, A., Trang, D.M., Roelvink, D., Symonds, G., Ranasinghe, R. 2013. Numerical modelling of low-frequency wave dynamics over a fringing coral reef. *Coastal Engineering*, 73, 178-190.
- Van Thiel de Vries, J.S.M., van Gent, M.R.A., Walstra, D.J.R., Reniers, A.J.H.M. 2008. Analysis of dune erosion processes in large-scale flume experiments. *Coastal Engineering*, 55, 1028-1040.
- Wong, P.P., Losada, I.J., Gattuso, J.P., Hinkel, J., Khattabi, A., McInnes, K.L., Saito, Y., Sallenger, A. 2014. Coastal systems and low-lying areas. Climate change 2014: impacts, adaption, and vulnerability. *Part A: global and sectoral aspects. Contribution of working group II to the fifth assessment report of the Intergovernmental Panel on Climate Change*. Cambridge University Press, Cambridge. pp. 361-409.
- Young, I.R., Zieger, S., Babanin, A.V. 2011. Global trends in wind speed and wave height. *Science*, 332, 451-455.

Appendix A

Noise correction for the array method of Van Dongeren et al. (2007)

In Chapter 4, a mathematical function was developed to correct for the impact of noise when separating wave spectra into incident and reflected components using the method of Gaillard et al. (1980). To demonstrate that the technique used to derive the noise correction function can be applied to other array-based wave decomposition methods, here a noise correction function is developed for the array method of Van Dongeren et al. (2007). Besides the different decomposition method, the procedure used is identical to that outlined in Section 4.1, in which numerical simulations are performed with various wave amplitudes, known reflection coefficients, and signal-to-noise ratios (SNR), with the intention of using the mean coherence between the sensor pairs as a proxy for the level of noise present in the time series. The use of symbols is consistent with Chapter 4.

A.1 Noise correction

Figure A1 demonstrates the positive bias impacting \widehat{S}^+ , \widehat{S}^- , and \widehat{R} , and the corresponding decrease in coherence, as a result of noise being added to the time series. With no noise added, both \widehat{S}^+ and \widehat{S}^- are estimated accurately and are within 4% of their respective target values, and \widehat{R} has a mean value of 0.29. This high level of accuracy is reflected in the mean coherence value of 0.98. SNRs of 2.5, 1.7, and 0.7 introduce an increasing positive bias to \widehat{S}^+ and \widehat{S}^- equal to approximately 7%, 23%, and 128% of S^+ , respectively. Mean coherence values associated with these levels of bias are 0.65, 0.48, and 0.19, respectively. Note that the coherence associated with a SNR of 0.7 is well below the 95% confidence threshold.

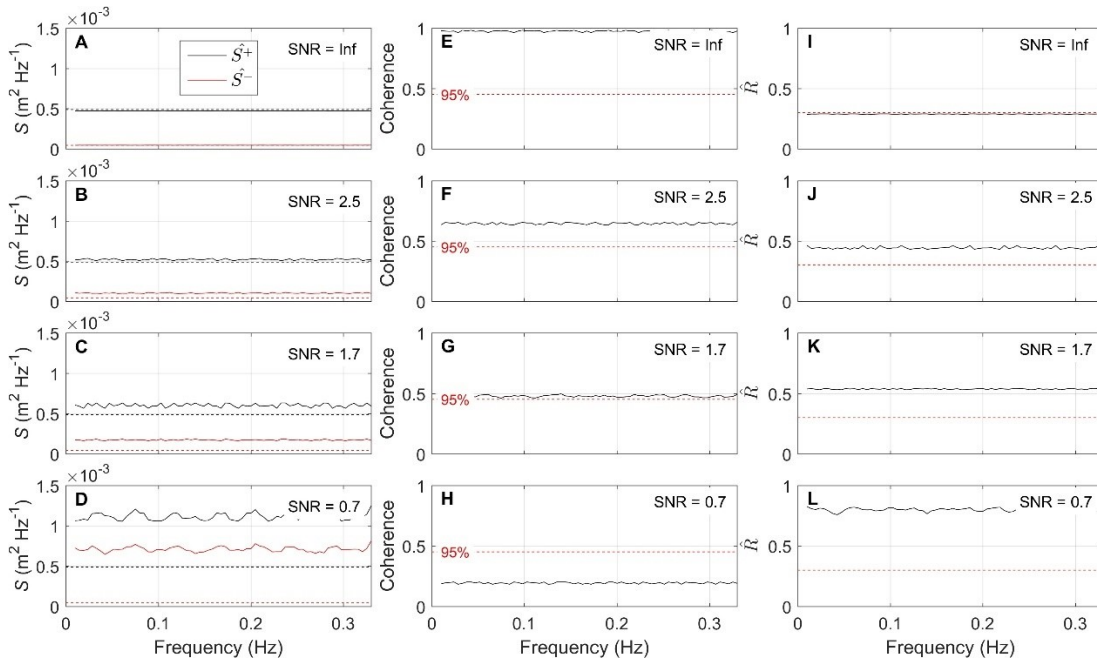


Figure A1. Estimated incident \widehat{S}^+ and reflected \widehat{S}^- spectra (A-D), coherence (E-H), and estimated reflection coefficients \widehat{R} (I-L) for SNR = Inf, 2.5, 1.7, and 0.7 as stated on the figure. Dashed lines in (A-D) are the target incident S^+ and reflected S^- spectra. Red dashed line in (E-H) is the 95% confidence threshold on coherence of 0.45 for 12 degrees of freedom (Shumway and Stoffer, 2000). Red dashed line in (I-L) is the target reflection coefficient R of 0.3. Wave amplitude is 2 m.

The impact of noise on wave reflection estimates using the Van Dongeren et al. (2007) method closely reflects that of the Gaillard et al. (1980) method presented in Section 4.2.1. Most importantly, \widehat{S}^+ and \widehat{S}^- are effected by the same magnitude of bias and this increases linearly with wave amplitude, thus allowing the bias to be normalised by \widehat{S}^+ before being parameterized by the coherence. Normalised bias from all simulations, averaged over the spectrum to give 984 degrees of freedom, is shown against coherence in Figure A2.

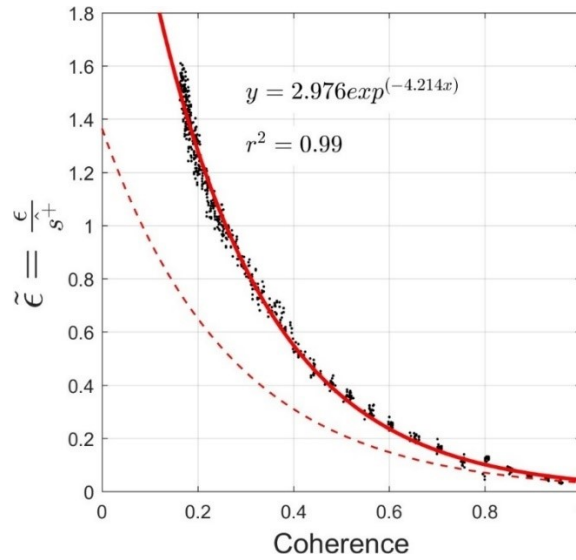


Figure A2. Normalised bias $\tilde{\epsilon}$ (ϵ/\widehat{S}^+ , where ϵ is bias) versus coherence for all wave amplitudes, true reflection coefficients, and SNRs. Data have been smoothed providing one estimate per simulation and 984 degrees of freedom. Solid red line is an exponential regression function with coefficients and accuracy given on the figure. Dashed red line is the exponential regression function used in the correction technique for the Gaillard et al. (1980) method, defined in Figure 4.3.

Consistent with Chapter 4, normalised bias decreases exponentially with increasing coherence and can be predicted very accurately ($r^2 = 0.99$) with an exponential regression function as

$$\hat{\epsilon} = \widehat{S}^+ 2.976 \exp(-4.214C) \quad (\text{A1})$$

Corrected incident and reflected spectra and reflection coefficients are then calculated following Equations 4.5-4.7. The exponential regression function fit to the normalised bias is steeper for the Van Dongeren et al. (2007) method than it is for the Gaillard et al. (1980) method due to the lower mean bias impacting the latter.

A.2 Confidence intervals

Figure A3A shows 95% confidence intervals on $\tilde{\epsilon}$ for coherence bins of 0.1, derived from a t-distribution of the data in Figure A2 with different levels of frequency smoothing and degrees of freedom between 12 and 984. Analogous to the results presented in Chapter 4,

confidence intervals are shown to increase with decreasing coherence and the rate of this increase is steeper for lower degrees of freedom. However, confidence intervals associated with the Van Dongeren et al. (2007) are larger for a given coherence level and degrees of freedom than they are for the Gaillard et al. (1980) method. For example, for 120 degrees of freedom (approximately equivalent to averaging over the infragravity band) and a coherence value of 0.75, confidence intervals on $\tilde{\epsilon}$ are ± 0.06 and ± 0.02 for the Van Dongeren et al. (2007) and Gaillard et al. (1980) methods, respectively.

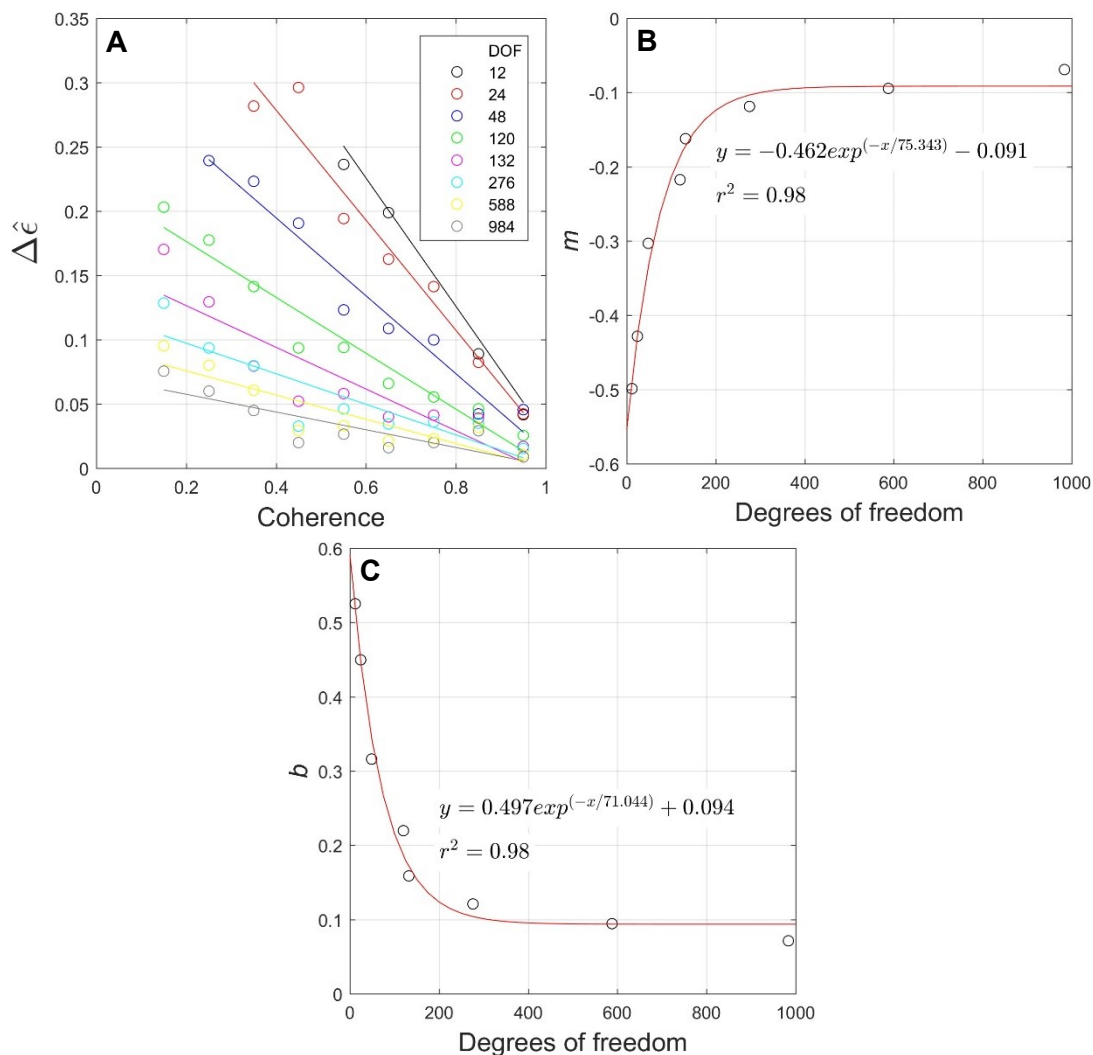


Figure A3. 95% confidence intervals on normalised bias $\Delta \tilde{\epsilon}$ for various degrees of freedom versus coherence (A). Solid lines are linear regression lines fit to the data of the corresponding colour. Slopes m (B) and intercepts b (C) from the linear regression lines shown in (A) versus degrees of freedom. Solid red lines in (B) and (C) are exponential regression functions with coefficients and accuracy given on the figure.

Linear regression models between the confidence intervals and coherence yield r^2 values between 0.72 and 0.96 for the different degrees of freedom. The slopes and intercepts from the linear regressions are predicted accurately ($r^2 = 0.98$ and 0.98 , respectively) using exponential regression functions and the degrees of freedom (Figures A3B and A3C), allowing 95% confidence intervals on corrected spectra to be calculated as

$$\begin{aligned} \Delta \widehat{S}_c^\pm = \widehat{S}^\pm & \left((-0.462 \exp^{-v/75.343}) - 0.091 \right) C \\ & + \left(0.497 \exp^{-v/71.044} + 0.094 \right) \end{aligned} \quad (\text{A2})$$

and 95% confidence intervals on estimated reflection coefficients are calculated following Equation 4.9.

A.3 Application to simulated data

Figure A4 demonstrates the correction technique outlined in the previous section using simulated data with a wave amplitude of 4 m and a true reflection coefficient of 0.3. With a SNR of 10.0, \widehat{S}^\pm is overestimated by an average of 6.40%, whereas the mean absolute error on \widehat{S}_c^\pm is 0.92%. \widehat{R}_c is 0.30 which is an improvement on the \widehat{R} estimate of 0.37. Corrected values are similarly accurate for a SNR of 3.3 with a mean error on \widehat{S}_c^\pm of 1.53%, compared to 12.71% on \widehat{S}^\pm , and a mean \widehat{R}_c 0.31. A SNR of 2.0 causes \widehat{S}^\pm to be overestimated by 28.64%, whilst \widehat{S}_c^\pm has a mean error of only 4.36%; a decrease in error magnitude of >80%.

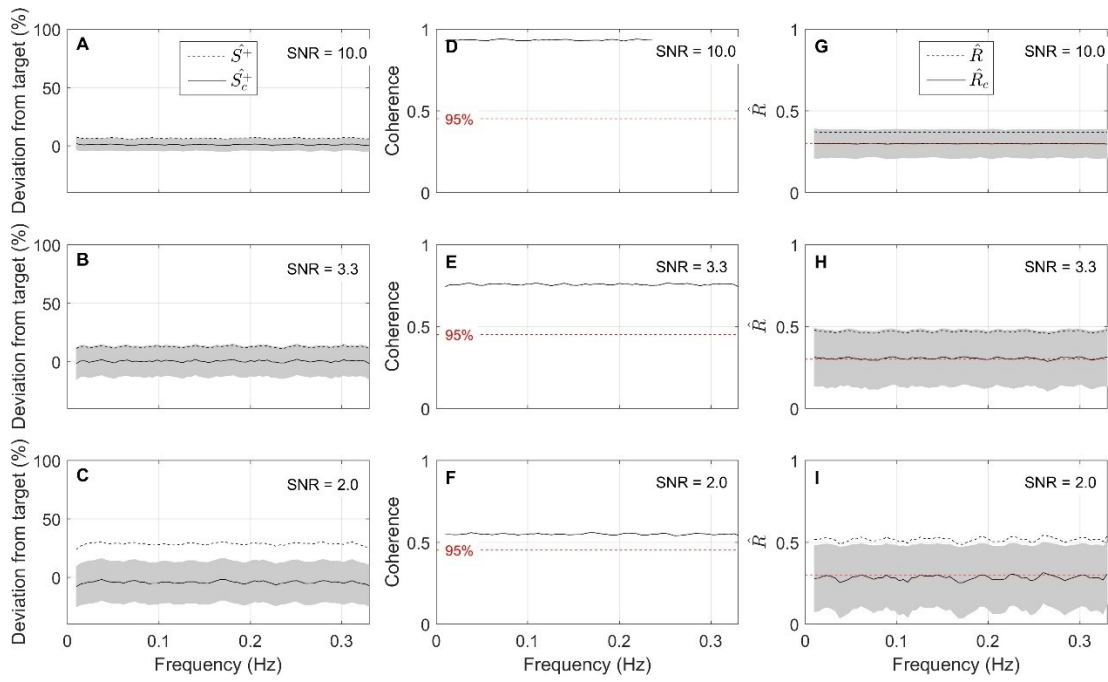


Figure A4. Deviation (%) of uncorrected \widehat{S}^+ and corrected \widehat{S}_c^+ incident spectra from the target value S^+ (A-C). Coherence (D-F), and uncorrected \widehat{R} and corrected \widehat{R}_c reflection coefficients (G-I). Shaded areas in (A-C) are 95% confidence intervals on \widehat{S}_c^+ and shaded areas in (G-I) are 95% confidence intervals on \widehat{R}_c . SNRs are 10.0, 3.3, and 2.0 as stated on the figure. Red dashed line in (D-F) is the 95% confidence threshold on coherence of 0.45 for 12 degrees of freedom (Shumway and Stoffer, 2000). Red dashed line in (G-I) is the target reflection coefficient R of 0.3. Wave amplitude is 4 m.

Appendix B

Published paper 1

Inch, K., Davidson, M., Masselink, G., Russell, P. 2015. Propagation and dissipation of infragravity waves on a dissipative beach with energetic wave forcing. *Proceedings of Coastal Sediments 2015*, World Scientific, San Diego, USA.

Appendix C

Published paper 2

Inch, K., Davidson, M., Masselink, G., Russell, P. 2016. Accurate estimation of wave reflection on a high energy, dissipative beach. *Journal of Coastal Research*, SI 75, 877-881.

Appendix D

Published paper 3

Inch, K., Davidson, M., Masselink, G., Russell, P. 2017. Correcting wave reflection estimates in the coastal zone. *Coastal Engineering*, 119, 65-71.

Appendix E

Published paper 4

Inch, K., Davidson, M., Masselink, G., Russell, P. 2017. Observations of nearshore infragravity wave dynamics under high energy swell and wind-wave conditions. *Continental Shelf Research*, 138, 19-31.